IntechOpen

Acoustical Engineering

The Intricate World of Sound Technology

Edited by Jiangyi Zhang

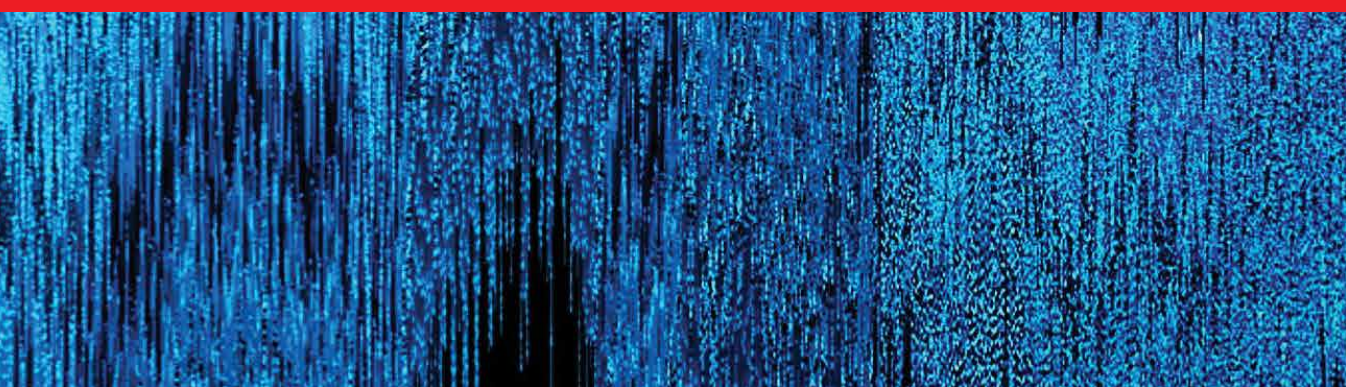

Acoustical Engineering - The Intricate World of Sound Technology

Edited by Jiangyi Zhang

Published in London, United Kingdom

Acoustical Engineering - The Intricate World of Sound Technology
http://dx.doi.org/10.5772/intechopen.1004684
Edited by Jiangyi Zhang

Contributors
Ben Wang, Bingkun Zhang, Cagri Yilmaz, Haoda Yu, Hua Xia, Irina Lutsenko, Keyong Hu, Maryna Kyrychenko, Oleksandr Soboliak, Rostand B. Tayong, Ruslan Ahaiev, Serhii Yehorov, Shuifa Sun, Trifanov Vitalii, Vadym Yehorov, Vasyl Vlasenko, Vasyl Zberovskyi, Vladyslav Lutsenko, Wenbo Liu, Yang Feng, Yiyang Luo, Zhen Yang

First published in London, United Kingdom, 2025 by IntechOpen
IntechOpen is the global imprint of INTECHOPEN LIMITED, registered in England and Wales, registration number: 11086078, 167-169 Great Portland Street, London, W1W 5PF, United Kingdom

For EU product safety concerns: IN TECH d.o.o., Prolaz Marije Krucifikse Kozulić 3, 51000 Rijeka, Croatia, info@intechopen.com or visit our website at intechopen.com.

British Library Cataloguing-in-Publication Data
A catalogue record for this book is available from the British Library

Acoustical Engineering - The Intricate World of Sound Technology
Edited by Jiangyi Zhang
p. cm.
Print ISBN 978-0-85014-856-5
Online ISBN 978-0-85014-855-8
eBook (PDF) ISBN 978-0-85014-857-2

If disposing of this product, please recycle the paper responsibly.

Meet the editor

From 2011 to 2019, Jiangyi Zhang studied for her undergraduate, master's and doctoral degrees at the Acoustics Laboratory of the University of Le Mans in France. Then, from 2019 to 2021, she worked as a postdoctoral researcher at the Department of Civil Engineering of Delft University of Technology in the Netherlands. In 2021, she served as an associate professor at the College of Underwater Acoustic Engineering of Harbin Engineering University. Dr. Zhang's main areas of study are nonlinear dynamics, nonlinear acoustics and nonlinear metamaterials, focusing on the interaction between nonlinearity, dissipation, and dispersion.

Contents

Preface

With the rapid development of technology, acoustic technology, as an ancient and dynamic discipline, is constantly demonstrating its unique charm and enormous application potential in various fields. At present, acoustic technology is changing our way of life and work at an unprecedented speed. The book *Acoustical Engineering – The Intricate World of Sound Technology* aims to comprehensively introduce the latest research progress of acoustic technology in various fields, providing readers with a window to gain a deeper understanding of the cutting-edge dynamics of acoustic technology.

This book includes the observable response of microcantilever beams to dynamic acoustic forces under single frequency excitation, acoustic monitoring of coal and rock mass states in water impact stress-strain zones, development of a low altitude outdoor moving target recognition system based on acoustic features, noise reduction performance of microporous plates, and application of surface acoustic wave yarn tension sensors.

Below is a specific introduction to the content of this book.

1. A Numerical Analysis of Single-Frequency Responses of the Resonant Micro-Cantilever to Dynamic Acoustic Forces Based on the Forced Van der Pol-Rayleigh-Mathieu Oscillator

In this work, a nonlinear dynamic model based on the forced Van der Pol Rayleigh-Mathieu is used to acquire the observable responses of the micro-cantilever to dynamic acoustic forces in the single-frequency excitations. Behaviors of the resonant micro-cantilever under external forces are strongly dependent on the simulation parameters. The start time, the time interval, and the initial boundary conditions considerably affect the flexural deflections on the particular time domains. Additionally, amplitude and phase shift can be simply extracted from the oscillatory motions to explore the micro-cantilever sensitivity to acoustic forces for different start times and time intervals. Furthermore, dynamic responses, including displacements and velocities, are demonstrated for the first two flexural eigenmodes considering different initial displacements. Therefore, the single-frequency responses of the resonant micro-cantilever can be investigated to quantify the sensitivity to periodic acoustic forces considering the effects of numerical simulation parameters.

This study involves microelectromechanical systems' micro cantilever beam structure, which generates dynamic response under specific frequency acoustic excitation. Quantitative observation and analysis of sound force can be achieved by accurately measuring this response. This is significant for fields such as acoustic sensors and sound signal processing.

2. Acoustic Monitoring of the Coal-Rock Massif State in Stress-Strain Zones during Hydroimpulsive Impact: Application Experience

The chapter presents the results of acoustic monitoring studies on the state of coal-rock massif during the hydro-impulsive loosening of outburst-hazardous coal seams in the working faces of development workings. The main methodological regulations for using acoustic monitoring systems in the mines of Ukraine and the parameters for evaluating the effectiveness of control methods on the stress-strain state of the outburst-hazardous massif are presented. The results of using acoustic systems in the study of the coal-rock massif state and the criteria substantiation for controlling and evaluating the effectiveness of hydro-loosening of outburst-hazardous coal seams are considered. A comparison of the results of theoretical, laboratory, and mining-experimental studies under the conditions of the mines of "Krasnodonvuhillia" was performed.

3. Development of an Advanced System for Identifying Low-Altitude Outdoor Mobile Objects Based on Acoustic Signatures

This chapter introduces an acoustic-based detection system for low-altitude moving objects, including unmanned aerial vehicles, helicopters, and ground vehicles. Key challenges addressed include target differentiation, bearing estimation accuracy, environmental noise impact, and the need for meteorological adjustments. Experimental results show that high-pass filters with a 500–700 Hz rejection band improve target detection contrast and reduce noise interference.

This study aims to use acoustic features to identify outdoor moving targets flying at low altitudes. By extracting and analyzing the acoustic signal features generated by the target, automatic recognition and tracking of the target can be achieved. This is significant for fields such as air traffic management and safety monitoring.

4. On the Use of Micro-Perforated Panels for Sound Absorption

This study deals with the sound absorption of micro-perforated panels (MPP) as an effective solution for sound reduction. Single and multiple MPPs backed by an air cavity are presented and analyzed, and both their behavior and response are modeled and measured. It is shown that sound absorption in the low-frequency ranges can be enhanced by using the combined effects of multiple MPPs and their vibrational effects. Relatively good agreement is also observed between the prediction and the measurement. The study suggests the present technique as a relatively easy and cheap technique for enhancing systems' sound absorption, including MPPs backed by air cavities.

5. The Application of Surface Acoustic Wave Yarn Tension Sensor

Surface acoustic wave sensor is a sensor based on the principle of sound wave propagation on solid surfaces. In yarn tension monitoring, surface acoustic wave sensors can monitor the tension changes of yarn in real time and indirectly measure the tension of yarn by analyzing the changes in acoustic signals. This is of great significance for quality control in industries such as textiles, printing, and dyeing.

In this chapter, a new type of surface acoustic wave yarn tension sensor is designed. The test parameters are improved, including the design and simulations of the SAW sensor, the solution to the second-order effect problem of the SAW yarn tension sensor, the design and application of the dual differential channel oscillator on the SAW yarn tension sensor, the temperature compensation of SAW yarn tension sensor based on PSO-LSSVM algorithm, which enhances the sensor's performance.

In summary, the research content covered by the book *Acoustical Engineering – The Intricate World of Sound Technology* involves cutting-edge explorations of acoustic theory and practical applications of acoustic technology in multiple fields. These research results not only promote the development of the field of acoustics but also provide strong support for the technological progress of related industries.

Jiangyi Zhang
Harbin Engineering University,
Harbin, China

Chapter 1

A Numerical Analysis of Single-Frequency Responses of the Resonant Micro-Cantilever to Dynamic Acoustic Forces Based on the Forced Van der Pol-Rayleigh-Mathieu Oscillator

Cagri Yilmaz

Abstract

In the present work, a nonlinear dynamic model based on the forced Van der Pol-Rayleigh-Mathieu is used to acquire the observable responses of the micro-cantilever to dynamic acoustic forces in the single-frequency excitations. Behaviors of the resonant micro-cantilever under external forces are strongly dependent on the simulation parameters. The start time, the time interval, and the initial boundary conditions considerably affect the flexural deflections on the particular time domains. Additionally, amplitude and phase shift can be simply extracted from the oscillatory motions to explore the micro-cantilever sensitivity to acoustic forces for different start times and time intervals. For instance, the amplitude at the second eigenmode fluctuates in the 0–500 pm region on the start time domain of 0–20 ms for the time interval range of 0.0001–0.1 ms. It is remarkably vital to observe the changes in the observables in response to different values of numerical simulation parameters for better sensitivity analysis. Furthermore, dynamic responses including displacements and velocities are demonstrated for the first two flexural eigenmodes considering different initial displacements. Therefore, the single-frequency responses of the resonant micro-cantilever can be investigated to quantify the sensitivity to periodic acoustic forces considering the effects of numerical simulation parameters.

Keywords: acoustic force sensitivity, micro-cantilever, single-frequency excitation, numerical simulation parameters, amplitude, phase shift

1. Introduction

Sensitivities of micro-structures such as micro-cantilevers to external forces are explored using experimental and theoretical techniques for a variety of purposes in

engineering applications. In Atomic Force Microscopy (AFM) operations [1, 2], tip-sample interaction force is considered as an external force, which determines the vibration characteristics of the micro-cantilever. Amplitude, frequency, and phase shift responses are used to extract the surface topography and the material properties of the samples in AFM. Effective acoustic forces that can be modeled as static [3] and dynamic forces [4] also change the oscillatory behaviors of resonantly driven micro-cantilevers at different eigenmode frequencies. The interactions of cantilevers with Acoustic Emissions (AEs) are widely studied for different technical applications. For instance, when the frequency of the surface acoustic wave exceeds the eigenmode frequency of the micro-cantilever, the deflections can be much larger than the amplitude of the surface modulation. In Ref. [5], a method based on an experimental force-curve is developed to calibrate the actual amplitude of the surface acoustic wave. Acoustic emission tests are also conducted to measure the crack probability for the semiconductors. Oxide cracks on the chip surface generate acoustic emissions during contact with the indenter tip [6]. Performing electrical tests, strain gauges for force measurements and a piezoelectric sensor can be integrated into a cantilever with an indenter. Moreover, a capacitive Micro-Electro-Mechanical System (MEMS) resonator is developed in Ref. [7] to sense acoustic emissions for cantilever-enhanced photoacoustic spectroscopy. A sensitivity of 3749 mV Pa^{-1} at the resonant frequency 1870 Hz is achieved for the bias voltage of 15 V. In addition to that, a method is proposed to excite the micro-cantilever using localized acoustic forces in fluidic AFM operations [8]. Additionally, the AFM micro-cantilevers can be characterized utilizing the developed method in a viscous environment. For instance, acoustic radiation force can be used to measure the spring constant of the micro-cantilever. The guidewire can also be utilized when a catheter is introduced to the capillary blood vessel with the diameter of less than 2 mm. For this issue, the direct catheter manipulation method, in which the acoustic radiation force is used, is developed in the study [9]. This technique allows the catheter with a diameter of less than 0.5 mm to reach the target area. Studying micro-cantilever dynamics in SubSurface-AFM, a numerical simulation is conducted in Ref. [10] to determine responses of a cantilever which oscillates at an ultrasonic frequency. At the same time, the sample is also excited at slightly different ultrasonic frequencies to calculate the amplitude and phase of the difference frequency. Oscillation observables can be robustly used to image the nanoparticles below the sample surface.

Based on numerical calculations performed in Ref. [4], it is mentioned that numerical simulation parameters such as start time of the simulation, time interval, and the initial boundary conditions significantly affect the micro-cantilever responses to acoustic forces. The effects of simulation parameters such as boundary conditions and time intervals on the responses of mechanical systems are investigated for different engineering purposes. Dynamic performances of the structures strongly depend on the boundary conditions and time intervals utilized in numerical calculations. The influence of varied boundary conditions on the dynamic behaviors of the functionally graded nanotubes is explored in the study [11]. The numerical results indicate that the boundary conditions remarkably affect the natural frequencies of the nanotubes. In another work [12], numerical calculations are conducted to investigate the influence of surface roughness on cantilever displacements considering variable boundary conditions. Periodic boundary conditions that are perpendicular to the micro-cantilever length are utilized for this case. In Ref. [13],

the influence of boundary conditions on oscillations of a long inflatable tube is studied with the consideration of the elastic modulus and air-added mass. It is demonstrated that the natural frequencies of the cantilever tubes are notably affected by the boundary conditions. An exact approach is also introduced in Ref. [14] to explore the dynamic responses of the cracked beams with diverse boundary conditions. The lowest two circular natural frequencies are determined for pinned-pinned boundary conditions. In the work in Ref. [15], a pseudo-dynamic analysis method is applied to examine the structural performance of the cantilever column system by performing experimental and analytical studies. It is mentioned that the value of the selected time interval is to be too small for ensuring stability in the numerical computations.

In the present work, a Van der Pol-Rayleigh-Mathieu oscillator is used to investigate the influences of numerical simulation parameters on the dynamic responses of the micro-cantilever. Different nonlinear oscillators, such as Van der Pol, Rayleigh, Mathieu, and Duffing oscillators [16], are used to examine viscoelastic and structural damping on vibrations of the structures. A damping Helmholtz-Rayleigh-Duffing oscillator solved using the nonperturbative method is introduced in Ref. [17]. The frequency formula is modified to provide contributions of the damping and quadratic nonlinear forces in the proposed approach. New approximations and exact solutions to the damped Duffing-Mathieu oscillator are acquired to explore nonlinear oscillations [18]. Analytical results obtained using the extended Krylov-Bogoliubov-Mitropolskii method are compared with the numerical ones calculated using the Runge-Kutta method. In addition to that, a Lienard equation including a generalized Van der Pol-Helmholtz equation is introduced in the study [19]. The first integral method is utilized to demonstrate the exact and explicit solutions.

This work introduces a novel conceptual model to examine the effects of the start time, time interval, and initial boundary conditions on the behaviors of the resonant micro-cantilever under dynamic acoustic forces. The micro-cantilever is driven using a monomodal excitation scheme to enhance its sensitivity. Flexural displacements at the first two eigenmodes are obtained in the presence of acoustic forces which are at resonance frequencies of the micro-cantilever. Time-domain displacements and observable responses are demonstrated for different start times and time intervals. Amplitude and phase shift at the first two eigenmodes are exhibited to track the changes in observable responses to varied time intervals on the domain of the start time of the numerical simulation. Additionally, dynamic responses that include flexural displacements and velocities are revealed for different initial displacements at the first two vibrational modes. Therefore, observing changes in micro-cantilever responses to varied simulation parameters enables to improve the quantification of sensitivity to dynamic acoustic forces.

2. Conceptual model

The present work introduces a mathematical framework based on a Van der Pol-Rayleigh-Mathieu oscillator to explore the effects of simulation parameters on responses under excitation and acoustic forces. The micro-cantilever is driven externally at the first or second eigenmode frequency in monomodal operations. In AFM operations, sensitivity to external forces can be enhanced by driving the

micro-cantilever at a higher mode. The second-order nonlinear differential equation based on the Van der Pol-Rayleigh-Mathieu oscillator is formulated as below:

$$\ddot{z}_i(t) + \frac{k_i}{m_e} z_i(t) + h(\dot{z}_i, z_i) + g(z_i) = \frac{1}{m_e}(F_{Exc} + F_{Acoustic}) \tag{1}$$

where $z_i, \dot{z}_i$, and $\ddot{z}_i$ are the time-varying deflection, velocity, and the acceleration of the micro-cantilever, respectively. k_i and m_e are the spring constant and the effective mass of the micro-cantilever respectively. In the present work, the properties of the micro-cantilever for the first (i = 1) and second (i = 2) eigenmode are given in **Table 1** (**Figure 1**).

The micro-cantilever has a length (L) of 225 μm, a width (w) of 40 μm, a thickness (t) of 1.8 μm, and an effective mass of 1.53×10^{-11} kg. The Van der Pol-Rayleigh function is introduced by:

$$h(\dot{z}_i, z_i) = \frac{\omega_{ei}}{Q_i}\dot{z}_i(t) + \frac{1}{m_e}\left(\eta_1 {z_i}^2(t)\dot{z}_i(t) + \eta_2 {\dot{z}_i}^3(t)\right) \tag{2}$$

where ω_{ei} and Q_i are the angular resonance frequency and the quality factor at the eigenmode i, respectively. f_{ei} is the resonance frequency at the eigenmode i. η_1 and η_2 are the nonlinearity coefficients of the Van der Pol-Rayleigh functions.

The equation of angular resonance frequency at the eigenmode is introduced as follows:

$$\omega_{ei} = \sqrt{\frac{k_i}{m_e}} = 2\pi f_{ei}. \tag{3}$$

Eigenmode—i	Frequency—f_{ei} (kHz)	Stiffness—k_i $\left(\frac{N}{m}\right)$	Quality factor—Q_i
1	48.9	0.9	255
2	306.7	35.4	1598.9

Table 1.
Micro-cantilever properties for the first two eigenmodes.

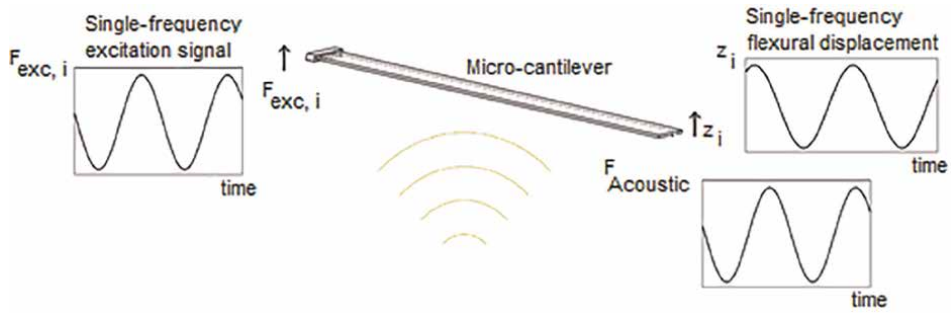

Figure 1.
A schematic representation for single-frequency flexural deflections of the resonant micro-cantilever under dynamic acoustic forces for the first two eigenmodes under monomodal operations.

The characteristic equation of the rectangular micro-cantilever is given below [20]:

$$1 + \cos(\kappa_i)\cosh(\kappa_i) = 0. \tag{4}$$

Based on the real root κ_i of the characteristic equation, the angular resonance frequency is determined utilizing the following equation as follows:

$$\omega_{ei} = (\kappa_i L)^2 \sqrt{\frac{El_z}{\rho A}} \tag{5}$$

where E, l_z, ρ, and A are the Young's modulus, the area moment of inertia, the mass density, and the cross-sectional area of the micro-cantilever, respectively.

The Mathieu function is formulated as follows:

$$g(z_i) = \delta {\omega_{ei}}^2 \cos(\omega_p t)\, z_i \tag{6}$$

where δ and ω_p are the excitation amplitude and frequency, respectively.

In numerical computations, the Van der Pol-Rayleigh coefficients η_1 and η_2 are set to 10^{-9} and the Mathieu coefficients δ and ω_p are taken as 1 and 30, respectively.

The micro-cantilever which is driven externally is also subject to the dynamic acoustic forces. The equation of excitation force F_{exc} for the eigenmode i is given as follows:

$$F_{Exc} = F_i \cos(\omega_{ei} t) \tag{7}$$

where F_i is the driving force strength for the vibration mode i. In AFM operations, the driving force strengths are determined using the free amplitudes at the eigenmodes. The equation of the driving force strength is given as follows [21]:

$$F_i = \frac{k_i A_{0i}}{Q_i} \tag{8}$$

where A_{0i} is the free amplitude for the eigenmode i. In the present work, A_{01} is taken as 8 nm and $\frac{A_{02}}{A_{01}}$ is set to 0.1 for the numerical computations.

Note that the micro-cantilever is driven at resonance frequency to increase its sensitivity to acoustic forces. The dynamic acoustic force $F_{Acoustic}$ is also formulated as given below [4]:

$$F_{Acoustic} = F_{Ac} \cos(\omega_{Ac} t) \tag{9}$$

where F_{Ac} and ω_{Ac} are the acoustic force strength and frequency, respectively. Static acoustic force ($F_{Acoustic} = F_s$) also induces variations in observable responses of the resonant micro-cantilever in single- and bimodal-frequency excitations [3].

Note that the maximum amplitude sensitivity to acoustic force is observed when the acoustic-force frequency is equal to the resonance frequency of the micro-cantilever. In the present work, the strength of acoustic force is taken as 100 pN (AE amplitude around 54.9 dB), and the acoustic force frequencies are set to the 307.25 kHz (ω_{e1}) and 1927.1 kHz (ω_{e2}) while computing the forced deflections at the

first and second flexural modes, respectively. Amplitude and phase shift can be simply obtained from the deflection at the eigenmode i:

$$z_i(\mathrm{t}) = A_i \cos(\omega_{ei} - \varnothing_i) + O(\varepsilon) \tag{10}$$

where A_i and $\varnothing_i$ are the amplitude and phase shift for the eigenmode i. $O(\varepsilon)$ represents the influence of displacements at higher harmonics. Obtaining deflections, the second-order nonlinear differential equation is solved using the Adams-Bashforth-Moulton method. The numerical computations are performed in a MATLAB environment.

3. Results and discussions

In this section, firstly, time-domain behaviors of the resonant micro-cantilever at the flexural eigenmodes are demonstrated for different start times and time intervals. Observables of vibration oscillations exhibit different responses for different values of numerical simulation parameters. Correspondingly, amplitude and phase shifts in the domain of start time are revealed and evaluated considering the effects of the time interval on the quantification of micro-cantilever sensitivity to acoustic forces. Lastly, dynamic responses of the micro-cantilever at the first two flexural modes are assessed for diverse initial displacements.

3.1 Time-domain flexural displacements

The start time of the numerical simulation considerably determines the free and forced behaviors of the micro-cantilever (**Figure 2**). For the time range between 27.20 and 27.25 ms, the amplitude of vibration at the first flexural mode does not remarkably change as the start time varies. On the other hand, the phase shift notably changes with increasing start time. Phase shift is utilized to extract the material properties and to explore the gradient of tip-sample interaction forces, especially at higher modes in multi-frequency AFM operations [22]. Based on the results depicted in **Figure 2**, the largest phase shift of 180 degrees at the fundamental mode is achieved at the start time of 12 ms (**Figure 2(c)**). Besides, the sensitivity of external forces such as acoustic forces are studied using phase shift responses at the fundamental and higher modes [3]. Thus, the influence of start time is to be considered while obtaining the simulation results.

The second mode also demonstrates similar observable responses to the first mode. Phase shift sensitivity is prevalent for the second mode and changes in amplitude responses to acoustic forces are also notable for diverse start times (**Figure 3**). Note that the phase shift can be calculated by considering the peak points of free vibrations (only driving forces) and forced vibrations (under driving and acoustic forces) in the particular time period. As expected, the vibration frequencies do not change as the start time varies for both modes. External forces acting on the cantilever-tip, such as hydrodynamic, Casimir, or Van der Waals forces, induce variations in frequency responses, which can be used to quantify micro-cantilever sensitivity. Since the micro-cantilever has maximum amplitude sensitivity to dynamic acoustic forces at the resonance frequencies, the acoustic forces at 307.25 and 1927.1 kHz are considered to interact with the resonantly excited micro-cantilever. Since the sensitivity quantification to external signals is performed based on the selected time period, the start time

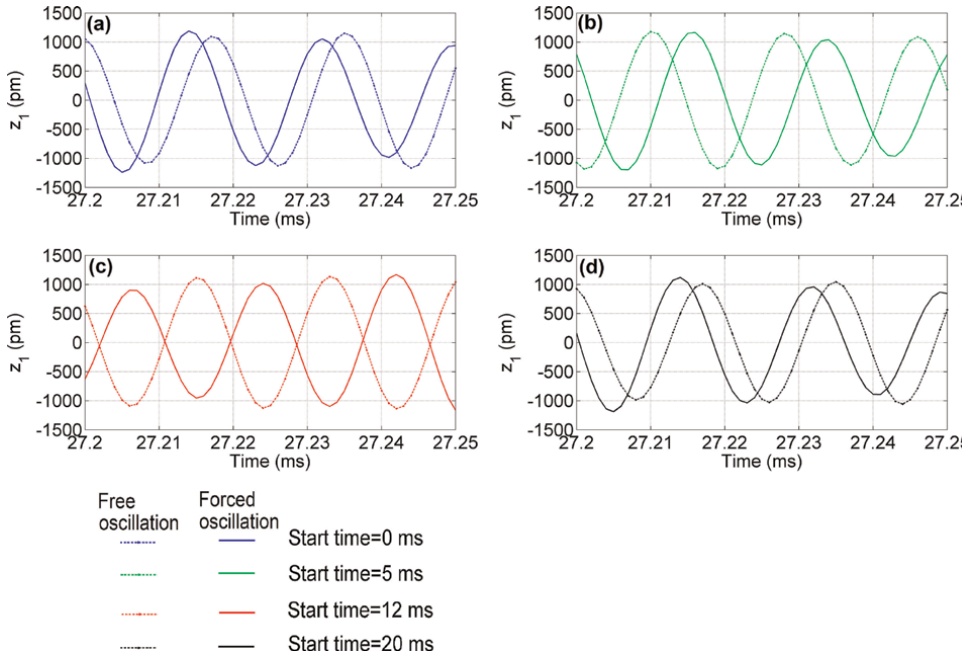

Figure 2.
Flexural displacements of the resonant micro-cantilever at the first eigenmode under acoustic force strength of 100 pN at the angular frequency of 307.25 kHz for the time interval of 0.001 ms, the initial displacement of 0 nm, and different start times of numerical simulations.

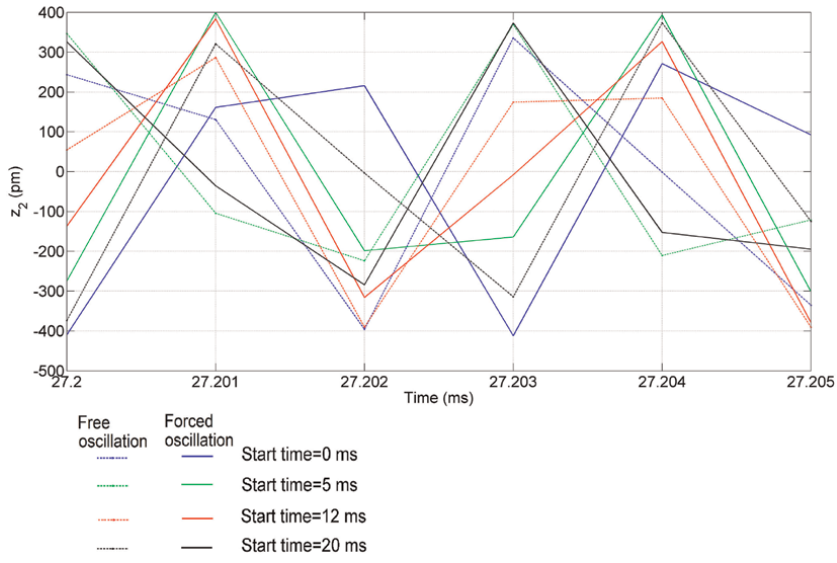

Figure 3.
Flexural displacements of the resonant micro-cantilever at the second eigenmode under acoustic force strength of 100 pN at the angular frequency of 1927.1 kHz for the time interval of 0.001 ms, the initial displacement of 0 nm, and different start times of numerical simulations.

considerably influences the oscillation observables. While constructing a dynamic model for the resonant micro-cantilever under external forces, the value of the start time is to be varied based on the comparison of measurements and numerical results.

The time interval characterizes the oscillatory responses of the micro-cantilever obtained using numerical simulation. Observables can be simply obtained from the periodic displacements of the micro-cantilever. Herein, for the first eigenmode, the oscillation amplitude and phase shift are extracted from the responses obtained in numerical simulations performed using the time interval of 0.001 and 0.0001 ms (**Figure 4(c)** and **(d)**). This result suggests that sensitivity analysis based on vibration observables is reliable provided that a relatively smaller time interval is adjusted for numerical computations. Similar to the start time effect, the phase shift is strongly dependent on the time interval as expected. It is also worth mentioning that vibration amplitude changes as the time interval increases. Variations in amplitude with respect to the time interval are much larger than the ones which vary with the start time.

More significantly, changes in observable responses with respect to the time interval at the higher eigenmode also differ from ones for the fundamental eigenmode. For this case, the second eigenmode requires a much smaller value of the time interval while obtaining oscillatory motions of the micro-cantilever (**Figure 5(d)**).

Note that the time interval also does not affect the frequency sensitivity to dynamic acoustic force as expected. Since quantification of sensitivity is based on the variations in oscillation observables, acquiring oscillatory motion is quite critical in numerical simulations. The numerical results obtained using the nonlinear dynamic model in the current work are consistent with the ones obtained using the single degree of freedom lumped parameter model in Ref. [4]. For this case, the time interval

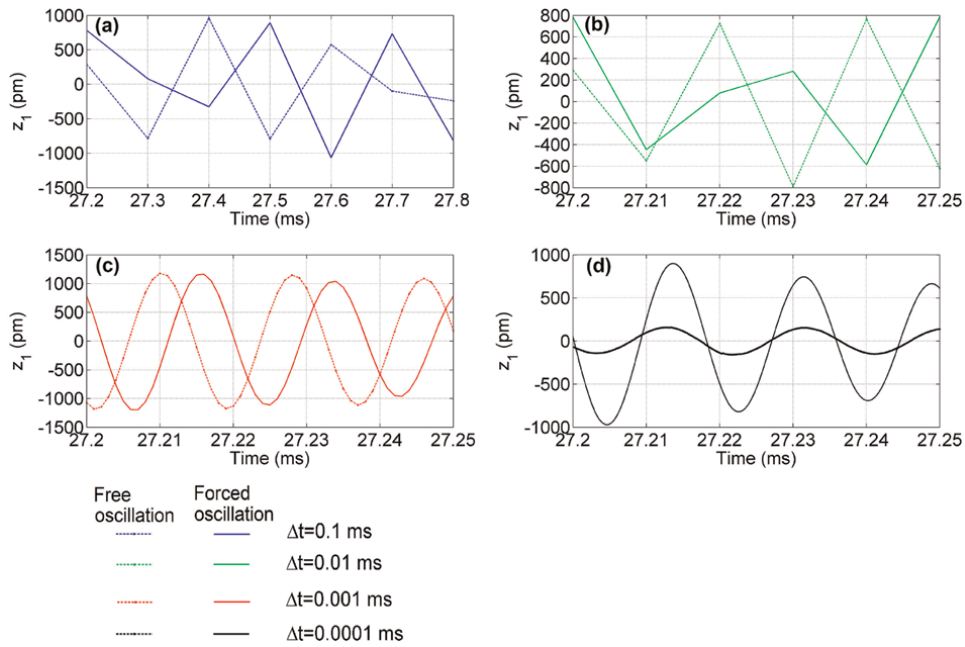

Figure 4.
Flexural displacement of the resonant micro-cantilever at the first eigenmode under acoustic force strength of 100 pN at the angular frequency of 307.25 kHz for the start time of 5 ms, the initial displacement of 0 nm, and different time intervals of numerical simulations.

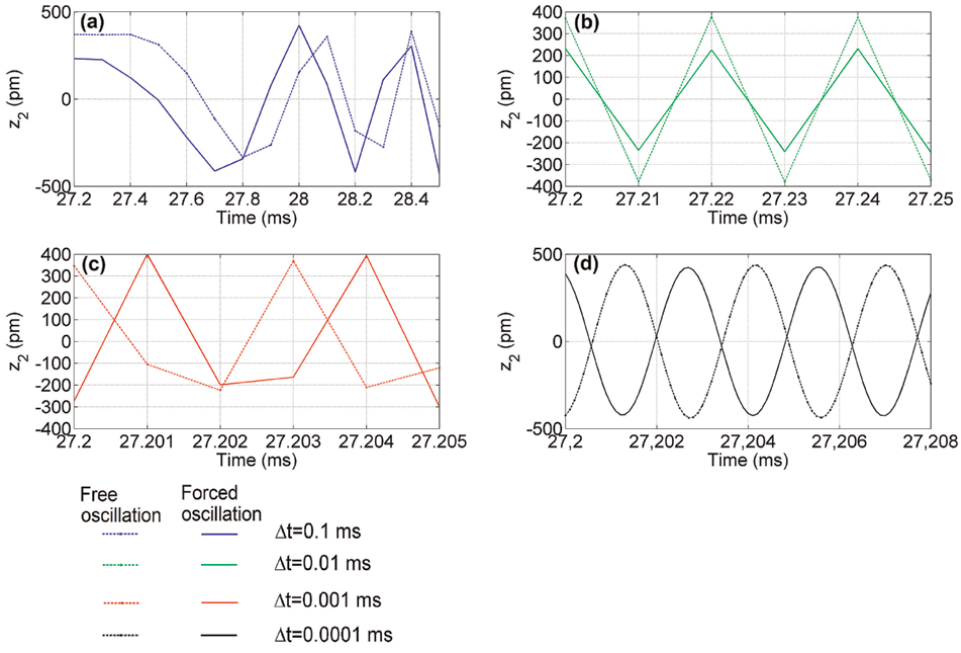

Figure 5.
Flexural deflections of the resonant micro-cantilever at the second eigenmode under acoustic force strength of 100 pN at the angular frequency of 1927.1 kHz for the start time of 5 ms, the initial displacement of 0 nm, and different time intervals of numerical simulations.

of 0.0001 ms is used to acquire single-frequency responses in bimodal-frequency excitations. Thus, the time interval is to be set to the critical value so that oscillatory motions are obtained for all vibrational modes in diverse single-frequency excitations.

3.2 Amplitude and phase shift responses

Influence of numerical simulation parameters on vibration observables is studied for enhanced analysis of sensitivity quantification. Demonstrating variations in observables with respect to the start time for different time intervals enables to optimize the numerical simulation. As mentioned before, obtaining periodic responses is quite crucial to quantify the micro-cantilever sensitivity to dynamic acoustic forces. As depicted in **Figure 6(a)**, amplitude response for the time interval of 0.0001 ms at the fundamental eigenmode exhibits fluctuating behaviors. Other amplitude responses have also similar trends in the amplitude range between around 500 and 1200 nm. In addition, the phase shift significantly responds to varying start times (**Figure 6(b)**). For varied time intervals, remarkable changes in phase shift responses are also prevalent for the first eigenmode. The phase shift responses fluctuate within the range between 0 and 180 degrees. This finding points out the importance of the selection of the proper time interval values for different start times in the investigation of acoustic force sensitivity. Proper time intervals can be simply determined by considering observable responses extracted from steady oscillatory motions (**Figure 4(c)** and **(d)**).

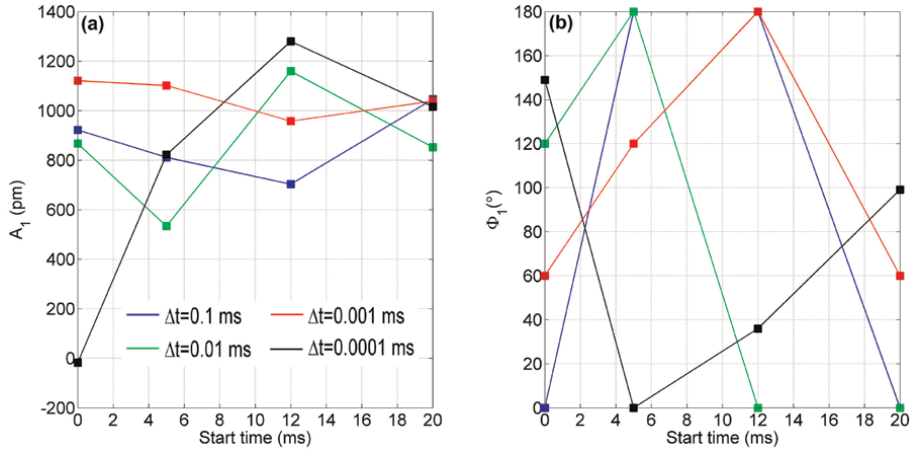

Figure 6.
Observable responses at the first eigenmode to acoustic force strength of 100 pN at the angular frequency of 307.25 kHz on the domain of start time of numerical simulation for the initial displacement of 0 nm and for varied time intervals. (a) Amplitude. (b) Phase shift.

The second eigenmode demonstrates different observable sensitivities in the domain of start time for varied time intervals (**Figure 7**). The amplitude response varies within the range of roughly 0–500 nm and the phase shift fluctuates in the range of approximately 0–180 degrees. It is obvious that the responses at the second eigenmode exhibit similar variations with respect to the start time and the time interval as for the first eigenmode. The higher eigenmode demonstrates different oscillatory motions using same values of the numerical simulation parameters. Correspondingly, the higher eigenmode might require different values of time intervals to reach the periodic motions. Thus, the numerical results obtained for different higher

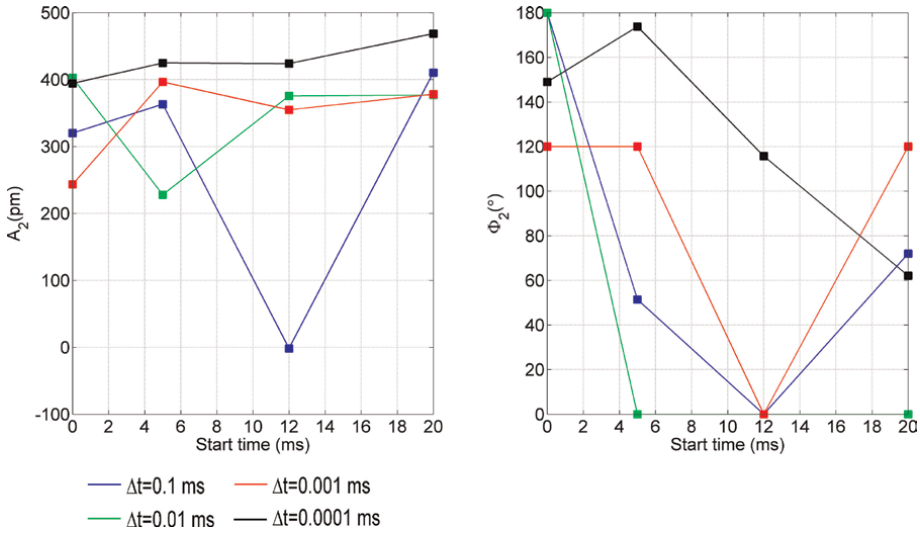

Figure 7.
Observable responses at the second eigenmode to acoustic force strength of 100 pN at the angular frequency of 1927.1 kHz on the domain of start time of numerical simulation for the initial displacement of 0 nm and for varied time intervals. (a) Amplitude. (b) Phase shift.

eigenmodes can be performed utilizing different time intervals so that the theoretical results can be matched with the experimental measurements or the results of different simulation software tools.

3.3 Effects of initial displacements

Initial boundary conditions such as initial displacement and velocity are to be selected properly to quantify the micro-cantilever sensitivity to acoustic forces effectively *via* numerical simulation. Mechanical systems might have different working conditions, which determine the initial boundary conditions. The forced Van der Pol-Rayleigh-Mathieu oscillator based second-order differential equation is solved considering these conditions illustrated in **Figures 8** and **9**. Initial displacements demonstrate a significant role in the determination of kinematic behaviors of the micro-cantilever under external forces on the particular time domain. Initial displacements affect the restoring energy acting on the effective mass, thereby determining the oscillation observables such as amplitude and phase shift. For a damped harmonic oscillator, analytical calculations of amplitude and phase shift are simply performed utilizing the initial amplitudes [23]. As expected, the vibration frequency of the micro-cantilever remains constant irrespective of how far the effective mass is placed from its equilibrium point. Essentially, the vibration frequency strongly depends on the elastic stiffness and effective mass of the micro-cantilever. For the present study, initial displacements significantly affect the displacements and velocities of the micro-cantilever under driving and acoustic forces on the particular time domains.

From the initial displacement of 5–20 nm for the first eigenmode, the deflection amplitudes continuously decrease to the smaller values at the picometer scale (**Figure 8(b–d)**). A similar trend is also observed for the second eigenmode

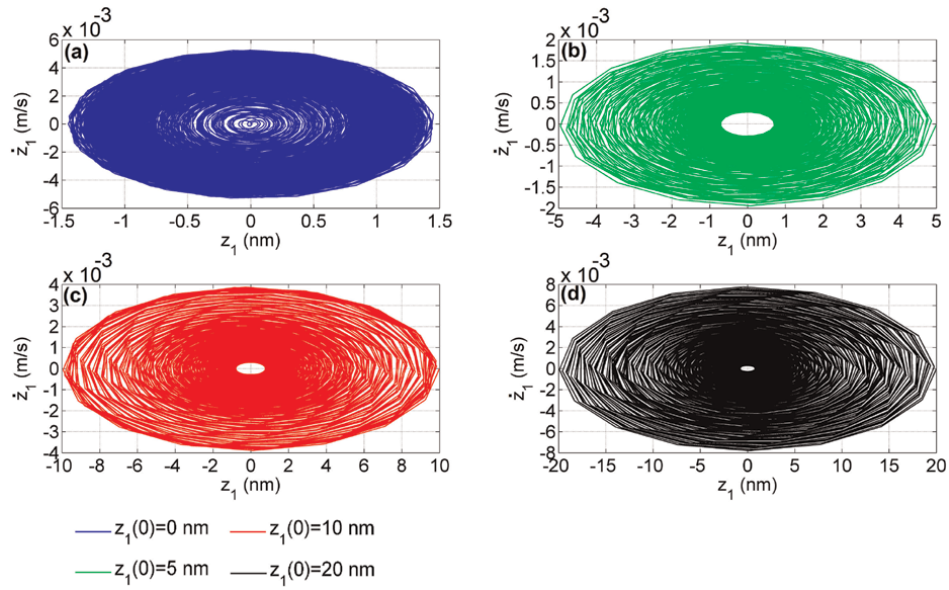

Figure 8.
Dynamic responses of the resonantly driven micro-cantilever at the first eigenmode to the acoustic force strength of 100 pN at the angular frequency of 307.25 kHz for the start time of 0 ms, the time interval of 0.001 ms, and diverse initial displacements.

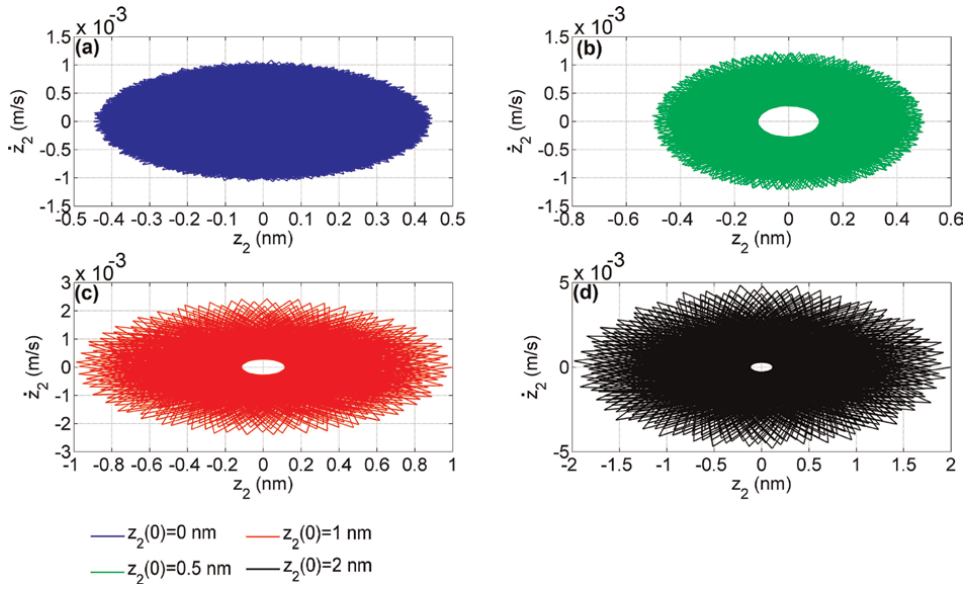

Figure 9.
Dynamic responses of the resonantly driven micro-cantilever at the second eigenmode to the acoustic force strength of 100 pN at the angular frequency of 1927.1 kHz for the start time of 0 ms, the time interval of 0.001 ms, and diverse initial displacements.

considering the initial displacement between 0.5 and 2 nm (**Figure 9(b–d)**). In addition, the second eigenmode exhibits different response patterns from the first eigenmode for relatively larger displacements and velocities. Thus, dynamic acoustic force sensitivity is to be examined considering the accurate initial boundary conditions that are based on operating conditions of the micro-cantilever under external forces.

4. Conclusions

In the numerical simulations, the responsiveness of the micro-cantilever is significantly dependent on the numerical simulation parameters, such as the start time, the time interval, and the initial displacements. The oscillation observables such as amplitude and phase shift can be extracted from the steady oscillations and the variations in the observables can utilized to quantify the micro-cantilever sensitivity to acoustic forces. The remarkable variations in amplitude responses are noted for different start times and time intervals. In addition to that, the phase shift exhibits quite notable responsiveness to varied start times and time intervals and correspondingly, the periodic responses can be acquired by adjusting those parameters in numerical computations. More significantly, the fundamental and higher eigenmodes might require different values of time intervals while obtaining single-frequency displacements. Thus, numerical simulation parameters are to be optimized for matching the numerical results with the experimental measurements or the analytical results obtained using different theoretical methods. Selecting time intervals is much more crucial while obtaining periodic responses to acoustic forces. The time interval is to be set to a much smaller value at the expense of longer computation time so that much more accurate periodic responses to acoustic forces can be obtained for the particular time

domains. More significantly, the quantification of sensitivity to external forces strongly depends on the selected time period since oscillation observables considerably change with varying time periods. It is also worth mentioning that the frequency responses do not change in the time domain as the numerical simulation parameters vary as expected. This result suggests that the varied values of numerical simulation parameters should be considered while conducting sensitivity analysis on external force sensitivity based on the amplitude and phase shift responses, rather than frequency shifts. Moreover, while obtaining the flexural displacements at different eigenmodes, the initial displacements are to be set considering the operating conditions of the micro-cantilever under external forces. The micro-cantilever approaches from the initial displacement within the range of 0–20 nm to the values at the picometer scale for the first eigenmode. For relatively larger displacements and velocities, the second eigenmode demonstrates different response patterns compared with the first eigenmode. Determining proper initial conditions is quite crucial for enhanced analysis of micro-cantilever sensitivity to acoustic forces. Thus, the effects of the numerical simulation parameters are to be considered while quantifying the sensitivity of the resonantly driven micro-cantilever to dynamic acoustic forces. Establishing more accurate dynamic models is vital for matching measurements of acoustic forces with different patterns in various operating environments. Mechanical characteristics of the microstructures and properties of the operating media can be obtained theoretically and experimentally by utilizing the highly sensitive responses of the microstructures under acoustic forces. Correspondingly, the resonance behaviors of the micro-cantilevers with different designs are considered to enhance their interactions with the acoustic forces for technological applications in biophysics, nanotechnology, and acoustic engineering fields.

Author details

Cagri Yilmaz
Akdeniz University, Vocational School of Technical Sciences, Antalya, Türkiye

*Address all correspondence to: cagriyilmaz@akdeniz.edu.tr

References

[1] Lozano JR, Garcia R. Theory of multifrequency atomic force microscopy. Physical Review Letters. 2008;**100**:076102. DOI: 10.1103/PhysRevLett.100.076102

[2] An S, Solares SD, Santos S, Ebeling D. Energy transfer between eigenmodes in multimodal atomic force microscopy. Nanotechnology. 2014;**25**:475701. DOI: 10.1088/0957-4484/25/47/475701

[3] Yilmaz C, Sahin R, Topal ES. Exploring the static acoustic force sensitivity using AFM micro-cantilever under single- and bimodal-frequency excitation. Measurement Science and Technology. 2021;**32**:115001. DOI: 10.1088/1361-6501/ac0eb1

[4] Yilmaz C, Sahin R, Topal ES. Theoretical study on the sensitivity of dynamic acoustic force measurement through monomodal and bimodal excitations of rectangular micro-cantilever. Engineering Research Express. 2021;**3**:045035. DOI: 10.1088/2631-8695/ac3a55

[5] Hellemann J, Müller F, Msall M, Santos PV, Ludwig S. Determining amplitudes of standing surface acoustic waves via atomic force microscopy. Physical Review Applied. 2022;**17**:044024. DOI: 10.1103/PhysRevApplied.17.044024

[6] Tremmel F, Nagler O, Kutter C, Holmer R. Smart cantilever probe with integrated force and acoustic emission sensor. In: 2023 IEEE Sensors; 29 October–01 November 2023; Vienna, Austria. USA, Canada, Worldwide: IEEE; 2023. pp. 1-4

[7] Yin Y, Ren D, Wang Y, Gao D, Shi J. A MEMS capacitive resonator as an acoustic sensor for photoacoustic spectroscopy. In: 2023 IEEE Sensors; 29 October–01 November 2023; Vienna, Austria. 2023. pp. 1-4

[8] Degertekin FL, Hadimioglu B, Sulchek T, Quate CF. Actuation and characterization of atomic force microscope cantilevers in fluids by acoustic radiation pressure. Applied Physics Letters. 2001;**78**:1628. DOI: 10.1063/1.1354157

[9] Mochizuki T, Hosaka N, Koda R, Shigehara N, Masuda K. Feasibility of thin catheter manipulation in the capillary blood vessel using acoustic radiation force. In: 2013 IEEE International Ultrasonics Symposium (IUS); 21–25 July 2013; Prague, Czech Republic. USA, Canada, Worldwide: IEEE; 2013. pp. 942-945

[10] Verbiest GJ, Oosterkamp TH, Rost MJ. Cantilever dynamics in heterodyne force microscopy. Ultramicroscopy. 2013;**135**:113-120. DOI: 10.1016/j.ultramic.2013.07.008

[11] Huang X, Shan H, Chu W, Chen Y. Computational and mathematical simulation for the size-dependent dynamic behavior of the high-order FG nanotubes, including the porosity under the thermal effects. Advances in Nano Research. 2022;**12**:101-115. DOI: 10.12989/anr.2022.12.1.101

[12] Hayden VC, Rahman SMS, Beaulieu LY. Computational analysis of the effect of surface roughness on the deflection of a gold coated silicon micro-cantilever. Journal of Applied Physics. 2013;**113**:054501. DOI: 10.1063/1.4789355

[13] Chen Y, Chen W, Wang L, Zhao F. Analysis and test of the inflatable tubes of ETFE foils. Applied Mechanics and

Materials. 2013;**351-352**:892-896. DOI: 10.4028/www.scientific.net/AMM.351-352.892

[14] Tan G, Shan J, Wu C, Wang W. Direct and inverse problems on free vibration of cracked multiple I-section beam with different boundary conditions. Advances in Mechanical Engineering. 2017;**9**:1-17. DOI: 10.1177/1687814017737261

[15] Öztürk S, Doran B, Aksoylar C. Effect of time step interval and time integration schemes in Pseudo-dynamic analysis. Structure. 2023;**50**:215-230. DOI: 10.1016/j.istruc.2023.02.013

[16] Hilton HH, Yi S. Generalized viscoelastic 1-DOF deterministic nonlinear oscillators. Nonlinear Dynamics. 2004;**36**:281-298. DOI: 10.1023/B:NODY.0000045520.93189.fe

[17] El-Dib YO. The damping Helmholtz–Rayleigh–Duffing oscillator with the non-perturbative approach. Mathematics and Computers in Simulation. 2022;**194**:552-562. DOI: 10.1016/j.matcom.2021.12.014

[18] Alyousef HA, Salas AH, Alkhateeb SA, El-Tantawy SA. Some novel analytical approximations to the (un)damped Duffing–Mathieu oscillators. Journal of Mathematics. 2022; **2022**:2715767. DOI: 10.1155/2022/2715767

[19] Akplogan ARO, Adjai KKD, Akande J, Avossevou GYH, Monsia MD. Modified Van der Pol-Helmholtz oscillator equation with exact harmonic solutions25 January 2022. PREPRINT (Version 1) available at Research Square. DOI: 10.21203/rs.3.rs-1229125/v1

[20] Yilmaz C. A multi-modal nonlinear dynamic model to investigate time-domain responses of a micro-cantilever in fluids. Engineering Research Express. 2024;**6**:025509. DOI: 10.1088/2631-8695/ad3c13

[21] Yilmaz C. Theoretical and experimental approaches for fluidic AFM operations and rheological measurements using micro-cantilevers. Journal of the Brazilian Society of Mechanical Sciences and Engineering. 2024;**46**:398. DOI: 10.1007/s40430-024-04964-1

[22] Solares SD, An S, Long CJ. Multi-frequency tapping-mode atomic force microscopy beyond three eigenmodes in ambient air. Beilstein Journal of Nanotechnology. 2014;**5**:1637-1648. DOI: 10.3762/bjnano.5.175

[23] Bhushan B. Springer Handbook of Nanotechnology. 3rd ed. Berlin, Heidelberg: Springer; 2010. 1964 p. DOI: 10.1007/978-3-642-02525-9

Chapter 2

Acoustic Monitoring of the Coal-Rock Massif State in Stress-Strain Zones during Hydroimpulsive Impact: Application Experience

Vasyl Zberovskyi, Ruslan Ahaiev, Vasyl Vlasenko and Maryna Kyrychenko

Abstract

The paper presents the results of acoustic monitoring studies on the state of coal-rock massif during the hydroimpulsive loosening of outburst-hazardous coal seams in the working faces of development workings. The parameters of the cavitation device and the regularities in the development of periodically discontinuous fluid flow, which manifests on the coal surface as high-frequency hydroimpulsive vibration and generates secondary vibrations in the coal-rock massif, are considered. The main methodological regulations for the use of acoustic monitoring systems in the mines of Ukraine and the parameters for evaluating the effectiveness of control methods on the stress–strain state of the outburst-hazardous massif are presented. The results of using acoustic systems in the study of the coal-rock massif state and the criteria substantiation for controlling and evaluating the effectiveness of hydroloosening of outburst-hazardous coal seams are considered. A comparison of the results of theoretical, laboratory, and mining-experimental studies under the conditions of the mines of "Krasnodonvuhillia" was performed.

Keywords: acoustic monitoring, stress-strain state, development workings, cavitation device, hydroloosening

1. Introduction

Solving the problem of safe operations in seams prone to gas-dynamic phenomena (GDP) and controlling the stress–strain state (SSS) of the coal-rock massif is one of the most challenging issues in the coal industry of all coal deposits worldwide, including Ukraine.

The most difficult conditions for stopping outburst-hazardous coal seams are created in abutment pressure zones and when conducting development workings in

unprotected areas. The use of additional measures to prevent sudden outbursts of coal and gas does not always ensure the safety of mining. That is why cases of GDP with catastrophic consequences still occur. Ukrainian mines in hazardous areas use concussion blasting, which leads to a reduction in the number of coal mining shifts, a decrease in the development of workings from 6 to 2 meters per day, and an increase in product costs.

For many decades, the Institute of Geotechnical Mechanics of the National Academy of Sciences of Ukraine (IGTM NASU) has been conducting research on the stress–strain state of coal-rock massif in various scientific and technical areas. One of these areas is the development and implementation of methods to prevent GDP, including sudden outbursts of coal and gas. In accordance with the Safety Rules of Ukraine, the development of new methods and their implementation takes place only with the permission of the Central Commission for Ventilation, Degassing, and Control of Gas Dynamic Phenomena in Mines of the Coal Industry of Ukraine (hereinafter "Central Commission ... ") [1]. Among the developed methods, special attention is paid to the control of the stress–strain state of the coal-rock massif by using hydrodynamic impact modes based on the effect of cavitation fluid flow.

The analysis of experimental studies of cavitation pulse generators of liquid pressure developed on the basis of a Venturi tube [2–8] allowed us to substantiate and develop a device for hydroimpulsive impact [9]. Laboratory and mining-experimental studies have shown high reliability and efficiency in its performance. However, during the study of the device in the working faces of the development workings, several scientific and technical issues arose that were solved experimentally. Therefore, the properties of outburst-hazardous coal, the amplitude–frequency characteristics (AFC) of the Venturi tube, and the design parameters of the device were studied simultaneously. This made it possible to develop a new method of hydroimpulsive loosening of outburst-hazardous coal seams [10].

Difficulties arising from the implementation of the device due to the fact that:

- to date, the impact of anthropogenic factors on the stress–strain state of a outburst-hazardous coal seam in a great depth conditions has not been sufficiently studied;
- the mechanism of the hydroloosening process impact on the state, structure, and design of outburst-hazardous coal, which has a globular structure and is considered as a coal-gas system, is poorly understood;
- the process of changing the stress–strain state, design and structure of outburst-hazardous coal under its hydroimpulsive loading is unexplored;
- there is no methodology for calculating the parameters and methods of controlling hydroimpulsive impact, studying the shear deformations of the coal-rock massif and its response to hydroimpulsive impact.

The directions for solving these issues and the research results were considered and agreed upon by the Decisions of the "Central Commission ... ".

At Ukrainian mines, acoustic monitoring methods are used to control the stress–strain state of the coal-rock massif and to predict the GDP (sudden outburst of coal and gas). At the same time, there is no acoustic control of the methods parameters of

preventing the GDP during preventive measures and evaluation of their effectiveness. This area, despite the technological necessity, is poorly studied.

Therefore, the experience of using acoustic monitoring of the state of outburst-hazardous coal seams to control the parameters of the hydroimpulsive loosening method and establish a safe coal recovery zone is relevant.

The purpose of the paper is to analyze the results of acoustic monitoring of the state of outburst-hazardous coal seams in the stress–strain state of the massif during the implementation of measures to prevent the sudden outburst coal and gas by hydroimpulsive impact in the mines of the Donetsk basin of Ukraine.

2. General information about the method of hydroimpulsive loosening of outburst-hazardous coal seams

In papers [2–6], some problems of developing the design of pressure pulse generator (PPG) for injecting fluid under high pressure into coal seams were solved. The use of these devices for coal humidification confirmed the high efficiency of the hydroimpulsive impact. The analysis of the results of these studies showed that the use of PPG allows creating cracks in the coal seam that form around the borehole in different directions. In other words, signs of hydroloosening process are formed in the massif. These circumstances made it possible to consider the conditions for using the method to prevent sudden outburst of coal and gas. For this purpose, after studying the parameters, amplitude–frequency characteristics (AFC) and operating ranges of all PPG modifications, its design was modernized. The schematic diagram of the new design of the generator of liquid pressure cavitation self-oscillations, hereinafter referred to as the cavitation generator (CG) or generator, is shown in **Figure 1**, and its main parameters are shown in **Table 1**.

The generator consists of: a Venturi tube (1) with a critical cross-section d_{cr} (2) and a cavitation chamber diffuser (3) with a diffuser opening angle β; an inlet flow channel with a diameter of D_1 (4); a diffuser channel with a diameter of D (5). The generator is installed in the tip of the sealer (6). P_0 is a liquid pressure at the inlet of the generator, MPa; G is a liquid flow rate, l/min.

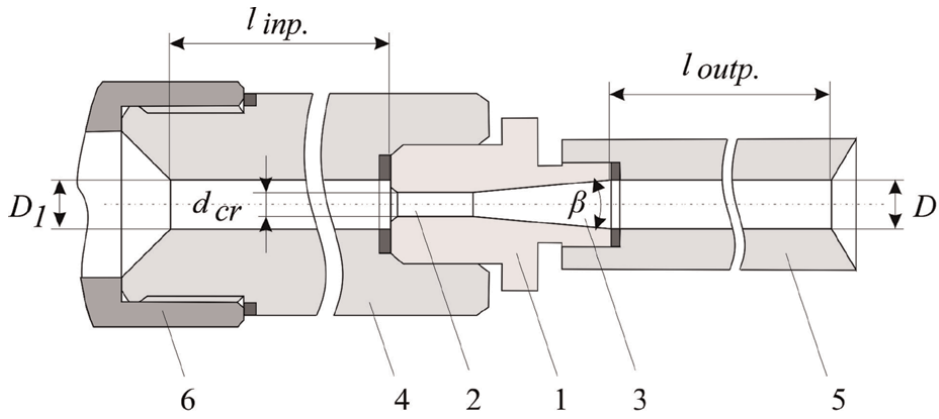

Figure 1.
Schematic diagram of the generator of liquid pressure cavitation self-oscillations (CG).

Type of generator	Hydraulic parameters	d_{cr}, mm	l_{cr}, mm	D_1, mm	D, mm	l_{in}, mm	l_{out} mm	β, deg
CG-2.5	P_0 = 170 G = 0.86	2.5	by calculation	10	$4d_{cr}$	$10D_1$	$100d_{cr}$	20

Table 1.
Geometric parameters of the CG-2.5 generator.

The set of theoretical, laboratory, and bench tests of CG-2.5 allowed us to establish the following:

- the dynamic parameters of the CG-2.5 generator correspond to the hydraulic parameters of pumping units used for hydroloosening of coal seams at depths of more than 600 meters;
- the established regularities of development of the generator's amplitude–frequency characteristic as a function of the cavitation parameter allow us to study the discrete pulse flow of fluid in the borehole simulator;
- based on the results of mining-experimental studies of CG-2.5, the criterion for controlling the AFC of generator by the fluid boost pressure in the borehole was established;
- based on the results obtained, the regularities of the AFC generator development as a function of the fluid boost pressure in the borehole were established;
- during acoustic monitoring of the stress–strain state of the coal-rock massif, the following were identified: the influence zone of hydroimpulsive impact, the zone of massif unloading ahead of the working face of the development workings, and the safe coal recovery zone;
- based on the research results, a method of hydroimpulsive loosening of outburst-hazardous coal seams was developed.

According to the mining and geological conditions of Krasnodonvuhillia mines, the depth of development of outburst-hazardous coal seams ranges from 600 m to 1300 m. According to [1], the maximum value of pressure pulses should not exceed $0.75\gamma H$. The lower limit should meet the criterion of hydroloosening efficiency that is a decrease in discharge pressure by at least 30%. Therefore, the range of calculated values of the discharge pressure will be $0.52\gamma H \le P_d \le 0.75\gamma H$ or, according to the calculations, $8 \le P_d \le 28$ MPa. Therefore, in theoretical and laboratory studies, the change in the amplitude of self-oscillations and their frequency was studied at an discharge pressure P_d (generator inlet pressure P_0) from 5.0 MPa to 30.0 MPa and a fluid boost pressure in the borehole P_b from 0.0 to 14.0 MPa.

According to the results of bench tests, it was found that fluid discharge modes up to 15 MPa correspond to the conditions of coal seams at depths of up to 700 meters. The operating range of the generator is $0.1 \le P_b \le 12.0$ MPa. Depths from 700 to 1300 meters correspond to discharge modes from 15.0 MPa to 25.0 MPa. In this case, the upper limit of the operating range is $P_b \le 0.82\ P_d$. The operating range of the generator is determined by the frequency of fluid pressure pulses within the values of

the self-oscillation range at which, according to the value of the elastic modulus of coal, its destruction is ensured.

Taking into account the results of mining-experimental studies of acoustic monitoring of the process of hydroimpulsive impact, which will be given below as an example, we will consider the change in the dynamic parameters of CG-2.5 at the discharge mode P_d = 10 MPa (**Figure 2**).

The fluid pressure self-oscillations range is defined as $\Delta P = p_{max}$-p_{min}, where p_{max} is the maximum pressure value in the pulse; p_{min} is the minimum pressure value in the pulse.

According to the results of the research, it was found that at a discharge pressure of P_d (P_0) = 10 MPa, a stable cavitation flow of fluid in the hydraulic system is observed in the range of boost pressure from P_b = 0.1 MPa to P_b = 8.0 MPa, the maximum self-oscillations range ΔP_{max} is achieved at $P_b \approx 1.7$ MPa, and the process is completed at $P_b \approx 9.0$ MPa. The established regularities of the self-oscillations range on the boost pressure at P_d = 10 MPa are described with sufficient accuracy by fourth-order polynomial equations:

$$\mathrm{P} = -0.07\mathrm{P}_b^4 + 1.49\mathrm{P}_b^3 - 10.63\mathrm{P}_b^2 + 25.79\mathrm{P}_b + 4.88, R^2 = 0.76; \quad (1)$$

In accordance with the established regularities of the development of the frequency of self-oscillations f on the boost pressure P_b at P_d = 5;10;15 MPa (**Figure 3**), their growth occurs with an increase in the discharge pressure and the boost pressure of the fluid in the borehole.

The established regularities are described by linear equations with high levels of determination factor. At the mode under consideration, P_d = 10 MPa, the equation has the form

$$f = 0.71\mathrm{P}_b + 0.95, R^2 = 0.95 \quad (2)$$

Comparing the results of studies of the regularities of the self-oscillation range development (**Figure 2**) and the frequency of their passage (**Figure 3**), we determine the operating range of CG-2.5. At a discharge pressure of P_d (P_0) = 10 MPa, a stable mode of cavitation fluid flow in the hydraulic system is observed at values of the fluid pressure self-oscillation range of $1.0 \leq P_b \leq 8.0$ MPa. At which the maximum value of the pulse passage is observed at P_b = 8.0 MPa, and the minimum at P_b = 1.0 MPa.

It is known that sudden outburst or bounce in the interval of deformation development at a rate of 1–10 s^{-1} causes a sharp drop in coal strength. At a strain rate of

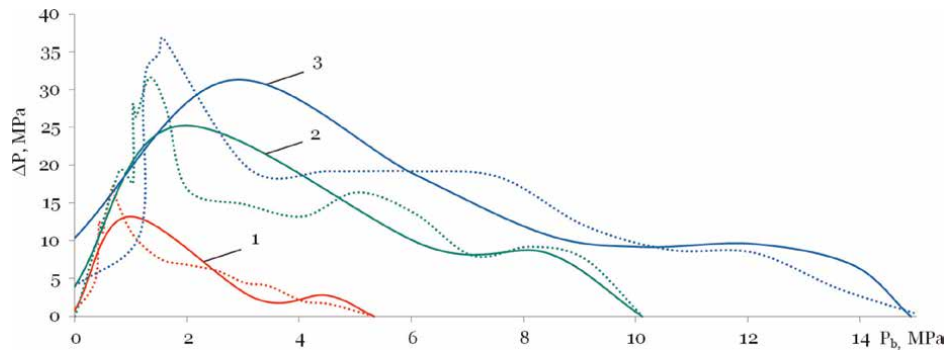

Figure 2.
Regularities of development of the fluid pressure self-oscillations range ΔP *in a borehole simulator at* P_d = *5, 10, 15 MPa.*

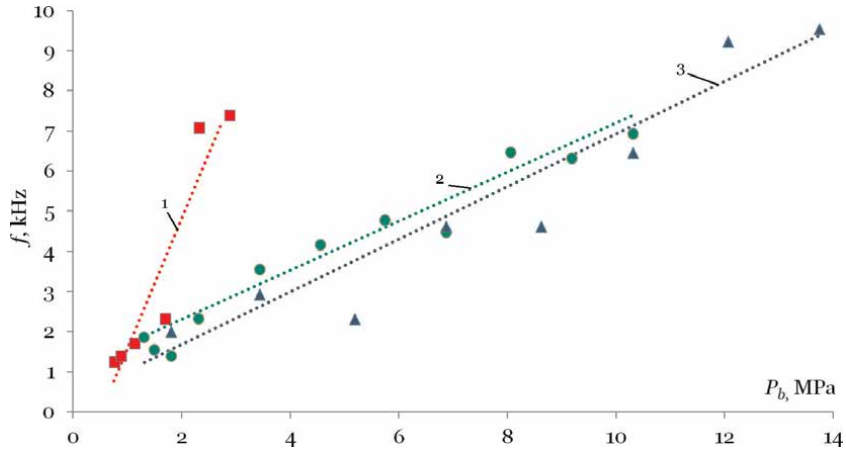

Figure 3.
Regularities of development of the self-oscillations frequency f *as a function of boost pressure* P_b *in the operating range at* P_d *= 5;10;15 MPa.*

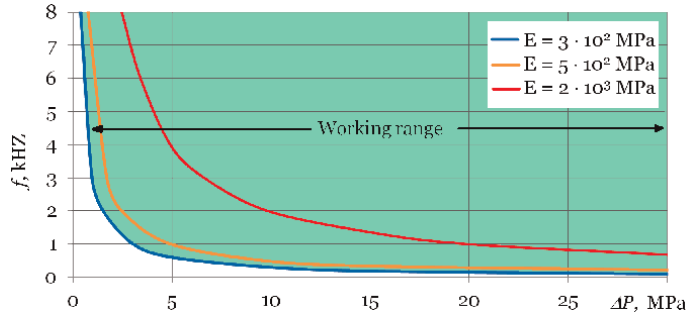

Figure 4.
Theoretical regularities of the minimum values of pressure pulses ΔP *on the frequency of their passage* f *for the values of the elastic modulus of coal* E = *3 · 10² MPa; 5· 10² MPa; 2· 10³ MPa at the rate of deformation development* $\dot{\varepsilon} \geq 10\ s^{-1}$.

more than $\dot{\varepsilon}$ = 10 s^{-1}, shear deformations are initiated. The destruction of coal under pressure depends on its elastic modulus (Young's modulus E). Under hydroimpulsive impact, coal destruction beyond the limit value of the strain development rate will occur under impulse loading Eq. (3) [11–13].

$$\acute{\varepsilon} = \frac{d\varepsilon}{dt} = \frac{\Delta P \bullet f}{E}, \ = \Delta P = \frac{10E}{f}, MPa, \tag{3}$$

It is known that the elastic modulus of coal behind the layering is in the range of $3 \bullet 10^2 \leq E \leq 5 \bullet 10^2$ MPa, and perpendicular to the layering is up to $E = 2 \bullet 10^3$ MPa. According to the established regularity (3), at the minimum values of the oscillation range and frequency, the AFC of the generator was calculated (**Figure 4**). According to the calculations, the minimum required values of pressure pulses, at the maximum values of $E = 2 \cdot 10^3$ MPa, are from 3.0 MPa to 20.0 MPa at a pulse passage rate of 7.0 kHz to 1.0 kHz, respectively.

Taking into account the results of studies [14, 15], according to which it was found that the destruction of outburst-hazardous coal does not depend on the direction of its

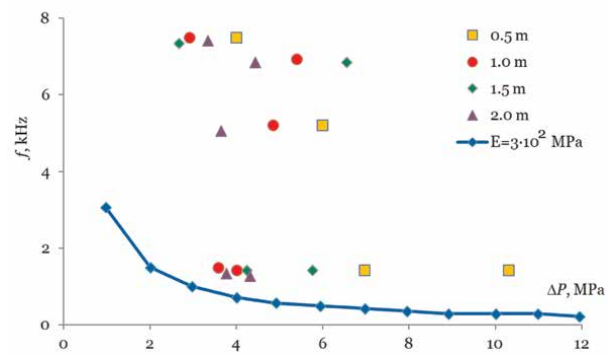

Figure 5.
Comparison of the experimental values of the AFC of generator and rate of strain development ε̇ at elastic modulus $E = 3\ 10^2$ *MPa.*

loading, the experimental values of the AFC of the CG-2.5 generator are compared with the conditions of coal destruction at a strain rate of $\dot{\varepsilon} = 10\ s^{-1}$ and $E \geq 3 \cdot 10^2$ MPa (experimental measurement points in the borehole simulator at a distance from the generator) (**Figure 5**).

According to the obtained results, all the established values of the AFC of generator are located above the strain rate curve with $\dot{\varepsilon} = 10\ s^{-1}$ at $E = 3 \cdot 10^2$ MPa. Therefore, when hydroimpulsive impact on outburst-hazardous coal seams, the range of operating modes of CG-2.5 consists of values of pressure pulses ΔP from 3.0 MPa to 30.0 MPa at a frequency of their passage from 0.8 kHz to 8.0 kHz.

3. Methodological bases of acoustic monitoring of hydroimpulsive impact

The analysis of the results of studies of changes in the parameters of the stress–strain state of coal seams ahead of working faces using acoustic monitoring of hydroimpulsive impact allowed us to obtain the following. Firstly, the methods of acoustic monitoring were established. This made it possible to study the parameters of acoustic monitoring in the complex of mining equipment used in Ukrainian mines and to establish rational technological solutions to assess the effectiveness of the developed method. Second, to study the parameters of changes in the stress–strain state of the coal-rock massif and to determine the response of the massif to its dynamic loading.

The use of seismic and acoustic signal transmission equipment (SASTE) and sound pickup equipment (SPE) was carried out by the decision of the "Central Commission ... " in accordance with the developed "Annex to the Design Technological Documentation ... " [1]. According to the results of the research, the following was established.

1. When assessing the change in the stress–strain state of a coal-rock massif, it is rational to use the SASTE-1 system.

2. In the working faces of the development workings, both the SASTE-1 and the SPE-98 systems are efficiently used when they are driven by a shearer.

3. The SPE-98 system should be used to control the process of coal mining intensity.

In these studies, it is important to know about the features of acoustic monitoring systems that determine the parameters of changes in the stress–strain state of the coal-rock massif or the parameters of controlling the dynamic load of outburst-hazardous coal.

The essence of forecasting and controlling the outburst hazard of massif according to the parameters of the acoustic signal (AS) by the SASTE-1 system is the registration, processing, and analysis of the signal spectrum excited in the coal-rock massif during the technological process. A seismic receiver installed in the roof of the seam picks up signals from each rock layer. For example, if there are three layers in the seam roof, then three acoustic responses to excitation with different spectral compositions will be registered at the measurement point (**Figure 6**).

The elastic vibrations occurring in the massif, reflected from the boundaries of rock layers, spread along the surfaces of the formation with a certain velocity and frequency. The recorded information is processed on a personal computer using the "Zond" program.

If there are weakened contacts in the massif, then natural (resonant) oscillations occur in the rock layer, the frequency of which is inversely proportional to the layer thickness, and the amplitude depends on the contact weakening. By means of a fast Fourier transform, the spectrum of the acoustic signal is calculated, and the resonant frequencies (f_r, Hz) are distinguished, which are related to the distance to the weakened contacts (h, m) by the ratio

$$f_r = \frac{c}{h}, Hz \tag{4}$$

where c is the phase velocity of cross waves, which for most roof sedimentary rocks is 2500 m/s.

The ratio of the high-frequency component of the spectrum f_u to the low-frequency component f_l determines the outburst hazard factor $K_o = f_u/f_l$. It reflects the stressed state of the massif at the observation point in real time.

Thus, by its essence, parameters, and established features, the SASTE system corresponds to the direction of studying changes in the state of the coal-rock massif during the technological process.

The SPE-98 equipment is used to predict the outburst hazard based on the acoustic emission (AE) of a rock massif. To assess the state of the massif, the observation time interval is set, the number of AE pulses, their critical value, and AE activity are determined. The presence of a continuous AE or a series of AE pulses is assumed to be

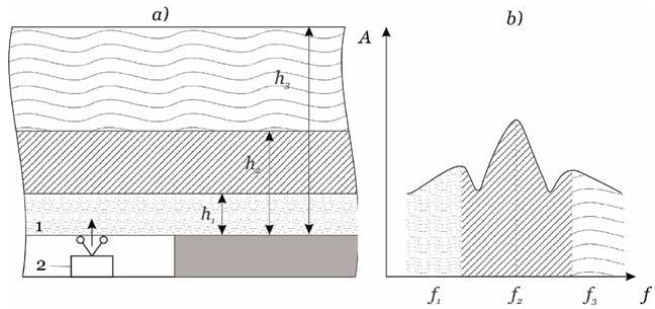

Figure 6.
Scheme for determining weakened contacts in roof rocks (a) and the corresponding acoustic signal spectra (b).

equivalent to the critical AE value. The forecast "dangerous" is issued by the operator of the forecast service in accordance with the methodology of using SPE-98.

For example, a borehole is drilled at meter intervals. At each interval of borehole drilling, a profile of the activity of the recorded AE signals is built in the form of the specific number of AE pulses per meter of the borehole (**Figure 7**).

The oscillogram and signal spectrum are determined and displayed on the system operator's monitor by means of automatic registration of AE pulses against the background of acoustic process accompaniment (**Figure 8**).

Using the drilling schedule and established acoustic emission activity profiles, stress changes along the length of the borehole are estimated. This allows for operational control of the coal recovery rate in the working faces of the development workings and stope.

The essence of the process control using the SPE-98 system is to control and assess the massif state based on the results of registering the AE arising during the technological process, its temporary suspension, and resumption upon notification of the mine forecasting service operator. In other words, the parameters of loading of the outburst-hazardous coal, which influence the change in its state, are used to control the parameters of the technological process by means of acoustic monitoring.

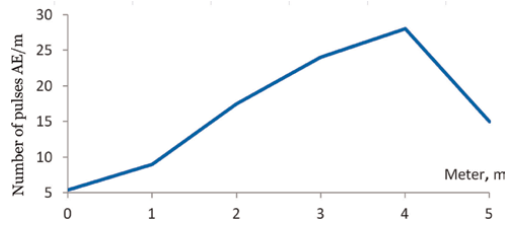

Figure 7.
Example of the AE activity profile along the length of the borehole.

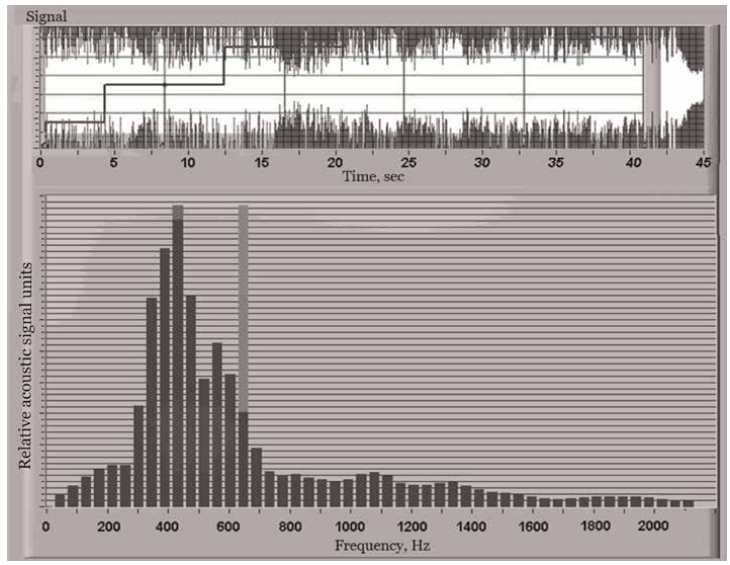

Figure 8.
Interface of the "spectral processing" program.

The parameters of acoustic monitoring and the study of the state of a stress–strain outburst-hazardous coal-rock massif were substantiated during the hydroimpulsive loosening in the working faces of the development workings. The analysis of scientific developments showed that there are no similar studies to solve the problem of sudden coal and gas outburst in the development workings [16–18].

4. Results of acoustic monitoring of the coal-rock massif state in stress–strain zones under hydroimpulsive impact

The study of the acoustic monitoring parameters of hydroloosening process in outburst-hazardous coal seams was performed in the mines of Public Joint Stock Company (PJSC) "Krasnodonvuhillia". The total volume of research amounted to 65 cycles, of which pulse discharge was 30 cycles. During this time, more than 1.2 km of development workings were driven.

The obtained results were considered at the meeting of the Bureau of the "Central Commission ... ", approved and accepted for industrial implementation. During the research, a database of experimental data on the parameters of control and evaluation of the effectiveness of hydroimpulsive loosening of outburst-hazardous coal seams was formulated, and parameters for control and evaluation of the method efficiency were developed [19, 20].

The use of acoustic monitoring of hydroloosening parameters in outburst-hazardous coal seams using the SASTE-1 and SPE-98 systems allowed solving a complex scientific and technical problem: to consider and evaluate the change in the stress–strain state of the coal-rock massif as a complex dynamic system consisting of a hydraulic component and a porous coal-rock medium, to consider the process "hydrodynamic load–rock massif–rock response".

The SASTE-1 system was used to study the static and pulsed discharge modes, determine the advantages of hydroimpulsive impact and changes in the stress–strain state of the roof rocks, which affect the coal seam unloading zone ahead of the face.

The SPE-98 system was used as an additional control method to study the state of the coal seam and the parameters of the new design of the cavitation device. The following provisions were taken into account when adapting the acoustic parameters to the process of hydroimpulsive loosening [21]:

- continuous AE occurs in conditions where localized stresses in the massif exceed the strength of the coal;
- AE is a response to a disturbance in the equilibrium of the stresses existing in the massif, i.e., to the mechanism of technological impact;
- monitoring of the acoustic signal and process parameters takes place remotely without disturbing the experimental conditions;
- in the system "hydrodynamic load–massif–massif response", the parameters of load and massif response are considered simultaneously.

Let us consider the results of the analysis, scientific and technical conclusions established during the acoustic monitoring of the coal-rock massif state in stress–strain zones under hydroimpulsive impact and make a comprehensive assessment of them.

4.1 Results of monitoring and evaluation of the effectiveness of hydroimpulsive impact by the SASTE-1 system

The study of the parameters of hydroimpulsive impact on the outburst-hazardous coal seams based on the results of control by the SASTE-1 system was performed in the conditions of the "Duvanna" mine and the "Sukhodilske-Skhidne"-Mine Administration". The effectiveness of the hydroimpulsive impact was evaluated by comparing the results of the new method with the parameters of the standard method (hydroloosening in the static mode of fluid discharge) [1]. The results of these studies are presented in scientific reports of the Institute of Geotechnical Mechanics of the National Academy of Sciences of Ukraine, and some in [22, 23].

Let us consider the sequence and general results of these studies. The procedure for conducting mining-experimental operations was carried out in accordance with the developed methodological and technical documentation. Initially, the working face of development working was driven according to the standard method of hydroloosening. The fluid discharge was stopped at the command of the SASTE-1 system operator "active process completed". If the discharge pressure dropped by at least 30% of the maximum set pressure, the process was considered effective. The parameters and results of fluid discharge were recorded in the hydroloosening log and stored in the computer database of the SASTE-1 operator, which formed the experimental database.

The research results were processed using the "Forecast 4.0" software package. This made it possible to record the time of fluid discharge, maximum and final discharge pressure, the period of active hydroloosening, calculate the outburst hazard factor, and control the unloading zone during borehole drilling. Real-time monitoring results are displayed on the operator's computer monitor (**Figure 9**). Examples and analysis of these studies are discussed in [22, 23]. We note that the software package "PROGNOZ 4.0" (FORECAST 4.0) performs spectral analysis and calculation of low-frequency and high-frequency components, which determine the outburst hazard factor $K_o = f_u/f_l$, the safe depth of coal recovery, and evaluate the effectiveness of hydroloosening.

The control of hydroimpulsive impact parameters was performed in a similar sequence. However, the software package "PROGNOZ 4.0" ("Forecast 4.0") was designed to control the static pressure of the liquid. It did not take into account the peculiarities of hydroimpulsive impact. Therefore, directly in the course of the operation, it was improved and adapted to a constant pressure at the inlet of the cavitation device and separate control of the fluid boost pressure in the borehole. It was assumed that the maximum and final pressures correspond to the inlet pressure of the

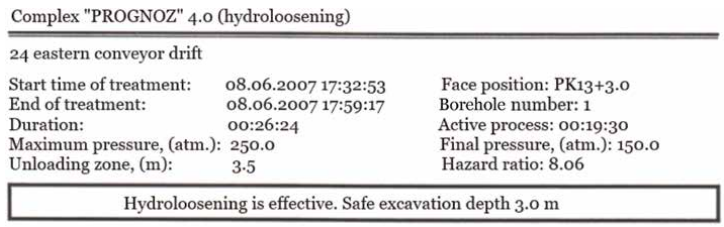

Figure 9.
Screenshot from the monitor of the SASTE-1 system operator when monitoring the process of hydroloosening.

Complex "PROGNOZ" 4.0 (hydroimpulsive impact)

24 eastern conveyor drift

Start time of treatment:	10.10.2007 12:40:13	Face position: PK40+4.0
End of treatment:	10.10.2007 12:52:21	Borehole number: 1
Duration:	00:12:08	Active process: 00:10:00
Maximum pressure, (atm.):	120.0	Final pressure, (atm.): 120.0
Unloading zone, (m):	6.0	Hazard ratio: 7.42

Hydroloosening is effective. Safe excavation depth 4.5 m

Figure 10.
Screenshot from the monitor of the SASTE-1 system operator while monitoring the process of hydroimpulsive impact.

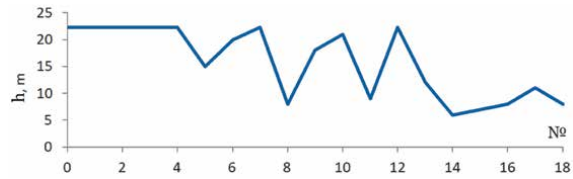

Figure 11.
Distribution of weakened contacts between rock layers in the reservoir roof after hydroimpulsive impact.

cavitation device, and the fluid boost pressure in the borehole is taken into account separately by the operator. All other parameters were calculated and displayed on the monitor (**Figure 10**).

Based on the results of comparing the control of static and pulsed discharge modes, it was found that under hydroimpulsive impact, the duration of the hydroloosening process and its active part are reduced by more than two times, and the fluid consumption is at least 50%.

By studying the change in the spectrum of the acoustic signal of the stress–strain state of the rock thickness in the seams roof at each cycle of fluid discharge, the resonant frequencies and the distance to the weakened contacts between the rock layers were determined (see **Figure 6**). Comparison of the average statistical data of these parameters showed that during pulse discharge, rocks at a distance of up to 22.5 m are involved in the deformation process (**Figure 11**) [22, 23].

According to the results of studies of the low-frequency and high-frequency components of the acoustic signal spectrum, it was found that during the hydroimpulsive loosening of outburst-hazardous seams, the low-frequency component increases up to 74%, and the stress of the massif (K_o) decreases by at least 25% (**Figure 12**). This ensures a uniform (without delays) development of deformations in the coal seam roof at a distance of more than 10 m and an increase in the safe coal recovery zone to the depth of the borehole drilling.

According to the results of the research, it was found that acoustic monitoring by the SASTE-1 system using the adjusted software package "PROGNOZ 4.0" ("Forecast 4.0") allows controlling the parameters of the hydroimpulsive impact process and evaluating the effectiveness of hydroloosening by changing the stress–strain state of the coal-rock massif. And vice versa, based on the results of changes in the parameters of the massif state, to control the process of hydroloosening.

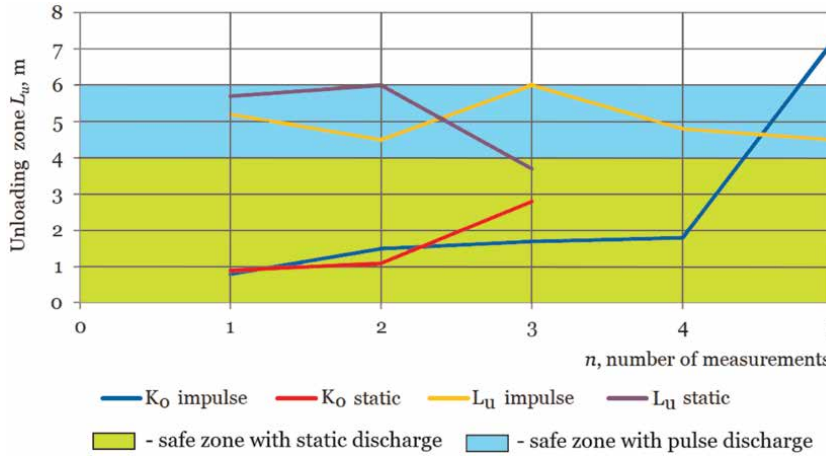

Figure 12.
Example of the results of determining the unloading zone in static and pulse modes of fluid discharge.

4.2 Results of control and evaluation of the effectiveness of hydroimpulsive impact by the SPE-98 equipment

Based on the results of the hydroimpulsive impact monitoring process by the SASTE-1 system, the decision of the "Central Commission ... " allowed to extend the study of the method parameters using the SPE-98 system. Due to the fact that the "Molodohvardiiske" Mine Administration had the necessary equipment for operational control of the intensity of technological processes by the SPE-98 system, these operations were performed in the conditions of the k_2^l and i_3^1 seams.

It should be noted that the study of the hydroloosening process of outburst-hazardous coal seams with the SPE-98 equipment was carried out for the first time in the practice. Some results of solving certain tasks were published in [22, 24–26], but a comprehensive assessment of acoustic monitoring of the coal-rock massif state in stress–strain zones under hydroimpulsive impact was not made.

Based on the results of the parameters analysis of methods for monitoring the outburst hazard of a coal massif, it was found that the spectra of the AE and continuous AE recordings are the most informative. At the same time, it is known that:

- in static fluid discharge modes, uncontrolled processes of hydraulic fracturing or hydraulic squeezing of the seam margin occur;
- The process of fluid discharge into coal is accompanied by the development of AE and continuous AE, but this phenomenon has not been studied;
- in the absence of a potentially dangerous condition of the massif, fluid discharge will be unnecessary, even if it is effective;
- the use of AE as a means of probing the massif during exploration borehole drilling allows monitoring the condition of the formation during the drilling of test and production boreholes during hydroloosening.

Therefore, the following provisions were taken into account when monitoring the stress–strain state of the massif under hydroimpulsive impact:

- during drilling, the initial zone of influence of the borehole is created around the drill bit. This allows the AE created around the drill bit to study the stress massif along the drilled borehole;

- installation of transmitters of SPE-98 equipment for monitoring AE signals arising in the area of the working drill bit should ensure a dynamic range of useful signals of at least 70 dB and high quality of all information coming from the working face. Therefore, it should be installed at a distance of one to two meters from the face line;

- the activity profile of AE signals recorded as the specific number of AE pulses is built at meter intervals. The service of seismic and acoustic forecasting at mines has a package of application programs for acoustic signal processing.

Thus, based on the results of registering the AE that occurs when drilling exploration, production and control boreholes under hydroimpulsive impact, it is possible to monitor and assess the state of the massif before, during and after the technological process.

As an example, consider the results of research obtained during mining-experimental operation in the conditions of the seam k_2^l 617 m horizon at "Molodohvardiiske" Mine Administration.

Based on the AE activity profile and the drilling length of production boreholes (**Figure 13**), it was found that under these conditions the maximum stresses in the massif are concentrated at a distance of 4.0 m ahead of the working face. Therefore, when using 6.0-meter deep production boreholes with a sealing depth of 4.0 m, its filtration part will be outside the zone of maximum stresses. Such parameters increase the reliability of sealing and reduce the probability of fluid breakthrough into the produced space. At the same time, the probability of hydraulic squeezing remains.

According to the calculations, it was found that under these conditions, the value of the hydraulic fracturing pressure is $P_{h.p.}$ = 12.2 MPa, and the pressure of hydroimpulsive impact is P_d = 10.3 MPa. Based on this, the range of fluid pressure at the generator inlet was set at $10.0 \leq P_d \leq 12.0$ MPa. Therefore, the liquid was discharged at a pressure of ≈11.0 MPa.

According to the calculations, it was found that under these conditions, the value of the hydraulic fracturing pressure is $P_{h.p.}$ = 12.2 MPa, and the pressure of

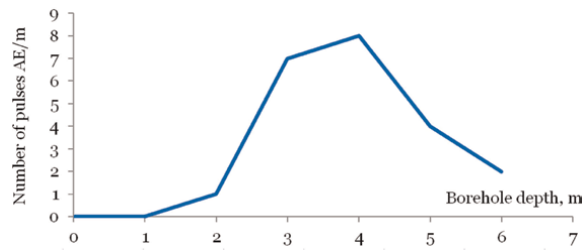

Figure 13.
Profile of AE activity along the drilling length of production borehole in the the seam k_2^{II} *617 m horizon at "Molodohvardiiske" Mine Administration.*

hydroimpulsive impact is P_d = 10.3 MPa. Based on this, the range of fluid pressure at the generator inlet was set at $10.0 \leq P_d \leq 12.0$ MPa. Therefore, the liquid was discharged at a pressure of ≈11.0 MPa.

According to [1], hydroloosening of an outburst-hazardous coal seam in the working face of a development workings should be carried out through two boreholes located in the corners of the workings. In this case, the distance between the borehole faces is from 4.0 m to 6.0 m. During the sound accompaniment of the process of hydroimpulsive impact and comparison of amplitude–frequency spectra, it was found that high-frequency spectra were recorded in borehole No. 1 (in the order of development). Based on the results of their processing, it was found that they relate to high-frequency oscillations of the CG-2.5 generator. The energy of these oscillations is spread in the fluid that fills the filtration space of the borehole. Stress transformation occurs in the massif, which generates ultrasonic vibrations in the liquid. These changes are recorded by SPE in the form of secondary vibrations of the coal massif in a wide frequency range. Some of them, low-frequency vibrations (LF), are associated with electrical interference (100–150 Hz) and the stressed state of the massif (200–800 Hz). The high-frequency (HF) component of the spectrum is associated with the pulses generated by CG-2.5 and contains peaks up to 3000 Hz. In borehole No. 2, the fluid discharge process is not accompanied by intense AE pulses, and the spectrum does not contain a high-frequency component with a high energy level. In addition, the frequency spectrum does not include the range of generator operation up to 3000 Hz. Based on the analysis of the results obtained, it was concluded that the use of the second borehole does not make sense.

The obtained results of acoustic monitoring made it possible to consider the feedback of the massif response to the hydroimpulsive impact and to assess the nature of changes in the generator operating modes when the fluid boost pressure in the borehole changes (**Figure 14**).

Due to the nature of the AE development and its spectral processing, it became possible for the first time to study the development of the process of cavitation fluid flow around the borehole directly in the coal massif. According to the results of the studies carried out on the borehole simulator (**Figures 2–4**), the pulse tracing recording is divided into components corresponding to different processes: 1—operation of the pumping unit; 2—operating (cavitation) modes; 3—the generator's non-operating range (no hydroimpulsive loosening process); and 4—development of cracks in the massif.

The availability of crack formation recordings and the established ranges of the generator operation allowed us to study the development of the dynamic characteristics of CG-2.5. The discharge process, namely the video recording of the fluid pressure change in the borehole, which was recorded by the manometer, was divided into components in time of 0.25 s. Based on the data obtained on the change in the fluid boost pressure in the borehole, the scope ΔP and the frequency f of the CG-2.5 oscillations were calculated. This made it possible to obtain a nomogram of the process development for the first time in the practice of research on hydroloosening of coal seams (**Figure 15**). An analysis of the development of cavitation fluid flow in the borehole and the hydroloosening process is given in [24].

According to the established hydrodynamic parameters registered by the SPE-98 system, the AFC of the generator was determined. This made it possible to compare the results of theoretical (see **Figure 4**) and mining-experimental studies (**Figure 16**), as well as to evaluate the process of hydroimpulsive loosening of the outburst-hazardous coal in relation to the values of its elastic modulus.

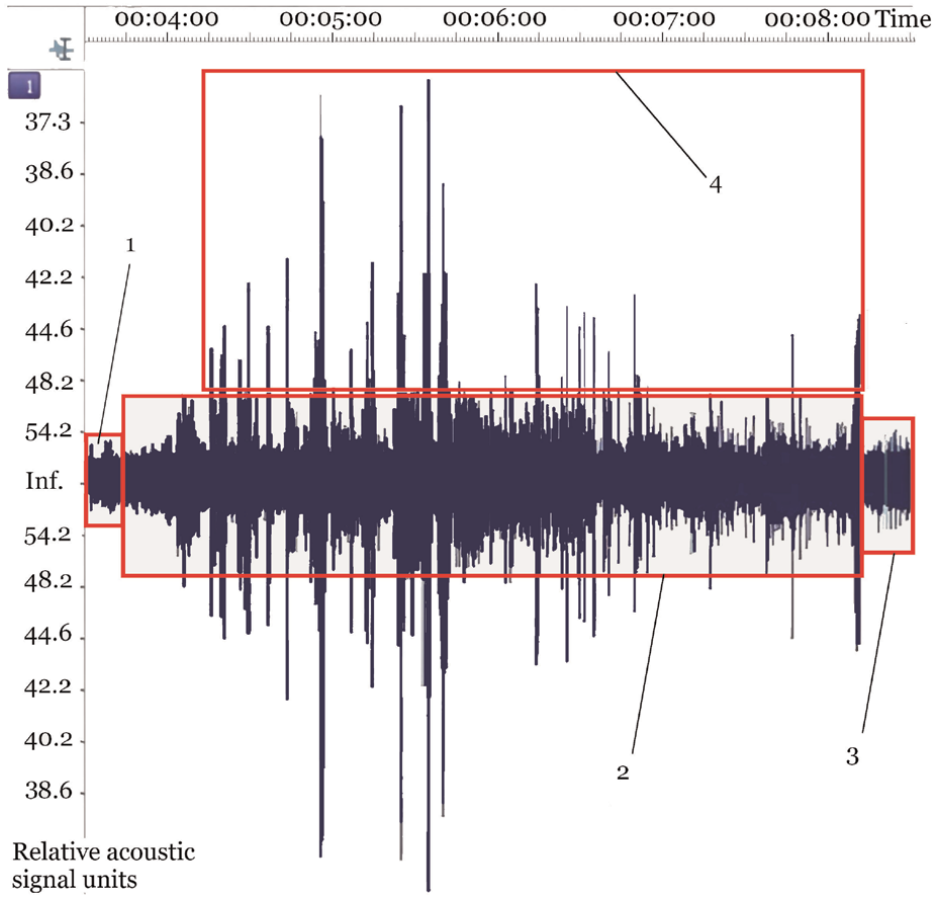

Figure 14.
Development of AE in the coal massif during its hydroimpulsive loosening.

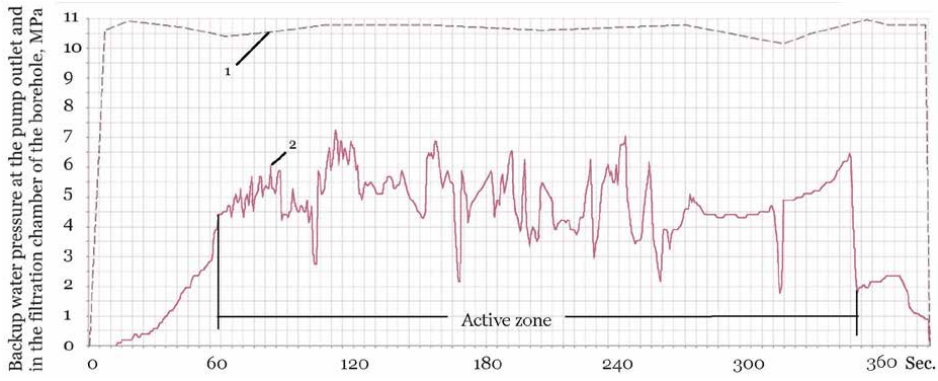

Figure 15.
Nomogram of the process of hydroimpulsive loosening of an outburst-hazardous coal seam.

According to the results of studies of the hydroimpulsive loosening process of the coal seam in the working faces of development workings, it was found that the development of cracks in the massif (destruction of outburst-hazardous coal) begins

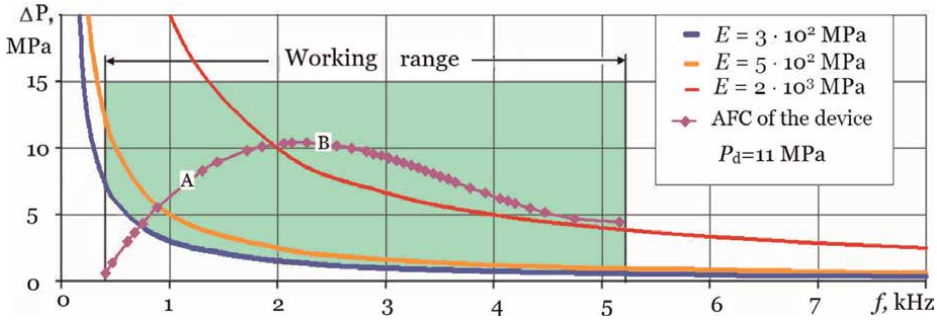

Figure 16.
Comparison of the AFC of the CG-2.5 generator during hydroimpulsive loosening of an outburst-hazardous coal seam with the dependences of strain development $\dot{\varepsilon} \geq 10\ s^{-1}$ at $E = 3 \cdot 10^2$ *MPa;* $5 \cdot 10^2$ *MPa;* $2 \cdot 10^3$ *MPa.*

simultaneously with the development of cavitation fluid flow in the borehole at a fluid boost pressure of ≈0.2 MPa. The active stage of the process occurs at $3.0 \leq P_b \leq 7.0$ MPa and ends at $P_b \approx 1.0$ MPa. In the theoretically established operating zones of the generator, such as zone "A" and zone "B", which correspond to the conditions of coal fracture at the elastic modulus $E = 3 \cdot 10^2$ MPa; $5 \cdot 10^2$ MPa; $E = 2 \cdot 10^3$ MPa, the development of cracks in the massif occurs without any changes in the parameters of the generator operating range.

Thus, regardless of the value of the elastic modulus of coal under the considered conditions, the mode of hydroimpulsive impact $P_d \approx 11$ MPa in a time of 8–11 minutes ensures the loosening of the outburst-hazardous coal seam.

The final stage of the research is to analyze the results of controlling the unloading zone and assessing the efficiency of the method by AE parameters. After the completion of the hydroimpulsive loosening operations, the analysis of the registered AE recordings obtained during the drilling of an exploration borehole was carried out. It was found that at a distance of up to 6.0 m from the mine face, the AE pulses are practically absent, which indicates the presence of an unloaded zone of the massif at least at the depth of the borehole. At a distance from 6.0 m to 17.0 m, a zone of change in the stress–strain state of the massif, which arose after the hydroimpulsive impact, is observed. In this zone, the state of coal outburst hazard is controlled by drilling control holes during the production. In practice, it has been established that it is safe to conduct the workings at a distance of up to 10.0 meters.

5. Conclusions

Acoustic monitoring of the coal-rock massif state in stress–strain zones using the SASTE-1 and SPE-98 systems made it possible to study the process of hydroimpulsive loosening of outburst-hazardous coal seams and establish new criteria for evaluating the efficiency of the method. The following conclusions were made based on the research results.

1. For the first time in the practice of hydroloosening of outburst-hazardous coal seams, the parameters of acoustic monitoring of the state of an outburst-hazardous

coal massif were used to control the parameters of cavitation fluid flow in the fractured-porous coal environment around the borehole.

2. The use of the SASTE-1 and SPE-98 systems made it possible to develop new criteria for assessing the effectiveness of the method of hydroimpulsive loosening of outburst-hazardous coal seams in the working faces of development workings and confirmed the development of the amplitude-frequency characteristics of CG-2.5 in the borehole. The established regularities of the AFC development as a function of the cavitation parameter or the fluid boost pressure in the borehole allow studying the mode parameters of the cavitation discrete-pulse fluid flow.

3. It has been established that the parameters of the developed generator CG-2.5 correspond to the parameters of mining equipment used for hydroloosening of outburst-hazardous coal seams.

4. Comparison of the average statistical data of the parameters of static and pulse modes of fluid discharge, established by acoustic monitoring, confirmed the increase in the efficiency of hydroloosening using the CG-2.5 generator, namely due to:
   - reduction of the massif stress by at least 25% (K_o) and uniform (without delays) development of deformations in the coal seam roof at a distance of more than 10 meters from the working face of the mine;
   - the presence of recordings accompanying cavitation fluid pressure oscillations in the borehole with high-frequency components of the spectra up to 3000 Hz, which correspond to the generator operating modes, and their absence when the boost pressure of the fluid in the borehole drops, the presence of AE spectra corresponding to the development of cracks in the massif;
   - conformity of the AFC of generator to the values of the impulse load of outburst-hazardous coal, which do not depend on the direction of loading and the elastic modulus of coal;
   - the presence of a zone of change in the stress–strain state of the massif ahead of the working face from 6.0 m to 17.0 m, which is created under the influence of hydroimpulsive impact and controlled by changes in AE when drilling control holes in the working face.
   - increase the safe coal recovery zone from the sealing depth to the borehole drilling depth;
   - the established unloading zone, which is formed ahead of the working face of the workings when it is carried out after hydroimpulsive loosening, at a distance of up to 10.0 meters.

Conflict of interest

The authors declare no conflict of interest.

DOI: http://dx.doi.org/10.5772/intechopen.1006643

Author details

Vasyl Zberovskyi[1*], Ruslan Ahaiev[1], Vasyl Vlasenko[1] and Maryna Kyrychenko[2]

1 M.S. Poliakov Institute of Geotechnical Mechanics of the National Academy of Sciences of Ukraine (IGTM NAS of Ukraine), Dnipro, Ukraine

2 Dnipro University of Technology (DniproTech), Dnipro, Ukraine

*Address all correspondence to: igtmdep16@gmail.com

References

[1] Standard Coal Ministry of Ukraine. SOU 10.1.001740088. Standard Coal Ministry of Ukraine. 2005. 225 p

[2] Rodin A. Justification of parameters of effective moistening of coal massif. In: New Methods of Destruction and Mechanics of Rocks. 1981. pp. 19-22

[3] Rodin A, Vasiliev L, Drozd V, Manko I, Bandurin V. Device for pulse water injection into a coal seam. USSR copyright certificate 1034453. September 9. 1981

[4] Pylypenko V. Cavitation Self-Oscillations. Kyiv: Naukova Dumka Publisher; 1989. 316 p

[5] Pylypenko V, Zadontsev V, Manko I, Dzoz N, Volkov V, Severin V, Kostyuk V. Device for obtaining fine dispersed systems. Author's certificate 1590124. 7 September. 1990. 6 p

[6] Vasiliev L, Demchenko V, Rodin A. Impulse pumping unit. Geotechnical Mechanics. 2001;**29**:3-8

[7] Denzersky V, Zhulai Y, Voroshilov O, Skosar V, inventors. Method of hydropulse cleaning. Patent of Ukraine 105602. 26 May. 2014. 6 p

[8] Manko I, Kozlovsky E, Kozlovsky M, Semkiv O, Aleksashina N, inventors. Drill rig for well drilling. Patent of Ukraine 105937. 10 July. 2014. 4 p

[9] Vasiliev L, Zhulai Y, Zberovskyi V, Moiseenko P, Trokhimets N, inventors. Device for hydro-pulse effect on coal seam. Patent of Ukraine 87038. June 10. 2009. 4 p

[10] Vassiliev L, Zhulai Y, Zberovskyi V, Nikiforov A, Kolchin G, Angelovsky O, Chugunkov I, Niskevich A, inventors. Method for hydro-pulse loosening of coal seams. Patent of Ukraine 73023. 10 September. 2012. 4 p

[11] Zhulai Y, Angelovsky A, Vasiliev D. Theoretical substantiation of dynamic parameters of pulse injection of liquid into coal seam. Nauk Visn NMU. 2012;**3** (129):26-30

[12] Dzenzersky V, Zhulai Y, Angelovsky A. Determination of parameters of pulse impact during hydraulic loosening of ejection-prone coal seams. Mining Equipment and Electromechanics. 2013; **3**:43-48

[13] Angelovskiy A, Zhulay Y, Zberovskyi V, Voroshilov A. Investigation of dynamic characteristics of the generator of elastic vibrations during hydroloosening of coal seam. Collection of Scientific Papers of the NMU of Ukraine. 2012;**38**:35-41

[14] Zberovskyi V, Kostandov Y. Limit state of ejection-prone coal seams at their hydraulic loosening taking into account coal shear resistance. Collection of Scientific Works of NMU of Ukraine. 2011;**2**(36):36-43

[15] Zberovskyi V, Kostandov Y, Lokshina L. Consideration of internal and external friction of coal at calculation of parameters of hydroimpulse impact. Geotechnical Mechanics. 2011;**94**:215-222

[16] Zberovskyi V, Shevchenko V, inventors. Method for controlling the state of a coal seam under hydraulic pulse action. Patent of Ukraine 125179. 25 Apr. 2018

[17] Zberovskyi V, inventor. Method of control and management of hydro-pulse

action on coal seam. Patent of Ukraine 125180. 25 Apr. 2018

[18] Zberovskyi V, Bulat A, Krukovskaya V, Krukovskyi O, inventors. Method for studying the state of a gas-bearing coal seam in a mine face under hydraulic action. Patent of Ukraine 132643. 21 Mar. 2019

[19] Zberovskyi V, Zberovskyi A, inventors. Method for hydrodynamic breaking of massif through a well. Patent of Ukraine 50405. October 15. 2002

[20] Zberovskyi V, inventor. Method for formation of well collector. Patent of Ukraine 81694. 25 Jan. 2008

[21] Zberovskyi V. Estimation of efficiency of hydroimpulse impact on coal seam by methods of acoustic control. Geotechnical Mechanics. 2017; **132**:74-84

[22] Deglin B, Melkonyan A. Sound-catching equipment of new generation - "ZUA-98-06". Gorny Informatsionno-Analyticheskiy Bulletin MGMU. 2008; **10**:260-262

[23] Zberovskyi V, Sofiiskyi K, Stasevych R, Pazynych A, Pinka J, Sidorova M. The results of monitoring of hydroimpulsive disintegration of outburst-prone coal seams using ZUA-98 system. E3S Web of Conferences. 2020;**168**:00068. DOI: 10.1051/e3sconf/202016800068

[24] Zberovskiy V, Pazynich A, Zmiievska K, Vlasenko V. Study results of the hydroimpulsive loosening of coal-seams at the active stage. IOP Conference Series. 2022;**970**(1):012024. DOI: 10.1088/1755-1315/970/1/012024

[25] Zberovskyi V, Ahaiev R, Vlasenko V, Sapehin V, Kyrychenko M. Investigation of Self-Destruction Process of the "Coal-Gas" System under Hydrodynamic Impact. Szkoła Eksploatacji Podziemnej. Kraków, Polska: Kraków, Akademia Górniczo-Hutnicza; 2023

[26] Zberovskyi V, Ahaiev R, Vlasenko V, Prytula D. Hydrodynamic impact as a way of controlling the state of the coal-gas system: Analysis and data processing. IOP Conference Series. 2024;**1348**(1): 012039. DOI: 10.1088/1755-1315/1348/1/012039

Chapter 3

Development of an Advanced System for Identifying Low-Altitude Outdoor Mobile Objects Based on Acoustic Signatures

Yiyang Luo, Oleksandr Soboliak, Vladyslav Lutsenko, Irina Lutsenko, Vadym Yehorov, Serhii Yehorov and Trifanov Vitalii

Abstract

This chapter introduces an acoustic-based detection system for low-altitude moving objects, including unmanned aerial vehicles, helicopters, and ground vehicles. The system analyzes acoustic spectra, revealing discrete harmonics from engine rotations and a continuous spectrum from engine operations, with energy primarily below 2 kHz. Harmonic spacing helps estimate rotor speeds for helicopters, while high engine revolutions per minute enhance the continuous spectrum component. Key challenges addressed include target differentiation, bearing estimation accuracy, environmental noise impact, and the need for meteorological adjustments. Experimental results show that high-pass filters with a 500–700 Hz rejection band improve target detection contrast and reduce noise interference. Future work will focus on advanced noise suppression, meteorological data integration, and multisensor fusion to enhance system performance and scalability.

Keywords: acoustic noise, microphone array, autocorrelation function, drones, helicopters, identification systems, low-altitude outdoor aerial objects, moving target selection filter, sensor integration, signal processing

1. Introduction

The detection and identification of low-altitude aerial objects, including unmanned aerial vehicles (UAVs), helicopters, and VTOL flying cars, are vital for ensuring safety and supporting the expanding low-altitude economy. Traditional detection methods, including optical detection, acoustic detection, radio frequency (RF)-based methods, and radar systems, have proven effective in various applications, but each encounters specific limitations under certain conditions.

Radar systems are renowned for their capability in long-range detection, coordinate determination, and trajectory tracking through radar signal characteristics [1–3]. They are highly effective for detecting and tracking objects at considerable distances. Nevertheless, radar systems face challenges in detecting small UAVs due to their low radar cross-section (RCS) and advanced stealth technologies. The presence of electromagnetic pollution from active radar systems also prompts the use of external electromagnetic sources to enhance radar performance while minimizing environmental impact.

Optical detection methods, including telescopes, optical sights, and rangefinders, are known for their high precision in measuring angular coordinates and identifying objects under favorable conditions [4–6]. These systems excel in clear visibility, offering detailed images and accurate object identification. However, their performance significantly deteriorates under adverse weather conditions such as fog, rain, and snow, as well as during nighttime. The limited field of view and lower precision in distance measurement further constrain the effectiveness of cameras.

RF-based detection methods offer several advantages, including cost-effectiveness due to the use of common frequencies like 2.4 and 5.8 GHz ISM bands, all-weather operation capabilities, real-time monitoring, and nonintrusiveness, making them suitable for extensive surveillance. However, they face challenges such as susceptibility to interference and signal attenuation, limited range for detecting distant or stealthy UAVs, complexity in signal analysis requiring advanced algorithms, potential privacy concerns due to pervasive monitoring, and dependence on specific frequency bands that can affect system effectiveness [7–9].

Acoustic detection methods leverage the sound emitted by objects to determine their spatial coordinates. These methods are particularly effective for low-altitude and low-speed UAVs and helicopters. Acoustic systems operate in a passive mode, relying on the inherent noise of the objects to improve stealth and survival capabilities. Compared to radar, acoustic methods benefit from simpler signal processing due to the lower frequency of sound waves, which also reduces system costs. However, these systems are limited by their shorter detection range and sensitivity to environmental noise and interference [10–15].

Each method's effectiveness varies depending on environmental conditions, target characteristics, and operational requirements. This paper explores the potential of acoustic spectral analysis as a complementary approach to enhance detection capabilities, particularly in adverse weather conditions where optical methods are limited and for noncooperative low-altitude aerial objects, such as small UAVs and helicopters, which challenge radar systems and RF-based methods.

This whole paper is structured into six sections, including Introduction, Theoretical Basis, Equipment Setting, Experimental Study of Spectra and Correlation Functions of Acoustic Signals from UAVs and Helicopters, Critical Discussion, Future Work and Conclusion. We specifically examine the acoustic characteristics of UAVs, including the "Shahed-136" [16], as well as helicopters such as the KA-52 [17], Mi-28 [18], and Mi-8 [19], which are frequently encountered in Ukrainian territory. The noise generated by these UAVs and helicopters is detectable by acoustic systems. This chapter also discusses the acoustic characteristics of ground vehicles and wind gusts, which are common and potential environmental factors affecting systems' detection capability for low-latitude outdoor aerial objects.

2. Theoretical basis

This section offers a detailed overview of the principles of acoustic detection systems. It begins with an explanation of acoustic radiation, detailing the generation of sound waves and their propagation, which is influenced by distance and atmospheric conditions. Next, it covers acoustic signal delay and bearing estimation, emphasizing methods to determine the direction of sound sources and manage associated measurement errors. The impact of variations in sound speed and sensor baseline on bearing accuracy is discussed, alongside the effect of sound source bandwidth on precision. The section concludes with methods for estimating bearings from multiple targets by analyzing time delays, providing a comprehensive framework for understanding and improving acoustic detection systems.

2.1 Acoustic radiation

Acoustic radiation refers to the emission of sound waves generated by mechanical systems, such as UAVs and helicopters. This radiation arises from various sources, including mechanical vibrations, engine noise, and aerodynamic turbulence during operation. Although such acoustic emissions are often considered unwanted and disruptive, they also provide distinctive signatures that are essential for the identification and classification of aerial objects. For instance, the noise produced by propellers and rotor blades is directly related to their rotational speeds, while engine noise is a result of combustion processes and mechanical vibrations. The unique modulation frequencies associated with these components serve as critical identifiers for different types of aerial vehicles.

The acoustic power radiated by these systems can be approximated as:

$$\boldsymbol{P}_{acoustic} = \rho_0 c A^2 S^2, \tag{1}$$

where ρ_0 is the air density, c is the speed of sound, A is the surface area of vibrating components, and S is the velocity of the surface vibrations.

However, in practical acoustic wave propagation, several factors contribute to the diminishing intensity of sound waves as they travel through the atmosphere:

1. *Distance attenuation*: following the inverse-square law, sound intensity decreases proportionally to the square of the distance from the source. This can be expressed as:

$$\boldsymbol{P}_{acoustic}(r) = \frac{P_{source}}{4\pi r^2}, \tag{2}$$

where $P_{acoustic}(r)$ is the acoustic power at a distance r, and P_{source} is the initial acoustic power.

1. *Atmospheric absorption*: higher frequencies are more susceptible to absorption by the air, leading to greater attenuation. The attenuation is described by:

$$SPL = SPL_0 - \boldsymbol{\alpha}(f) \cdot r, \tag{3}$$

where SPL_0 is the initial sound pressure level, $\alpha(f)$ is the frequency-dependent attenuation coefficient, and r is the distance. It should be noted that the quantities in Eq. (3) are expressed in decibels, while those in Eq. (2) are given in absolute terms: pressure in pascals and pressure density in Pa/m^2 as a function of r.

1. *Environmental interference*: external noise sources, such as gusty winds and rainfall, can interfere with the detection of acoustic signatures. High-pass filters can mitigate low-frequency interference from these sources, enhancing detection clarity.

2. *Other meteorological factors*: additional weather-related elements, such as temperature gradients, humidity, and wind direction, can further influence sound wave propagation and detection accuracy. Temperature gradients and humidity affect the speed and absorption of sound, while wind direction can cause refraction of sound waves, altering their trajectory and making detection more challenging.

From Eq. (2), it is evident that sound wave attenuation in the atmosphere is frequency-dependent. However, the frequencies associated with aerial objects generally exhibit a stable structural pattern. These frequencies, which correlate with operational speed and the number of blades or rotors, can be detected in both acoustic and radar signals, facilitating a dual-modal identification approach. Previous research [21, 22] has shown that the modulation frequencies of rotating components, such as propellers and engines, are crucial for identifying aerial objects. For example, helicopter rotor blades produce harmonics at multiples of their rotational frequency, serving as distinctive identifiers despite attenuation. Similarly, aircraft with turbofan engines exhibit modulations related to the rotation of shafts and turbines, further defining their acoustic profiles.

Furthermore, to improve detection accuracy, further integration of advanced signal processing methods such as high-pass filtering and spectrum analysis, alongside the use of microphone arrays, can enhance the reliable identification and tracking of aerial objects under difficult conditions.

2.2 Acoustic signal delay and bearing estimation

Acoustic detection systems utilizing multiple sensors, such as microphone arrays, enhance the determination of the direction of incoming wave fronts, allowing for the identification and localization of aerial objects based on their emitted sounds. **Figure 1** illustrates a schematic diagram of such a system, featuring two microphones, M_0 and M_1, positioned at an angle relative to the x-axis, with sound waves propagating along the y-axis. The time delay τ between signals received by the two microphones is used to estimate the azimuth α of the sound source O relative to the baseline between the sensors. This method is extensively employed in sonar, radar, and wireless communications [1–3].

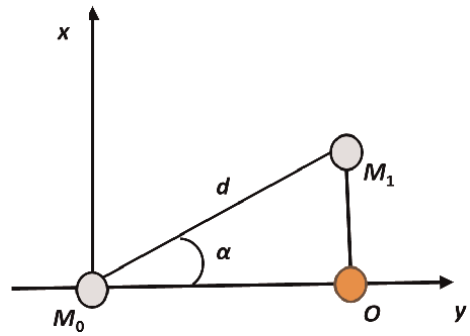

Figure 1.
Schematic diagram of the direction-finding (bearing) system. Schematic diagram of an acoustic direction-finding system consisting of two microphones, M_o and M_1.

The time delay τ of an acoustic signal at microphone M_1 relative to the signal received at microphone M_0 can be mathematically expressed as:

$$\boldsymbol{\tau} = \frac{\boldsymbol{OM}_1}{c} = \frac{d \cdot \sin \boldsymbol{\alpha}}{c}, \tag{4}$$

where d denotes the baseline distance between the microphones, c represents the speed of sound, and α is the bearing angle between the normal to the microphone array's baseline and the direction of the incoming acoustic wave [4].

The relationship between the bearing angle and the time delay can be derived as:

$$\sin \boldsymbol{\alpha} = \frac{c \cdot \boldsymbol{\tau}}{d}. \tag{5}$$

Using this, the bearing angle α is determined by:

$$\boldsymbol{\alpha} = \arcsin\left(\frac{c \cdot \boldsymbol{\tau}}{d}\right). \tag{6}$$

The bearing error $\Delta\alpha$, resulting from an error in the time delay measurement $\Delta\tau$, is a critical factor in direction-finding accuracy and can be estimated using:

$$\Delta\boldsymbol{\alpha} \cdot \cos \boldsymbol{\alpha} = \Delta\boldsymbol{\tau} \cdot \frac{c}{d}, \tag{7}$$

or, more explicitly:

$$\Delta\boldsymbol{\alpha} = \Delta\boldsymbol{\tau} \cdot \frac{1}{t_{\max}} \cdot \frac{1}{\cos \boldsymbol{\alpha}} = \frac{1}{F_0 \cdot t_{\max}} \cdot \frac{1}{\cos \boldsymbol{\alpha}}, \tag{8}$$

where $t_{\max} = d/c$ is the maximum signal delay for the baseline d, and $F_0 = 1/\Delta\tau$ is the sampling frequency of the received signal [5].

As shown in Eq. (8), the bearing error depends on the sampling frequency F_0 and the bearing angle α. The minimum bearing error $\Delta\alpha_{\min}$ occurs when the target is aligned with the normal to the baseline ($\alpha = 0$), where $\cos \alpha = 1$, leading to:

$$\Delta\boldsymbol{\alpha} = \Delta\boldsymbol{\alpha}_{\min} \cdot \frac{1}{\cos \boldsymbol{\alpha}}, \tag{9}$$

where $\Delta\boldsymbol{\alpha}_{\min} = \frac{1}{F_0 \cdot t_{\max}}$.

Previous research [6, 7, 21, 22] has shown that the minimum achievable bearing error increases significantly with the angle from the baseline normal. Specifically, the bearing error grows proportionally to $1/\cos\alpha$ as the angle α deviates from the baseline normal. For instance, a 60° deviation doubles the error. Consequently, sectors within ±60° of the baseline normal (a total angular range of 120°) are generally considered to have acceptable bearing accuracy for direction-finding systems [6, 7]. This underscores the importance of careful system design to ensure accuracy across various operational scenarios, which will be discussed further below.

2.3 Key factors influencing bearing accuracy in acoustic detection systems

Accurate azimuth estimation is crucial in fields such as navigation, communication, and surveillance. The time delay measurement $\Delta\tau$, which is crucial for

determining the azimuth accuracy of an acoustic detection system, is influenced by several factors. Variations in the speed of sound caused by atmospheric conditions—such as temperature, pressure, and humidity—affect measurement precision. The baseline distance between microphones is also crucial; any inaccuracies here directly impact the azimuth estimate. Additionally, the accuracy of time delay measurement (related to the sampling frequency E_0), signal processing techniques (including filtering and spectral analysis), and the bandwidth of the sound source play significant roles. Environmental interference, such as wind and background noise, can further reduce accuracy. The configuration of the microphone array also affects the system's ability to determine the direction of incoming sound waves effectively. This subsection focuses on the effects of variations in sound speed, errors in baseline distance measurement, and the bandwidth of the sound source, providing a detailed analysis of the dependence of bearing error on the bandwidth of the sound source.

1. *The influence of sound speed variations and baseline*. Based on Eq. (7), the influence of sound speed variations, caused by meteorological conditions (temperature, pressure, and humidity), and baseline inaccuracies on the bearing estimation error can be assessed using the following relation:

$$\frac{\boldsymbol{\delta}(\Delta\boldsymbol{\alpha}_{\min})}{\Delta\boldsymbol{\alpha}_{\min}} = \frac{\boldsymbol{\delta}C}{C} + \frac{\boldsymbol{\delta}d}{d}, \tag{10}$$

where:

- $\frac{\boldsymbol{\delta}(\Delta\boldsymbol{\alpha}_{\min})}{\Delta\boldsymbol{\alpha}_{\min}}$ is the relative error in bearing determination, and
- $\frac{\delta C}{C}$ and $\frac{\delta d}{d}$ are the relative errors in the determination of sound speed and the baseline distance, respectively.

If the total bearing determination error must not exceed $\pm 0.5\%$, then as indicated by Eq. (10), the errors in sound speed and baseline distance determination should each be within $\pm 0.25\%$. Since sound speed is significantly affected by temperature changes, achieving the required bearing accuracy necessitates incorporating a weather station in the direction-finding system. This weather station should measure environmental parameters such as temperature (with an error margin up to 1°C), humidity ($\pm 10\%$), and pressure (± 20 Pa).

The minimal achievable bearing measurement errors for various baseline distances (0.5, 0.75, and 1 m) under standard propagation conditions (temperature of 15°C, pressure of 10^{13} hPa, and sound speed approximately 341 m/s) are illustrated in **Figure 2**. To maintain a specified bearing measurement error of 1.5° within a 120° sector, a sampling frequency (F_0) of approximately 28 kHz is required for a baseline of 0.5 m, 18 kHz for a baseline of 0.75 m, and 14 kHz for a baseline of 1 m. Consequently, for baseline distances greater than 0.75 m, selecting an F_0 of 20 kHz ensures the desired hardware accuracy in bearing measurement.

1. *The influence of the sound source bandwidth*. Bearing estimation for a broadband acoustic signal source can be performed by calculating the maximum of the cross-correlation function of the signals received by microphones spaced apart by a baseline. The time delay, which determines the bearing, can be derived from this cross-correlation maximum. The signals received by the microphones can be

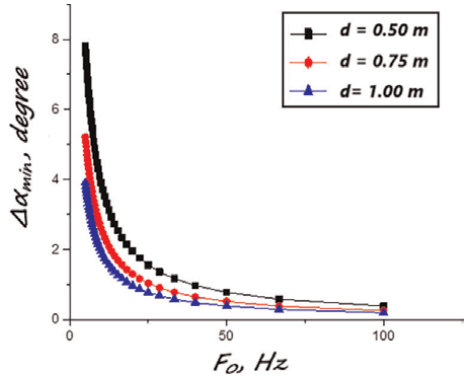

Figure 2.
Dependence of minimum bearing measurement error on baseline and sampling frequency under normal propagation conditions.

denoted as $S(t)$ and $S(t-\tau)$, where τ is the time delay between signals. This time delay can be determined by finding the maximum of the cross-correlation function $R(\tau)$:

$$R_{\max}(\boldsymbol{\tau}) = \max_{\boldsymbol{\tau}\in(0,\boldsymbol{\tau}_{\max})} \int_{t-T}^{t} S(t)S(t-\boldsymbol{\tau})dt. \tag{11}$$

The discrete version of Eq. (11) is given by:

$$R_{\max}(\boldsymbol{j}) = \max_{j\in(0,\boldsymbol{j}_{\max})} \sum_{i-i_0}^{i} S(i)S(i-\boldsymbol{j}), \tag{12}$$

where $j = \tau \cdot F_0$.

Thus, to estimate the time delay of the signals received by a pair of microphones spaced by a baseline distance, the cross-correlation function of the received signals must be calculated for all possible delays, from the minimum to the maximum.

The error in time delay estimation will depend on the required signal-to-noise ratio (SNR) μ_0 for achieving the desired probabilities of correct detection and false alarm, as well as the noise variance $\sigma_N{}^2$ during measurements:

$$R_{\max}(\boldsymbol{\tau}) - R_{\max}(\boldsymbol{\tau}+\Delta\boldsymbol{\tau}) \geq \boldsymbol{\mu}\boldsymbol{\sigma}_N^2. \tag{13}$$

Considering that:

$$R(\boldsymbol{\tau}) = \boldsymbol{\sigma}_S^2\boldsymbol{\rho}(\boldsymbol{\tau}), \tag{14}$$

where $\rho(\tau)$ is the normalized cross-correlation function and $\sigma_S{}^2$ is the variance of the received acoustic signal.

From Eqs. (13) and (14), we obtain:

$$\boldsymbol{\rho}_{\max}(\boldsymbol{\tau}) - \boldsymbol{\rho}_{\max}(\boldsymbol{\tau}+\Delta\boldsymbol{\tau}) \geq \frac{\boldsymbol{\mu}_0}{\boldsymbol{\mu}}. \tag{15}$$

Assuming the normalized correlation function can be approximated by an exponential function:

$$\rho(\tau) \approx \exp(-|\tau/\tau_0|). \tag{16}$$

which corresponds to the spectrum $S(\omega)$ described by the Lorentzian line:

$$S(\omega) \approx \frac{1}{1 + (\omega\tau_0)^2}. \tag{17}$$

It is evident that the bandwidth at half-power $\Delta\omega$ is:

$$\Delta\omega = \frac{1}{\tau_0}. \tag{18}$$

Using the asymptotic representation of the correlation function near its maximum:

$$\rho(\tau \approx 0 + \Delta\tau) \approx 1 - \frac{\Delta\tau}{\tau_0}. \tag{19}$$

Eq. (15) can be rewritten as:

$$\frac{\Delta\tau}{\tau_0} \geq \frac{\mu_0}{\mu}. \tag{20}$$

If the excess SNR during measurements relative to the required SNR for detection with specified quality is denoted as $\Delta\mu = \mu/\mu_0$, then the error in time delay determination is given by:

$$\Delta\tau \geq \frac{\tau_0}{\Delta\mu}. \tag{21}$$

This implies that the error is directly proportional to the correlation interval τ_0 of the received acoustic signal and inversely proportional to the signal bandwidth $1/\Delta\omega$, and inversely proportional to the SNR $\Delta\mu$ above the required level for achieving the desired detection characteristics.

As indicated by Eq. (21), when the SNR is below the required detection level ($\Delta\mu$ = 0 dB), the error in estimating the arrival time of acoustic signals at spatially separated elements will be equivalent to their correlation interval. Conversely, when the SNR exceeds the required level by $\Delta\mu$ = 10 dB, the error decreases by a factor of 10. These relationships can be applied to estimate the upper bounds of errors for various acoustic signal spectra. Combining Eq. (21) with Eq. (8) enables the estimation of bearing error based on the broadband characteristics of the signal and the measured SNR. Assuming that the errors—both instrumental and those related to the broadband nature of the acoustic signal—are independent, the resulting bearing estimation error should remain within the specified limits.

2.4 Bearing estimation using time delays from multiple acoustic sources

Let us consider a scenario where the microphones receive signals from two distinct sources, each with different bearings and therefore different time delays. The signals

from the first source are denoted as $S_1(t)$ and $S_1(t-\tau_1)$, where τ_1 represents the time delay between the signals received by the first and second microphones, determined by the bearing of the first target. Similarly, the signals from the second source are denoted as $S_2(t)$ and $S_2(t-\tau_2)$, where τ_2 is the time delay corresponding to the bearing of the second target. The time delay is measured relative to the first microphone. The received signals at the microphone inputs can be expressed as:

$$\begin{cases} S_{1\Sigma}(t) = S_1(t) + S_2(t) \\ S_{2\Sigma}(t) = S_1(t-\boldsymbol{\tau}_1) + S_2(t-\boldsymbol{\tau}_2) \end{cases}. \tag{22}$$

The cross-correlation function of these signals, assuming the signals from the two sources are statistically independent, is given by:

$$R_\Sigma(\boldsymbol{\tau}) = \boldsymbol{\sigma}^2_{\Sigma S}\boldsymbol{\rho}_\Sigma(\boldsymbol{\tau}) = \boldsymbol{\sigma}^2_{1S}\boldsymbol{\rho}_1(\boldsymbol{\tau}-\boldsymbol{\tau}_1) + \boldsymbol{\sigma}^2_{2S}\boldsymbol{\rho}_2(\boldsymbol{\tau}-\boldsymbol{\tau}_2), \tag{23}$$

where σ_{iS} and $\rho_i(\tau-\tau_i)$ represent the variance and normalized cross-correlation function of the i-th acoustic signal source and its time delay, respectively. The terms $\sigma_{\Sigma S}$ and $\rho_\Sigma(\tau)$ denote the variance and normalized cross-correlation function of the resultant signal.

The resultant cross-correlation function is a weighted average of the cross-correlation functions of the individual signals, with weights determined by their variances. For simplicity, let us assume that time delays are estimated by locating the maxima of the resultant cross-correlation function, as outlined in Eq. (23). This procedure mirrors that used for a single source, as previously described in Eqs. (11) and (12). Consequently, the cross-correlation function for the superposition of signals from two sources will be a weighted average of their individual cross-correlation functions, with weights based on their variances.

To detect the second local maximum corresponding to the second source, its level must exceed the cross-correlation function value of the first source, considering the necessary SNR ratio μ0 for detection. Therefore, we can express this requirement as:

$$\boldsymbol{\sigma}^2_{2S} \geq \boldsymbol{\mu}_0\boldsymbol{\sigma}^2_{1S}\boldsymbol{\rho}_1(\boldsymbol{\tau}_2-\boldsymbol{\tau}_1). \tag{24}$$

From Eq. (24), it follows that as the time separation between received signals decreases, the required signal level for accurate bearing estimation increases. When estimating bearings for complex targets with multiple sources, the process involves computing the cross-correlation function of signals received by a pair of spatially separated microphones. The global maximum of this function indicates the time delay (bearing) of the most intense source. Following this, the second local maximum, corresponding to the second radiation source, can be identified.

3. Equipment setting

When air and ground objects move, their propulsion systems generate noise with distinct characteristics that can be used for type identification. To identify the type of aerial target, we utilize characteristic modulation frequencies caused by the movement of helicopter main rotors and tail rotors, or by the propellers of UAVs. The identification process involves analyzing useful signals and their spectral profiles. The

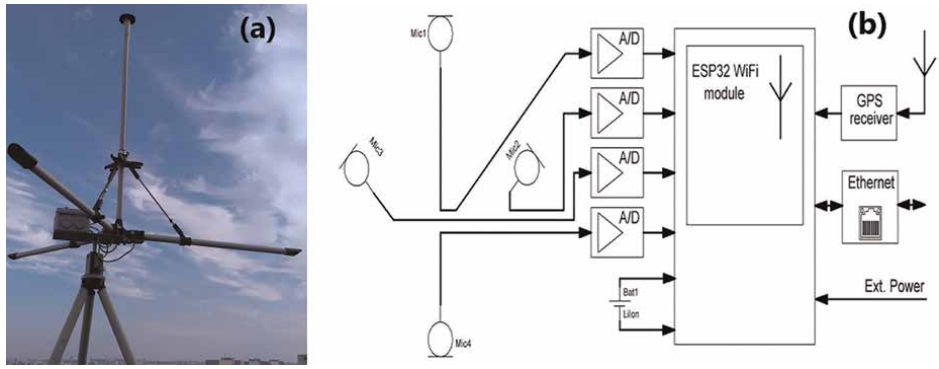

Figure 3.
Photograph (a) and design structure schema (b) of the direction-finding system experimental setting.

characteristic modulation frequencies of the emitted acoustic signals can be used to determine the type of aircraft.

To detect acoustic signatures of UAVs, helicopters, ground targets, and environmental noise, a four-channel measurement system was developed, as shown in **Figure 3**. This system, featuring high precision, uses MEMS microphones for detailed acoustic signal capture. It is integrated with an ESP-32 microcontroller (240 MHz dual-core) and supports Wi-Fi and Bluetooth, with data stored on a 32 GB micro-SD card. The microphone array consists of four omnidirectional INMP441 digital MEMS microphones arranged in a three-sided equilateral pyramid with a 1.4-meter base and 0.8-meter edges. The system's specifications are detailed in **Table 1**.

Although the microphone array was successfully constructed as shown in **Figure 3a**, field testing for UAV trajectory tracking was hindered by the ongoing war. Consequently, the analysis and findings presented in this study are based on previously recorded data from a single microphone, focusing on the spectral characteristics of acoustic signals from each target.

It is important to note that accurate matching of signals received by each channel to their respective sound sources is essential, as it directly influences the precision of subsequent bearing estimations. The sources and cumulative effects of bearing errors were discussed in the previous chapter. To enhance detection accuracy, high-pass filtering was employed to eliminate low-frequency noise, such as wind interference. Advanced signal processing techniques, including spectrum analysis and correlation, were utilized to effectively extract modulated signals. By integrating these methods, the detection system improves reliability in identifying and tracking aerial objects under challenging conditions. Detailed results will be presented in the next chapter.

4. Experimental study of spectra and correlation functions of acoustic signals from UAVs and helicopters

A sampling frequency of 24 kHz and a 24-bit resolution allow for an estimation of azimuth errors within ±1.5° and elevation errors within ±30° [22]. In this study, we analyze four scenarios with a focus on noncooperative helicopters and UAVs that pose potential threats in urban safety environments. These scenarios highlight the practical

Component	Details
Microphones	INMP441 Digital MEMS
Type	Omnidirectional, bottom port
Interface	Digital I^2S, 24-bit data
SNR	61 dBA
Equivalent Input Noise	33 dBA SPL
Sensitivity	−26 dBFS
Frequency Response	60 Hz to 15 kHz
Maximum Acoustic Input Peak	120 dB SPL
Noise Floor	−87 dBFS
Data Digitization	24-bit, 24 kHz sampling frequency
Microcontroller	ESP-32, Dual-core, 240 MHz
Communication Modules	WiFi and Bluetooth
Data Storage	32 GB micro-SD card

Table 1.
Technical specifications of the measuring system.

experimental challenges associated with detecting and identifying low-altitude targets in urban settings. Accurate and timely identification of potential threats in such environments is crucial.

Case 1: Shahed-136. The Shahed-136, an Iranian suicide drone introduced in 2020 [20], is often compared to the Russian Geran-2. This glide bomb has a range of up to 1000 km, with a claimed maximum range of 2000 km. It measures 3.5 meters in length, has a wingspan of 2.5 meters, and weighs 200 kg. Operating at altitudes between 60 and 4000 meters, it maintains a cruising speed of 150 to 170 km/h (40 to 50 m/s). It is powered by a 50 hp. (37 kW) MADO MD 550 engine, a clone of the German Limbach L550E. Its distinct engine noise allows detection from several kilometers away.

Case 2: Ka-52 "Alligator." The Ka-52, a Russian multirole helicopter [17], is an evolved version of the Ka-50 "Black Shark." It measures 16.0 meters in length, with a fuselage length of 14.2 meters, a rotor diameter of 14.5 meters, and a wingspan of 7.3 meters. It is powered by twin TV7-117 V engines, producing 2400 hp. at takeoff, 2700 hp. in emergency mode, and 1750 hp. during cruising. Its maximum speed is 310 km/h, cruising speed is 260 km/h, with a practical range of 460 km, a static ceiling of 4000 meters, and a dynamic ceiling of 5500 meters.

Case 3: Mi-24. The Mi-24, also known as the "Crocodile" [18], is a multirole helicopter developed by the Mil Moscow Helicopter Plant. It has a length of 21.35 meters, a height of 4.73 meters, and a rotor diameter of 17.3 meters. The Mi-24 can achieve speeds of up to 315 km/h at low altitude with a weight exceeding 11,200 kg, or 335 km/h with a weight below 11,200 kg. Its practical range is 450 km, and it has a static ceiling of 1750 meters.

Case 4: Mi-8. The Mi-8, a Soviet multirole helicopter from the early 1960s [19], measures 25.244 meters in length and 4.73 meters in height and has a rotor diameter of 21.288 meters. It can reach speeds of 250 km/h at ground level with a takeoff weight of

11 tons and a cruising speed of 225 km/h at an altitude of 500 meters. Its maximum operational altitude is 4500 meters. At 500 meters altitude, with a normal fuel load of 1450 kg, its range is 365 km, and with a maximum fuel load of 3445 kg, it extends to 1305 km. The main rotor has five blades with a diameter of 21.288 meters, and the tail rotor has three blades with a diameter of 3.908 meters.

By analyzing the fundamental spectral characteristics of the aforementioned four types of low-altitude aerial moving objects, and utilizing advanced signal processing techniques such as autocorrelation functions of acoustic signals, cepstrum analysis, and selective filtering for moving targets, we effectively suppressed and separated background noise.

4.1 Analysis of spectral characteristics

The spectral characteristics of UAVs and helicopters are analyzed in this subsection. **Figure 4** presents the spectra from three passes of the Shahed-136 (Geran-2) UAV. The analysis reveals that the maximum spectral density is concentrated in the frequency range up to approximately 1300 Hz, with several prominent harmonics. Beyond 4 kHz, the spectral density diminishes by more than 30 dB. Notably, all three instances display similar spectral patterns, characterized by a continuous component, which can be approximated by:

$$S_I(F) = S_{01} / \left(1 + \left(\frac{F - F_D}{\Delta F_n}\right)^n\right), \tag{25}$$

and a discrete component $S_D(F)$, representing harmonics associated with the UAV's engine frequencies:

$$S_D(F) = \sum_{i-1}^{n_{\max}} a_i \boldsymbol{\delta}(F - F_D + i\Delta F_n). \tag{26}$$

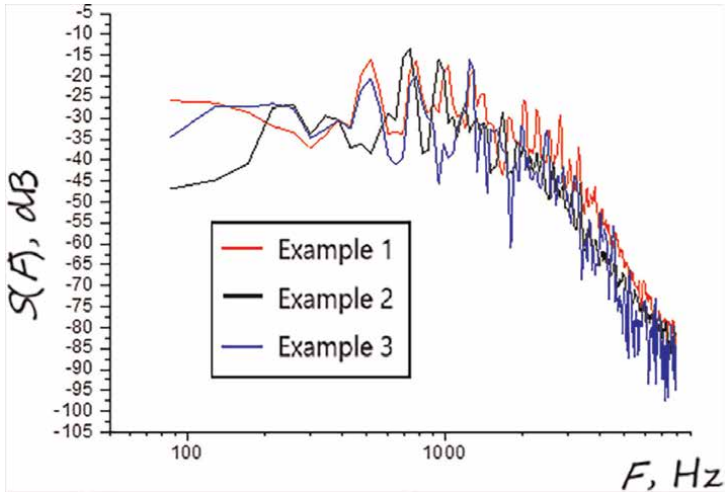

Figure 4.
Spectra of three passes of the Shahed-136 UAV. (Note: The data were sampled at a frequency of 44.1 kHz, with a frequency resolution of 10.767 Hz. The segment length N was 4096 samples, resulting in a duration of ~1.5 seconds. Linear averaging was used, with smoothing applied via a Hanning window. Segment overlap during spectral calculations was 99%).

These components are associated with various mechanisms, including noise-induced aerodynamic and structural processes [23], which are primarily driven by noise generated during the active gas exchange in the engine and cooling systems, as well as vibrations from the engine suspension and its outer surfaces. Studies of the Shahed-136 UAV's acoustic noise reveal that the spectral energy is concentrated within the 200–2000 Hz range. The spectrum comprises both continuous and discrete components, represented by a set of Delta triangular functions. The frequency variation (ΔF_n) is linked to engine revolutions per minute (RPM), while the specific value of Doppler frequency shift (F_D) is influenced by the UAV's flight direction. To estimate the average modulation frequency associated with the UAV's engine operation, the frequency of the maximum spectral value and its corresponding harmonics must be evaluated. For the Shahed-136 UAV, the spectral peak occurs at approximately 1070 Hz, indicating that harmonics related to the modulation frequency are spaced around 107 Hz.

Figure 5 presents the acoustic signal spectra of the Ka-52 and Mi-24 helicopters, respectively, using different frequency resolution elements and time-averaging intervals, displayed on different scales. The spectra for the Ka-52 in **Figure 5(a)** are presented on a logarithmic scale for both frequency (x-axis) and amplitude (y-axis), while for the Mi-24 in **Figure 5(b)**, the frequency is represented on a linear scale and the amplitude on a logarithmic scale. The spectra of the helicopters exhibit a similar pattern to that of UAVs, with differences in the spacing of spectral lines, which are determined by the rotational frequencies of the main and tail rotors. These spectral characteristics can be used to identify the helicopter type. The primary energy is concentrated in the frequency band up to approximately 2000 Hz. Wind noise, concentrated at lower frequencies, can be suppressed using high-frequency (HF) filters to enhance detection against natural background noise.

Furthermore, in contrast to the Shahed-136 UAV and Ka-52 helicopter, whose spectra can be effectively approximated using a linear approximation on a double logarithmic scale for both frequency and amplitude, the Mi-24 helicopter spectrum behaves differently. When represented on a linear frequency scale and a logarithmic amplitude scale, the Mi-24's spectrum can be approximated by a linear function across a wide dynamic range of 40 to 50 dB (**Figure 5b**). This suggests that the HF spectral density for helicopters can be modeled using an exponential function:

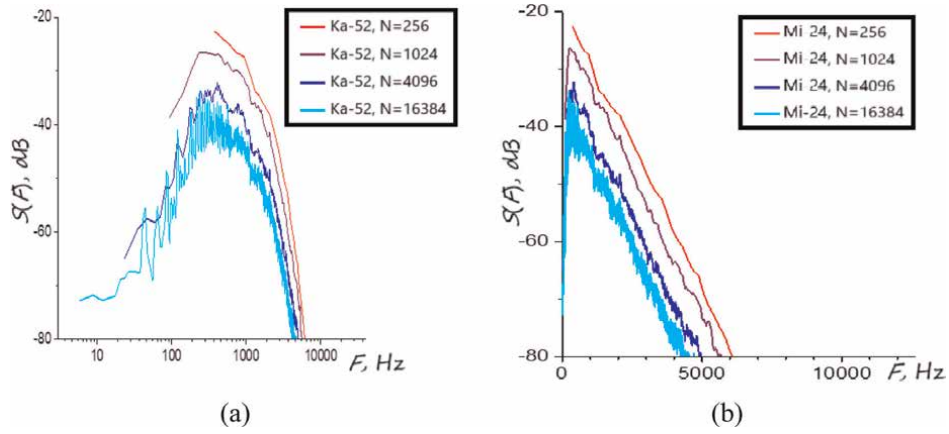

Figure 5.
Spectra of acoustic signals from helicopters Ka-52 (a) and Mi-24 (b).

$$S(F) \approx S_0 \exp\left(-\frac{F}{\Delta F}\right). \tag{27}$$

4.2 Autocorrelation functions of acoustic signals

The autocorrelation function (ACF) of acoustic signals plays a crucial role in analyzing the periodic characteristics of emitted sound waves from aerial vehicles. Unlike amplitude, which can be affected by environmental noise and other external factors, the ACF provides a more stable measure of a signal's inherent periodic features. For an acoustic signal $s(t)$, the ACF $R(\tau)$ is defined as:

$$R(\boldsymbol{\tau}) = \int_{-\infty}^{\infty} s(t)s(t+\boldsymbol{\tau})dt. \tag{28}$$

where τ represents the time lag. The ACF quantifies the similarity between the signal and a time-shifted version of itself, capturing the periodic components of the signal.

Figure 6 displays the ACF of the Shahed-136 UAV's acoustic signals across different time windows. A one-unit shift represents an approximate time offset of 22.7 μs. For larger time windows, as shown in **Figure 6(a)** and **(b)**, the envelope correlation interval is about 13.6 ms, measured at a value of 0.37 from the peak, corresponding to ∼600 units. This interval indicates the effective bandwidth of the acoustic signal, estimated to be between 70 and 80 Hz. For intermediate and smaller time windows, depicted in **Figure 6(c)** and **(d)**, the central frequency shift, inferred from the ACF

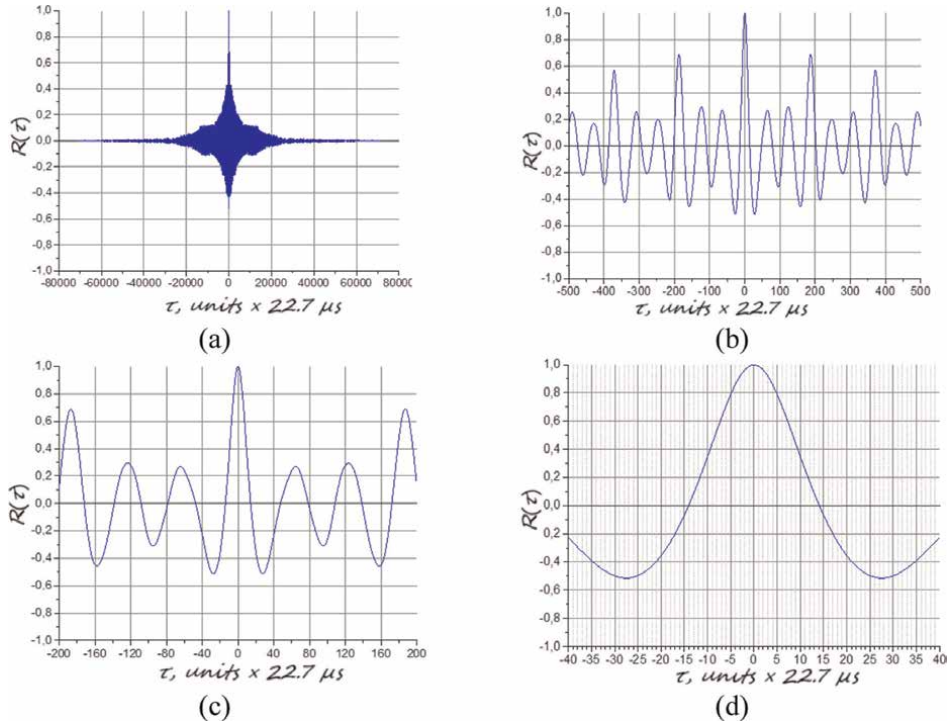

Figure 6.
Autocorrelation function of the acoustic signal of the Shahed-136 UAV.

period, is around 630 to 670 Hz, corresponding to about 65 to 70 units. The ACF of the main lobe can be approximated by an aperiodic function:

$$R(\boldsymbol{\tau}) \approx \exp\left(-\left|\frac{\boldsymbol{\tau}}{\Delta\boldsymbol{\tau}}\right|\right). \tag{29}$$

where $\Delta\tau$ represents the correlation interval for the Shahed-136 UAV. The width of the main lobe of the ACF is ~10 units, corresponding to 227 μs.

The periodic nature of the ACF offers a stable indication of modulation frequencies and rotor blade rotations. Unlike amplitude, which fluctuates due to environmental noise, the ACF consistently reveals these periodic features, enhancing accuracy and reliability in vehicle recognition and classification. Thus, focusing on ACF periodicity improves differentiation between various helicopters and UAVs, refining acoustic signal analysis and detection. For instance, the ACF of the Shahed-136 UAV's acoustic signals indicates that modulation frequencies are more informative than the intensity of scattered signals for identifying aerial vehicles.

Previous studies [21–23] demonstrate that helicopter rotor frequencies are distinctly identifiable through the periodic components in the ACF, which are less apparent from amplitude measurements. The modulation frequency (f_m) of the emitted acoustic signal, associated with blade rotation, can be estimated using the method outlined in Refs. [9, 15]:

$$f_m = \frac{3}{4\pi} \cdot \frac{c}{D} \cdot (N \cdot P) = \frac{1}{\boldsymbol{\tau_m}}, \tag{30}$$

where c, D, N, and P present the speed of sound, the diameter of the rotor blade, the number of blades, and the number of rotors, respectively. And τ_m is the period of the modulation observed in the autocorrelation function. For the Shahed-136 UAV, with an envelope correlation interval of ~13.6 ms, f_m is estimated to be ~73.5 Hz.

Unlike the Shahed-136 UAV, which operates at higher frequencies, the main rotor frequencies of helicopters like the Ka-52 are in the tens of Hz range, with tail rotor frequencies approximately 5 to 6 times higher. The Ka-52's dual main rotors have slightly higher frequencies compared to single-rotor helicopters such as the Mi-8 and Mi-24. **Table 2** presents detailed rotor characteristics and estimated modulation

Characteristic		**Ka-52**	**Mi-24**	**Mi-8**
Main Rotor	Diameter (D, m)	14.5	17.3	21.288
	Number of Blades (N)	3	5	5
	Number of Rotors (P)	2	1	1
	Frequency (f_m,,Hz)	33.7	23.54	19.1
	Period (τ_m, ms)	26.97	42.48	52.36
Tail Rotor	Diameter (D, m)	—	3.91	3.908
	Number of Blades (N)	—	3	3
	Number of Rotors (P)	—	1	1
	Frequency (f_m,,Hz)	—	62.41/196.33	62.44/196.23
	Period (τ_m, ms)	—	16.023/5.094	16.015/5.096

Table 2.
Acoustic signal modulation frequencies and rotor characteristics of helicopters.

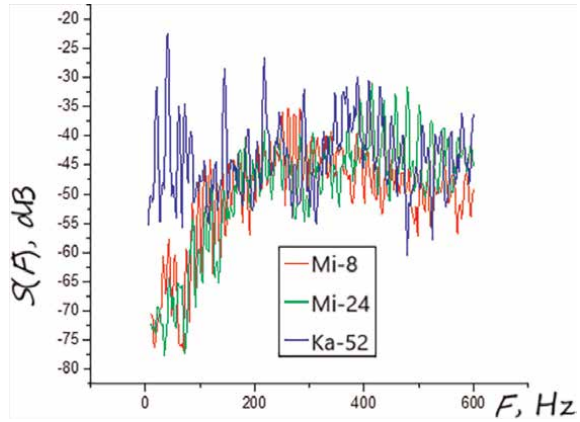

Figure 7.
Low-frequency components of helicopter acoustic spectra: 1 – Mi-8; 2 – Mi-24; 3 – Ka - 52.

frequencies of the emitted acoustic signals, calculated using Eq. (30). **Figure 7** illustrates the low-frequency components of the acoustic spectra from these helicopters. These results are consistent with each other and align with those in Refs. [21–24], indicating that these frequencies are effective for aircraft type identification. However, the estimates in **Table 2** are preliminary and require further refinement.

It is important to note that environmental factors, such as wind gusts, can significantly impact these measurements. Previous studies [23] compared the spectra of wind gusts with those of fixed-wing UAVs and multirotor UAVs. Wind gusts are characterized by energy concentrated at much lower frequencies, and their nonstationary nature can substantially reduce the detection range of objects based on acoustic noise. The following subsection will present measures to mitigate the impact of quasiperiodic natural interference on acoustic system detection.

4.3 Strategies for mitigating environmental noise and enhancing system's detection accuracy

For small aerodynamic objects, such as UAVs, spectral features related to engine speed are prominent. The acoustic noise spectra of four different aerial targets (Shahed-136 UAV, Mi-8, Mi-24, and Ka-52) are illustrated in **Figures 5–8**. UAVs typically exhibit higher rotational frequencies, ranging from 7000 to 11,000 RPM. Previous work [23] has detailed the acoustic characteristics of fixed-wing UAVs, propeller-driven UAVs, and gust noise. The spectrum of fixed-wing UAVs shows a periodicity of about 116 Hz, corresponding to an engine speed of approximately 7000 RPM. Notably, increasing engine speed from idle to maximum results in an 11 to 18 dB rise in noise level, with the frequency of the spectral peak increasing proportionally to the engine RPM, while the overall shape of the emission spectrum remains relatively unchanged [23].

4.3.1 Ground vehicle noise

Noncooperative UAVs often fly over busy highways or rivers to conceal their presence and pose a threat to urban safety. Therefore, it is crucial to consider the differences between the acoustic noise of ground vehicles and UAVs. **Figure 9** depicts the acoustic

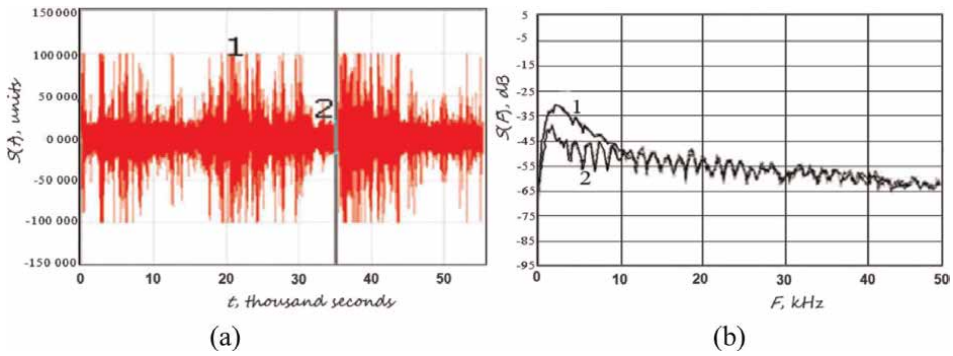

Figure 8.
Time-domain signal (a) and spectra (b) of a quadcopter during a wind gust (1) and in its absence (2).

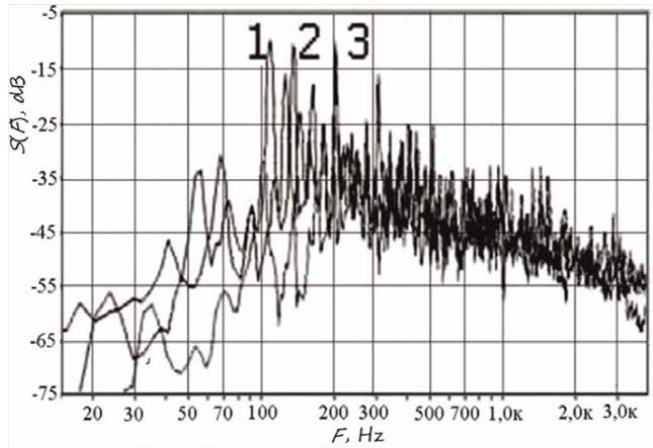

Figure 9.
Acoustic noise spectra of a 3TD diesel engine at various RPMs: 1 – 600, 2 – 1800, and 3 – 2400 RPM.

noise spectra of a ground vehicle equipped with a 3TD diesel engine at various engine speeds (ranging from 600 to 2400 RPM). The spectral behavior of ground vehicles is similar to that of aerial objects, featuring both a continuous spectrum and discrete harmonics related to engine rotation. While the harmonics vary with engine speed, the overall spectral shape remains relatively consistent. This indicates that, despite being part of the environmental interference, ground vehicle noise can still be identified and distinguished from UAV noise based on its unique acoustic characteristics.

4.3.2 Gust wind noise

Gust wind noise presents significant challenges for UAV detection due to its spectral energy being concentrated at much lower frequencies compared to UAV noise. This discrepancy complicates the performance of acoustic detection systems. Additionally, the nonstationary nature of gusts further impedes UAV detection using acoustic signals. To mitigate the challenges posed by natural disturbances such as wind, a modified Fourier transform can be employed to analyze the dynamics of quasiperiodic sequences [23]. Furthermore, broadband interference caused by wind requires specialized noise suppression techniques. For instance, **Figure 8** shows the

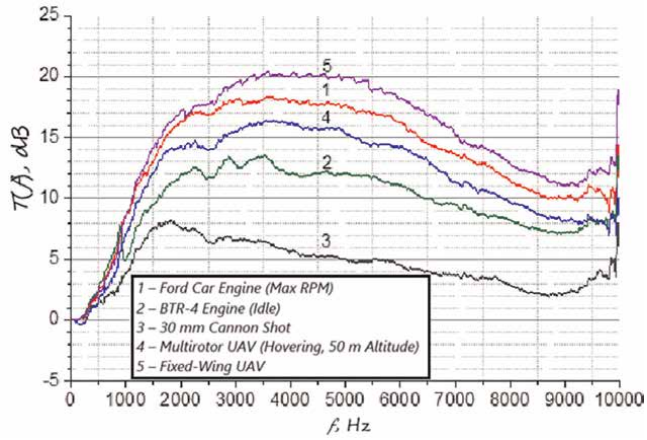

Figure 10.
Dependence of transfer coefficients on cutoff frequency for various objects under wind noise conditions.

recorded noise of a quadcopter at an altitude of approximately 10 meters and its corresponding spectrum. During the experiment, wind speeds ranged from 7 to 8 m/s. Under gusty conditions (moment 1 in **Figure 8(a)**), the noise intensity increased by about 10 dB, and the spectrum broadened at lower frequencies (curve 1 in **Figure 8 (b)**) compared to calmer periods (moment 2 in **Figure 10a**, with the spectrum shown as curve 2 in **Figure 8(b)**). The quadcopter's noise exhibits stationary characteristics, with a spectral periodicity determined by the rotor rotation frequency, approximately 110 Hz, corresponding to ~7000 RPM.

4.3.3 Moving target selection (MTS) filter

Furthermore, considering noise from wind, rain, and engine, self-noise can complicate the detection of other technical objects (targets of reconnaissance), the distribution of noise source power by frequency and the attenuation coefficient α of noise sources when rejecting their low-frequency components were studied:

$$\boldsymbol{\alpha}(f)[\mathrm{dB}] = 10 \cdot \log_{10}\left(\frac{P_{\mathrm{in}}}{P_{\mathrm{out}}(f)}\right), \tag{31}$$

where $P_{\mathrm{in}} = \int_0^{f_{\max}} S(\boldsymbol{\omega})d\boldsymbol{\omega}$ and $P_{\mathrm{out}}(f) = \int_f^{f_{\max}} S(\boldsymbol{\omega})d\boldsymbol{\omega}$ are the power level of the input signal (before filtering) and the output signal (after filtering), respectively.

Figure 11(a) shows the transmission coefficients $T(f)$ [dB] = $-\alpha(f)$ [dB] of the Shahed-136 UAV signal through the MTS filter as a function of the lower cutoff frequency (f). The samples 1, 2, and 3 correspond to those presented in **Figure 4**. With f = 500 Hz, the attenuation of the useful signal remains minimal (<3 dB) while wind noise is significantly suppressed by the MTS filter. This demonstrates that applying a HF MTS filter effectively enhances system's target detection ability by reducing passive interference, such as wind, as illustrated in **Figure 11(b)**.

The effectiveness of noise suppression becomes more pronounced at frequencies above 200 Hz. At a rejection frequency of approximately 500 Hz, the signal-to-noise

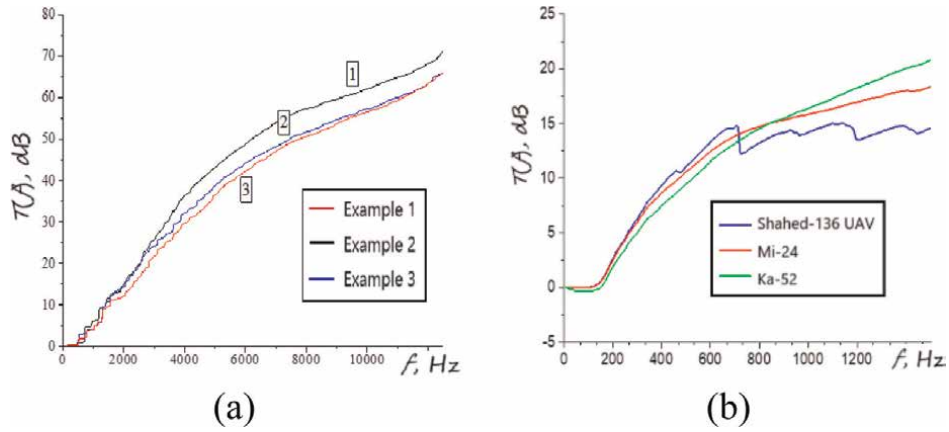

Figure 11.
Dependence of transfer coefficients on cutoff frequency: (a) for acoustic signals from Shahed-136 UAV using MTS filter (1–3 realizations), (b) comparison of contrast enhancement for Ka-52, Mi-24, and Shahed-136 using MTS filter.

ratio improvement at the MTS filter output for UAVs like the Shahed-136, as well as helicopters such as the Ka-52 and Mi-24, is around 10 dB, as shown in **Figure 11(b)**. Expanding the rejection band to 700 Hz further boosts this improvement to 13–14 dB, suggesting that the detection range of these targets amid natural interference can be increased by approximately 2 to 4 times.

The effectiveness of noise suppression becomes more pronounced at cutoff frequencies above 200 Hz. At a rejection frequency of approximately 500 Hz, the signal-to-noise ratio improvement at the MTS filter output for UAVs like the Shahed-136, as well as helicopters such as the Ka-52 and Mi-24, is around 10 dB, as shown in **Figure 11(b)**. Expanding the rejection band to 700 Hz further boosts this improvement to 13–14 dB, suggesting that the detection range of these targets amid natural interference can be increased by approximately 2 to 4 times.

Similarly, MTS filters can be used to improve observation in the presence of wind noise not only for airborne vehicles but also for ground objects, as illustrated in **Figure 10**. In most observed objects, both aerial and terrestrial, HF components are present that can be used for detection and localization. Using data on the attenuation coefficients α_i of noise by a high-pass filter for the i-th observation object, the contrast between objects A and B can be estimated as:

$$\Delta\boldsymbol{\alpha}(f)[\mathrm{dB}] = \boldsymbol{\alpha}_{\mathrm{A}}(f)[\mathrm{dB}] - \boldsymbol{\alpha}_{\mathrm{B}}(f)[\mathrm{dB}]. \tag{32}$$

The resulting contrasts under wind noise conditions are illustrated in **Figure 10**. The analysis reveals that the wind noise spectrum predominantly lies within lower frequency ranges, compared to the noise produced by technical objects. Consequently, by suppressing the low-frequency components, an additional contrast improvement of approximately 10–15 dB can be achieved. This filtering process enhances observability by selectively attenuating low-frequency noise, thereby improving target detection.

4.4 Consideration of meteorological adjustments

Meteorological factors, including temperature, humidity, and variations in wind speed and direction, significantly influence sound propagation and bearing accuracy,

indicating that real-time weather data could enhance system adaptability [1, 11–15, 21–24]. Our recent study [25] investigated the role of these factors in the detection and localization of small, low-speed aerial objects. Quantitative analyses showed that humidity has a minimal effect on sound speed, with variations of less than 0.01% across a relative humidity range of 0–100%. In contrast, sound speed varies by approximately 12% between −30°C and +40°C. Wind speed and direction significantly impact sound speed, with maximum changes occurring when the wind direction aligns with the "source-observer" line, leading to bearing errors when perpendicular. Accurate estimation of wind speed at the object's height should utilize models that account for underlying surface types, as high-rise building models exhibit substantial wind speed variations with height. Therefore, effective acoustic localization must consider these meteorological factors to ensure precise sound radiation and accurate azimuth measurements.

5. Critical discussion

Recent studies have demonstrated that acoustic signatures can effectively identify various types of low-altitude outdoor moving objects [1, 10–16, 21–26]. The developed acoustic detection system shows significant potential for monitoring the trajectories of these aerial objects. However, several critical limitations must be addressed to enhance operational performance.

5.1 Target differentiation

The system accurately identifies UAVs, helicopters, and ground vehicles based on their spectral signatures. However, it encounters difficulties in environments with overlapping noise sources, complicating target differentiation in complex settings.

5.2 Bearing estimation accuracy

Microphone arrays enhance bearing estimation but are less effective in low SNR conditions and with closely spaced targets [13, 14]. Refinements to advanced processing techniques are necessary, while increasing the array base size adds complexity and cost.

5.3 Environmental noise impact

Wind and other nonstationary noises reduce detection performance, particularly at low frequencies. High-pass filters mitigate some effects but may attenuate critical signals. Better noise rejection methods are needed to maintain reliability in varied conditions.

5.4 Meteorological adjustments

Integration with meteorological data is lacking. Temperature, humidity, and wind variations impact sound propagation and bearing accuracy. Incorporating real-time weather data could improve system adaptability.

5.5 Instrumental and measurement errors

Measurement inaccuracies, particularly in angle determination and azimuthal bases, adversely affect bearing precision [13]. Although increasing base size and sampling frequency can mitigate errors, such enhancements complicate the system and elevate costs.

5.6 Passive detection limitations

While passive detection provides stealth, signal attenuation over long distances or in complex terrains remains a challenge. Combining with radar or optical systems may enhance detection capabilities.

5.7 The system's scalability

The system's scalability is limited by its ability to distinguish multiple acoustic sources from noise sources. As noise increases, target differentiation decreases. Further research into adaptive filtering and enhanced algorithms is essential for effective large-scale deployment.

6. Future work

Future efforts will focus on enhancing noise suppression, integrating meteorological data, and applying convolutional neural networks for multi-source wave matching and filtering. Additionally, multisensor fusion will be implemented to improve system robustness and scalability across urban and remote environments.

7. Conclusion

Our study demonstrates the effectiveness and feasibility of using acoustic noise to monitor and identify aerial and ground objects. The acoustic spectra of these targets consist of two primary components: discrete harmonics associated with engine rotation and a continuous component from engine operation and vibration, with substantial energy concentrated below 2 kHz. For helicopters, the spacing of harmonics is critical for estimating rotor speed and type, while increased engine speed enhances the continuous spectrum, facilitating the identification of operating modes. Accurate bearing estimates depend on correlation spacing and SNR, with higher sampling frequencies improving accuracy. Environmental noise, particularly from gusts, can reduce range and introduce errors, complicating detection. Our experiments indicate that a high-pass filter with a rejection band of 500–700 Hz can mitigate some of these effects. Future work should incorporate meteorological data (e.g., temperature, pressure, and humidity) to account for variations in sound propagation and improve error correction. Furthermore, advanced correlation techniques and high SNR are essential for effective detection and tracking of multiple sources.

Acknowledgements

The work by Soboliak O, Lutsenko V, Lutsenko I, Yehorov V, Yehorov S, and Trifanov V was supported by the National Academy of Sciences of Ukraine.

Conflict of interest

The authors declare no conflict of interest.

Thanks

The authors express gratitude to the academic editor, Professor Jiangyi Zhang, for her valuable suggestions, which significantly contributed to the enhancement of the manuscript.

Author details

Yiyang Luo[1,2*], Oleksandr Soboliak[1], Vladyslav Lutsenko[1], Irina Lutsenko[1], Vadym Yehorov[1], Serhii Yehorov[1] and Trifanov Vitalii[1]

1 O. Ya. Usikov Institute for Radiophysics and Electronics of the NAS of Ukraine, Kharkiv, Ukraine

2 V.N. Karazin Kharkiv National University, Kharkiv, Ukraine

*Address all correspondence to: yiyangluo@163.com

References

[1] Oleynikov V, Zubkov O, Kartashov V, Koryttsev I, Sheiko S, Babkin S. Experimental estimation of direction finding algorithms for unmanned aerial vehicles based on their acoustic emission. In: 2019 International Scientific-Practical Conference on Problems of Infocommunications – Science and Technology; 2019; Kiev, Ukraine. Piscataway, NJ: IEEE; pp. 175-178. DOI: 10.1109/PICST47496.2019.9061337

[2] Makarenko SI, Timoshenko AV, Vasilchenko AS. Analysis of means and methods for countering unmanned aerial vehicles. Part 1: The unmanned aerial vehicle as an object of detection and destruction. Systems of Control, Communication and Security. 2020;**1**: 109-146. DOI: 10.24411/2410-9916-2020-10105

[3] Kartashov VM et al. Signal Processing in Radio-Electronic Systems for Remote Monitoring of the Atmosphere. Kharkiv: KhNURE; 2014. 312 p

[4] Kartashov V, Oleynikov V, Zubkov O, Sheiko S. Optical detection of unmanned aerial vehicles in a video stream in real-time. In: The Fourth International Conference on Information and Telecommunication Technologies and Radio Electronics (UkrMiCo'2019); Odessa, Ukraine. Piscataway, NJ: IEEE; 2019. pp. 1-4. DOI: 10.1109/UkrMiCo47782.2019.35 9165362

[5] Kartashov VM, Oleynikov VN, Kolendovskaya MM, Timoshenko LP, Kapusta AI, Rybnichkov NV. Image fusion for detecting unmanned aerial vehicles. Radiotekhnika. 2020;**201**: 120-129. DOI: 10.30837/rt.2020.2.201.10

[6] Sergiyenko O, Rodriguez-Quiñonez JC. Developing and applying optoelectronics in machine vision. Vol. 1. Hershey, PA: IGI Global; 2016. pp. 1-341. DOI: 10.4018/978-1-5225-0632-4

[7] Lutsenko VI, Lutsenko IV, Sobolyak AV, Popov IV, Ahn NX, Luo Y. Interference to active-passive radar systems created by emissions from HF and VHF broadcasting stations. Telecommunications and Radio Engineering. 2020;**79**(10):829-845. DOI: 10.1615/TelecomRadEng.v79.i10.10

[8] Lutsenko V et al. Use of radiation from HF range broadcasting stations for detection of aerial objects. In: 2020 IEEE Ukrainian Microwave Week (UkrMW); Kharkiv, Ukraine. Piscataway, NJ: IEEE; 2020. pp. 267-271. DOI: 10.1109/UkrMW49653.2020.9252652

[9] Lutsenko VI, Popov LIV, DO and Popov IV. Remote Sensing of the Environment Using the Radiation of Existing Ground and Space Radio Systems. Kyiv: Akademperiodyka; 2020. DOI: 10.15407/akademperiodyka.429.345. 345 p

[10] Oleynikov VN, Zubkov OV, Kartashov VM, Koryttsev IV, Babkin SI, Sheiko SA. Investigation of detection and recognition efficiency of small unmanned aerial vehicles on their acoustic radiation. Telecommunications and Radio Engineering. 2019;**78**(9):759-770. DOI: 10.1615/TelecomRadEng.v78.i9.20

[11] Kartashov V, Oleynikov V, Koryttsev I, Sheyko S, Zubkov O, Babkin S, et al. Use of acoustic signature for detection, recognition, and direction finding of small unmanned aerial vehicles. In: 2020 IEEE 15th International Conference on Advanced Trends in Radioelectronics, Telecommunications and Computer Engineering (TCSET); Lviv, Ukraine. Piscataway, NJ: IEEE; 2020. pp.1-4. DOI: 10.1109/TCSET49122.2020.235458

[12] Kartashov VM et al. Information characteristics of sound radiation of small unmanned aerial vehicles. Telecommunications and Radio Engineering. 2018;**77**(10):915-924. DOI: 10.1615/TelecomRadEng.v77.i10.70

[13] Oleynikov VM, Kartashov VM, Sheyko SO, Zubkov OV, Oleynikova OI. Determining the location of small unmanned aerial vehicles based on acoustic emission. Radiotekhnika. 2022; **210**:113-127. DOI: 10.30837/rt.2022.3.210.09

[14] Kartashov VM. Algorithms for direction finding of unmanned aerial vehicles based on their acoustic emission. Radiotekhnika. 2019;**196**:22-31

[15] Shatrov MG, Yakovenko AL, Kricheskaya TY. Noise of Internal Combustion Engines: A Study Guide. Moscow: MADI; 2014. 68 p

[16] Hunder M. Cheap Russian Drone a Menace to Ukrainian Troops and Equipment. London, United Kingdom: Reuters; 2023. Available from: https://www.reuters.com/world/europe/cheap-russian-drone-menace-ukrainian-troops-equipment-2023-06-28/

[17] Ka-52 "Alligator". Available from: https://www.russianhelicopters.aero [Accessed: April 18, 2016], Archived: April 23, 2016

[18] Mikheev VR. Mil Moscow Helicopter Plant: 50 Years. Moscow: Favorite Book Publishing; 1998. Hardcover; 272 pages. ISBN: 5-7656-0013-0

[19] Kazansky Helicopter Plant Produced its 7500th Mi-8/17 Helicopter. Aviation Explorer. 2014. Available from: https://www.aex.ru/news/2014/5/23/120575/

[20] HESA Shahed-136. Available from: https://www.militaryfactory.com/aircraft/detail.php?aircraft_id=2520.

[21] Joshi A, Rahman MM, Hickey J-P. Recent advances in passive acoustic localization methods via aircraft and wake vortex aeroacoustics. Fluids. 2022; **7**(7):218. DOI: 10.3390/fluids7070218

[22] Lutsenko VI, Lutsenko IV, Sobolyak AV. The range of action of acoustic intelligence systems. Appl Radio Electron. 2015;**14**(2):125-136

[23] Lutsenko VI, Lutsenko IV, Sobolyak AV, Luo Y, Guo Q, Zheng Y. The acousto-electromagnetic portrait signatures for the aerodynamic and ground technology objects. Telecommunications and Radio Engineering. 2018;**77**(11):971-993. DOI: 10.1615/TelecomRadEng.v77.i11.40

[24] Trifanov V, Lutsenko V, Sobolyak O, Luo Y, Lutsenko I. Use of temporal and spectral characteristics of acoustic noises of aerial objects for their recognition. In: Proceedings of the III International Scientific and Practical Conference; 2024; Sofia, Bulgaria. NY, USA: International Science Group; 2024. pp. 194-200. DOI: 10.46299/ISG.2024.2.3

[25] Trifanov V, Lutsenko V, Sobolyak O, Luo Y. Influence of meteorological factors on errors in determining the bearing of objects by acoustic noises. In: Proceedings of the I International Scientific and Practical Conference; 2024; Boston, USA. NY, USA: International Science Group; 2024. pp. 177-185. DOI: 10.46299/ISG.2024.2.1

[26] Mięsikowska M. Classification of unmanned aerial vehicles based on acoustic signals obtained in external environmental conditions. Sensors. 2024;**24**(17):5663. DOI: 10.3390/s24175663

Chapter 4

On the Use of Micro-Perforated Panels for Sound Absorption

Rostand B. Tayong

Abstract

This study deals with the sound absorption for micro-perforated panels (MPP) as an effective solution for sound reduction. Single and multiple MPPs backed by an air cavity are presented, analyzed, and both their behavior and response are modeled and measured. The experimental setup relies on the use of an impedance tube. Three MPP samples were fabricated for this study: two MPP samples are made of Aluminum and one sample is polymer-made to analyze the contribution of the panel vibration to the overall sound absorption. To support the analysis, two models are presented: a model based on the acoustic propagation in short and narrow tubes and a model based on the equivalent fluid. Both models are compared to the experimental data and discussed. The theory considers no interactions between the holes. It is particularly showed that the sound absorption in the low-frequency ranges can be enhanced by using the combined effects of multiple MPPs and their vibrational effects. Relatively good agreement is also observed between the prediction and the measurement. The study suggests the present technique as a relatively easy and cheap technique for enhancing the sound absorption of systems including MPPs backed by air cavity.

Keywords: micro-perforated panel, absorption coefficient, acoustic, sound reduction, sound testing

1. Introduction

Due to the development of economic activities, noise pollution has increased to such an extent that it is now one of the leading causes of individual complaints in many countries around world. The transport industries already use lots of conventional porous absorbent materials for medium and high frequencies; low frequencies remain difficult to address because they require the use of large material thicknesses that are often incompatible with industrial constraints. The current trend is therefore to use thin and light structures. For the past decades, micro-perforated panels (MPPs) has been considered as an emerging and effective method to absorb sound. They stand as a clean and interesting alternative to traditional porous materials as described by Cobo and Simon [1]. MPPs consist of sub-millimetric holes in a panel, acting as the Helmholtz resonator principle [2]. Major advantages that MPPs offer is that their sound absorption performance can be optimized by adjusting parameters such as the panel thickness, the holes diameter (or perforation size) and the open area ratio (also

known as the porosity) [3]. These sound absorption systems offer practical benefits such as minimal space requirements and cost-effectiveness [4]. In addition, multiple layers of MPPs arrangement can significantly broaden their absorption frequency range [1]. All these potentials of MPPs suggest that they can be versatile and interesting sound absorbers in various applications, particularly in building and transport domains. Other non-negligible reasons for their preference are that they offer interesting advantages such as wind proofing, waterproofing or flameproofing compared to the traditional porous materials such as glass wool [5]. They are therefore suggested as an alternative sound solution to the traditional materials mostly in extreme or harsh environments that require high temperature or high velocity gas circulation.

The acoustic response of MPP is influenced by various factors such as the sound pressure level, the vibrational behavior of the panel, the distribution of the holes across the panel surface and the geometrical characteristics of the MPP. To predict the acoustic response of MPPs when subjected to an acoustic excitation, models need to take into consideration these factors. The principle of using MPPs as sound absorption solutions is simple but their modeling remains incomplete. Their principle is as followed: when the incident acoustic wave encounters the MPP, it propagates through the perforations. If the dimensions of the perforations are of the order of magnitude of the thermal and viscous boundary layers, part of the acoustic energy is dissipated by friction and heat exchange, or by vortex detachment in the case of high sound pressure levels. There are various approaches to modeling MPP at low sound pressure levels. These approaches include the theoretical and empirical approaches to acoustic orifices developed by Bolt et al. [6], the Helmholtz resonator approach [7], the acoustic propagation in short and narrow tubes approach expanded by Maa [8], the equivalent fluid approach developed by Atalla and Sgard [9] and various numerical approaches, including the semi-analytical methods [10]. Recently, many research works have explored various aspects of MPP performance. The work by Yang et al. [11] developed a theoretical model for oblique sound incidence on finite MPP absorbers, demonstrating that absorption coefficients depend on incident angle, frequency, and cavity modes. There is also an empirical optimized model using the response surface methodology developed by Esraa et al. [12]. This model predicts the sound absorption coefficients of MPP in a convenient approach for practitioners. Tayong et al. [13] investigated MPP behavior at high sound excitation levels, presenting a model based on Forchheimer's flow regime and conducting experiments using an impedance tube with a pressure driver. They particularly observed that maximum absorption can be a positive or negative function of perforation flow velocity, suggesting the existence of an optimal flow velocity for maximum absorption. To model MPPs in complex environments, a patch transfer function approach has been proposed, allowing for the assembly of different vibro-acoustic subsystems and facilitating physical interpretation [14]. By using a Bayesian design approach, Xiang et al. [15] studied the possibility of optimizing the performance of multilayered MPP absorbers for a broad range of frequencies. Their work research suggests this approach as effective for designing absorbers that can effectively attenuate sound across various frequencies. The work by Li et al. [16] attempted to provide a comprehensive understanding of how flexible perforated panel absorbers function in absorbing sound waves. Through numerical simulations, they elucidated the specific processes involved in sound absorption by such panels. Their results can potentially inform the design, enhancement and optimization of sound absorption systems that include MPPs when applied to various environments. While the work by Chen et al. [17] focuses on the benefits of metasurfaces in different applications, they specifically

address absorptive metasurface inaccuracies made of micropore and microslit panels in multiple structures. They clearly showed the importance of understanding and mitigating inaccuracies in the metasurface designs to optimize their performance. MPPs were also studied under controlled active conditions. The work by Ma et al. [18] for example used a point force controlled thin plate to depict an error sensing strategy low-frequency sound absorption of MPPs. Relatively good results were obtained for their model and experimental data built around a piezoelectric patch attached to the absorber. Multi-section perforation sizes were investigated to evaluate their contribution to the sound absorption of MPPs [19]. This study revealed that varying perforation sizes can influence their sound absorption capabilities. They showed that the relationship between the air cavity depth and the sound absorption needed better understanding. The effect of inhomogeneous MPPs with multiple cavities, known as multi-chamber MPPs, was studied by Deepak et al. [20]. By testing micro-helix metamaterial structures fabricated through 3D printing, they revealed some potentials for enhancing their sound absorption performance. Furthermore, the sustainability aspect of the MPP was used in the study by Beheshti et al. [21] by testing MPP based on sugarcane fibers and bagasse. They demonstrated a 76% achievement for the peak of sound absorption coefficient for double-leaf MPPs. The use of sugarcane fiber composite in the air gap was showed to cause a shift of the sound absorption peak to frequencies below 100 Hz. MPP sandwich structure based on selective laser melting was studied by Li et al. [22] as an alternative technique to increase the sound absorption coefficient. These structures resonate when excited by sound waves. Still in an attempt to enhance the sound absorption coefficient of MPPs backed by a porous material composite, SheikhMozafari et al. [23] developed a numerical study using Finite Element Methods (FEM). It is particularly shown that halving the porous layer's thickness and replacing the half by an air layer and single MPP is an effective method to enhance the sound absorption rather than using thick porous materials. Optimization of MPPs is also depicted in the work by Hashemi et al. [24] to generate wider absorption bandwidths than non-optimized MPPs. Their work showed relatively good agreement between FEM and Equivalent Circuit Model (ECM) results predictions.

To enhance the sound absorption of an MPP, one common and relatively cheap technique consists of using multiple MPPs separated by air cavity or porous materials. While single-leaf MPP absorbers are effective in controlling absorption coefficients, they are limited in their sound absorption bandwidth, usually only exhibiting one narrow resonance absorption peak. To address this limitation, double-leaf and multi-leaf MPP absorbers have been proposed to broaden the absorption frequency range. In a study by Xiaoling et al. [25], the sound absorption properties of MPP with partitioned cavities were investigated using impedance tube experiments [25]. The results showed that double-leaf MPP with partitioned cavities exhibited two main sound absorption peaks at different frequencies, leading to a broader sound absorption bandwidth compared to single-leaf MPP absorbers [25]. The maximum sound absorption peak of MPP with partitioned cavities was also greater than that of single-leaf MPP absorbers [25]. These findings suggest that the use of partitioned cavities in MPP absorbers can improve their sound absorption performance [25]. Tayong et al. [26] proposed a technique to reduce ambiguity in the inversion of microperforated panels' parameters by linking the hole diameter to the open area ratio [26]. This technique could potentially enhance the design and optimization of MPP absorbers with partitioned cavities to further improve their sound absorption properties [26]. Overall, the simultaneous inversion of microperforated panels' parameters, particularly in the context of single and double air-cavity backed systems, presents a

promising avenue for enhancing the sound absorption performance of MPP absorbers, especially when incorporating partitioned cavities [25, 26]. Further research in this area could lead to the development of more effective sound absorbers for reducing noise levels in various applications. Carbajo et al. [27] conducted a study on perforated panel absorbers with micro-perforated partitions. In their study, they found that multi-size perforated panel absorbers with micro-perforated partitions showed a wider sound absorption effective bandwidth compared to those using rigid partitions [27]. Min and Cong [28] compared the acoustic absorption performance of MPPs using the Transfer matrix method and Equivalent electric circuit approach (EECA), introducing the effectiveness of both techniques. The study of sound absorption performance of layered micro-perforated and poro-elastic materials has been a topic of interest in recent years. Kim and Mendoza [29] conducted a study using a micro-perforated panel and a porous layer to investigate and optimize the acoustic performance of such layered systems. The study formulated the micro-perforated panel with the porous layer based on Biot theory to understand the effect of porous materials in a multi-layer system. In the study by Gao and Hou [30], an experimental investigation of sound absorption in a composite absorber was also conducted, further contributing to the understanding of the sound absorption behavior in composite materials systems. Their research builds upon previous studies on sound absorption, such as the work by Yang et al. [31] on subwavelength total acoustic absorption with degenerate resonators, which demonstrated near-perfect absorption with airborne wavelengths larger than traditional composite absorbers. The combination of a sonic black hole with multi-layer MPPs has been proposed as a structure to achieve low-frequency and broadband sound absorption simultaneously [32] which is shown to remain a challenge. The work by Zou et al. [33] focused on analyzing the differences between the use of impedance transfer and equivalent circuit methods for estimating the sound absorption of double layer micro-perforated membranes backed by air cavities and a rigid wall. Their work particularly provided a note on the prediction method of the reverberation absorption coefficient of double layer micro-perforated membrane. They demonstrated that in certain circumstances both methods can have significant differences. Their experiment showed better result agreement with the impedance transfer method than with the equivalent circuit. However, they concluded that the distance between the two MPPs plays an important role for accurate calculations using the equivalent circuit method.

Despite the extensive works already done on multiple layers of absorbers including MPPs, there still exists some knowledge gaps between the suitable approach to predict their behavior and the consideration of other effects that could contribute to enhance their performance. The present chapter attempts to fill some of these gaps by studying the case of up to three MPPs layers backed by an air cavity and accounting for the vibrational effect of the MPPs. The aim is to show how this combination of effects can be predicted but also can contribute to enhance the sound absorption coefficient. It is particularly showed that the sound absorption in the low-frequency ranges can be enhanced by using the combined effects of multiple MPPs and their vibrational effects. In addition, the models presented are easy to implement to predict the acoustic response of these systems. The present chapter is organized as followed: After presenting the geometrical parameters of MPPs and their acoustics characteristics, the next section will deal with the sound absorption calculation for single and multiple MPPs backed by an air cavity and a rigid wall. This section will be followed by the experimental setup, presenting the MPP samples tested for the present work and the equipment used to measure the sound absorption coefficient. Results obtained are

analyzed and discussed in the next section. The important findings for this study are summarized in the conclusion.

1.1 Geometrical parameters of an MPP

An MPP is a panel consisting of a distribution of through-thickness perforations (holes) that have sub-millimeter perforations. **Figure 1a** shows MPP important parameters where d represents the hole diameter, b is the center-to-center hole distance, ϕ is the open area ratio also known as the porosity and h is the panel thickness. The open area ratio ϕ is defined as the ratio of the total volume of the perforations and the total volume of the panel and generally calculated as

$$\phi = \frac{nV_p}{V_T}, \tag{1}$$

where V_p is the volume of a perforation and V_T is the total volume of the panel. There are two common lattice arrangements of perforations over the surface of the panel: The square lattice arrangement [34] for which

$$\phi = 0.785\left(\frac{d}{b}\right)^2 \tag{2}$$

and the triangular lattice arrangement [35] which equation is

$$\phi = 0.906\left(\frac{d}{b}\right)^2. \tag{3}$$

1.2 Acoustic characteristics of an MPP

MPPs are normally designed to produce sufficient acoustic resistance and low acoustic mass (reactance) [5]. By principle, their acoustic impedance is complex

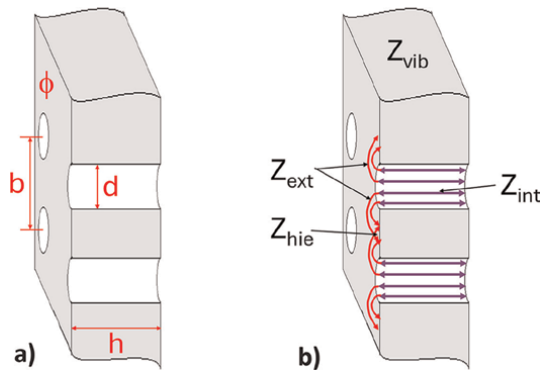

Figure 1.
Description of the MPP. (a) Important geometrical parameters with the open area ratio, d is the diameter, b is the center-to-center hole distance and h is the panel thickness; (b) acoustic impedances describing the acoustic response of an MPP with Z_{int} accounting for the visco-thermal dissipation inside the perforation, Z_{ext} accounts for the external effect related to the distortion of flow at the inlet (also the outlet) of the perforation, Z_{vib} accounts for the vibrational (or structural) effect of the panel and Z_{hie} accounts for the holes interaction effect at the inlet (also the outlet) caused by adjacent perforations.

(having a real part known as resistance and an imaginary part named as reactance) and must match the surrounding medium (generally air) impedance. Now, because the impedance or the surrounding medium is real (no imaginary part), the reactance of the MPP acoustic impedance must be compensated by another component's reactance such as air cavity or porous material. This explains why MPP must be backed by an air cavity or a porous material to be effective in terms of sound absorption. **Figure 1b** presents the different acoustic impedances that characterize the acoustic response of an MPP. These impedances are listed as followed:

- Z_{int} accounts for the visco-thermal dissipation inside the perforation.
- Z_{ext} accounts for the external effect related to the distortion of flow at the inlet (also the outlet) of the perforation.
- Z_{vib} accounts for the vibrational (or structural) effect of the panel.
- Z_{hie} accounts for the holes' interaction effect at the inlet (also the outlet) caused by adjacent perforations.

The present study aims at presenting the effectiveness of using Multiple layers of MPPs to enhance their sound absorption frequency range. Both models and measured are compared and analyzed in different configurations. This work assumes no holes interaction effect for the MPP studied. This chapter is structured as followed: the next section presents two common models used to predict the sound absorption of systems incorporating MPPs. Next the experimental setup is described followed by the results and discussion section. The important findings for this work are summarized in the conclusion.

2. The sound absorption calculation

For an MPP system backed by an air cavity and a rigid wall, calculation of the sound absorption coefficient depends on surface impedance given by

$$Z_s = Z_{MPP} + Z_{cav}, \tag{4}$$

where the impedance of the air cavity is given by

$$Z_{cav} = -jZ_0 \cot(k_0 D_{cav}), \tag{5}$$

with D_{cav} the depth of the air cavity and k_0 the wave number. Assuming a plane wave propagation at normal incidence to the MPP, the reflection coefficient of the system is calculated by

$$R = \frac{Z_s - Z_0}{Z_s + Z_0}, \tag{6}$$

from which the absorption coefficient is deducted and calculated as

$$\alpha = 1 - |R|^2. \tag{7}$$

The characteristic impedance of the air cavity backed MPP can be calculated from any of the following described models.

2.1 Acoustic propagation in short and narrow tubes model

This approach, developed by Maa [8], is based on the work by Rayleigh [36] on the wave propagation in a cylindrical tube which was solved for short tubes by Crandall [37]. For this approach, the radial velocity of the wave inside the tube is assumed negligible compared to the axial velocity and the tube thickness is smaller than the wavelength. So, the differential equation for the axial velocity is given by

$$j\omega\rho_0 u - \frac{\eta}{r}\frac{\partial}{\partial r}\left[r\frac{\partial}{\partial r}u\right] = \frac{\Delta p}{h}, \tag{8}$$

where Δp represents the pressure difference at the tube inlet and outlet, h the tube length (corresponding to the thickness of the perforated panel), η the dynamic viscosity, ρ_0 the air density, r is the radial coordinate and u is the particle velocity in the tube. The characteristic impedance Z_{int} of the tube (the perforation) is obtained by developing u into an integer sequence and by identifying the coefficients which gives

$$Z_{int} = \frac{32\eta h}{d^2}\sqrt{1+\frac{k_p^2}{32}} + j\omega\rho_0 h\left[1+\frac{1}{\sqrt{3^2+k_p^2/2}}\right], \tag{9}$$

for which ω is the angular frequency and $k_p = d\sqrt{\frac{\omega\rho_0}{4\eta}}$ is the perforation constant defined as the ratio of the perforation diameter and the viscous boundary layer thickness inside the perforation. The external effect Z_{ext} related to the distortion of flow at the inlet (also the outlet) of the perforation is taken into account by considering the sound radiation Z_{rad} at the inlet (and outlet) of the perforation and twice a resistance correction R_c suggested by Rayleigh [36] due to the vibrations of the air particles on the flange of the perforation. By taking into account these effects for both the inlet and outlet, the external effect impedance Z_{ext} is given by

$$Z_{ext} = 2Z_{rad} + 4R_c, \tag{10}$$

where

$$Z_{rad} = \frac{(k_0 d)^2}{2} + j\frac{8k_0 d}{3\pi}, \tag{11}$$

with k_0 the wave number and

$$R_S = \frac{1}{2}\sqrt{2\omega\rho_0\eta}. \tag{12}$$

These later results are valid for a single perforation. Under careful considerations, an homogenization can be performed on all the panel perforations. Assuming that the minimum distance b between the perforations is greater than the hole diameter (and smaller than the wavelength considered), it is possible to consider that the effects of

interaction between perforations are negligible. In this case, the total impedance of the MPP is given by

$$Z_{MPP} = \frac{Z_{\text{int}} + Z_{ext}}{\phi}. \tag{13}$$

2.2 Equivalent fluid model

The work by Atalla and Sgard [9] has shown that MPP can be modeled using an equivalent fluid approach initially developed by Johnson-Allard [38] for porous media. In their model, the effective density $\tilde{\rho}_e$ of the MPP can be expressed as

$$\tilde{\rho}_e = \rho_0 \tilde{\alpha}_\infty, \tag{14}$$

for which $\tilde{\alpha}_\infty$ is the dynamic tortuosity given as

$$\tilde{\alpha}_\infty = \alpha_\infty \left(1 + \frac{\sigma\phi}{j\omega\rho_0\alpha_\infty} G_J(\omega)\right), \tag{15}$$

with

$$G_J(\omega) = \left(1 + j\frac{4\omega\rho_0\alpha_\infty^2\eta}{\sigma^2\phi^2\Lambda^2}\right)^{1/2}, \tag{16}$$

and σ is the MPP resistivity ($\sigma = 8\eta/\phi r^2$) normally obtained from the static viscous permeability expression for the Poiseuille law, α_∞ is the geometrical tortuosity, η is the dynamic viscosity of air, Λ is the viscous characteristic length which is equal to the hydraulic radius of the perforation. It is worth noting that the thermal effects within the perforations are assumed negligible due to their small size and shape. To account for the distortion of the flow at the perforation inlet and outlet, the geometrical tortuosity is corrected according to the medium behind the MPP. For the case of an air cavity and a rigid wall behind the MPP, the geometrical tortuosity is given by

$$\alpha_\infty(\omega) = 1 + \frac{2\varepsilon_e}{h}, \tag{17}$$

where ε_e = 0.48 $\sqrt{\pi r^2}$ (1–1.14$\sqrt{\phi}$) is the correction length obtained by a modal approach in the case of circular cross-section perforations and for $\sqrt{\phi} < 0.4$. The MPP acoustic impedance is then given by

$$Z_{MPP} = j\frac{\omega}{\phi}\tilde{\rho}_e h. \tag{18}$$

2.3 The vibrational effect of the plate

Effects due to the vibration of the MPP coupled to the air cavity may be involved in the absorption mechanisms. This effect can either enhance or alter the sound absoprtion of the system as described by Lee et al. [39]. This would depend on the material properties of the panel. Vibration effects must therefore be incorporated into the models. The vibration of thin and homogeneous plates with no holes has been the

subject of numerous studies and the most common basic theory of thin plates is given by Kirchhoff-Love [40]. From these works, it can be demonstrated that the acoustic impedance of a non-perforated panel backed by an air cavity can be obtained as

$$Z_{vib} = j\omega M_S A_{mn} + \frac{1}{j\omega}\left[\frac{D_{rig}(1+j\eta_{mn})}{L_x^2}B_{mn} + \frac{\rho_0 c_0^2}{D_{cav}}\right], \tag{19}$$

where M_S is the surface mass of the panel, η_{mn} is the loss factor related to the plate mode, L_x is the lateral dimension of the panel, ρ_0 is the air density, c_0 is the speed of sound in the air, A_{mn} and B_{mn} are the modal coefficients which depend on the boundary conditions of the panel and D_{rig} is the modulus of the flexural rigidity given by

$$D_{rig} = \frac{Eh^3}{12\left(1-\nu_p^2\right)}, \tag{20}$$

where E is the Young modulus and ν_p is the Poisson's ratio. The vibrational impedance of the perforated panel $Z_{MPP-vib}$ is calculated following an electric circuit analogy as

$$\frac{1}{Z_{MPP-vib}} = \frac{1}{Z_{MPP}} + \frac{1}{Z_{vib}}. \tag{21}$$

2.4 Some parametric results

Figure 2 shows the absorption coefficient result for the variation of the hole diameter as a function of frequency. In this configuration, one can easily observe that optimum values for the resonance frequency (frequency at which the absorption coefficient is maximal) are obtained between 600 and 900 Hz and the corresponding optimum diameter values range between 0.1 and 1 mm. Any diameter value below 0.1 mm would result to a poor absorption coefficient. Maximum absorption coefficient of 1 is obtained for values of diameter between 0.3 and 0.45 mm suggesting a relatively narrow bandwidth. In addition to this, it is observed that out of the

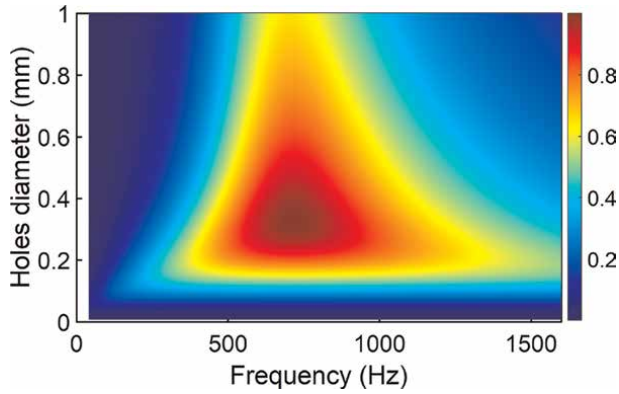

Figure 2.
Variation of MPP hole diameter as a function of frequency. Plate thickness is 2.2 mm, Open area ratio is 1.5% with an air cavity depth of 50 mm.

optimum resonance frequency range, a small changes in value of the diameter would lead to a degradation of the absorption coefficient.

Figure 3 depicts the absorption coefficient result for the variation of the open area ratio as a function of frequency. Unlike the case for diameter variation the range for optimum values for the open area ratio is relatively broad. The optimum values for the resonance frequency are obtained between 450 and about 900 Hz and the corresponding open area ratio values range between 1 and 4.5%. Small changes in values of the open area ratio would not yield to a degradation of the absorption coefficient.

2.5 Modeling the multi-layered MPPs backed by an air cavity

To model the case of multiple MPPs backed by an air cavity and a rigid wall, the Transfer Matrix Method (TMM) is often used. The principle of this method is to determine the pressure fields reflected by or transmitted through a multi-layered MPPs as described by Lauriks et al. [41]. The TMM can be used to calculate the surface impedance of the multi-layered MPPs system. By expressing the conserved physical data at one end of the layer as a function of the physical data at the other end, it is possible to determine the transfer matrix T_{MPP} for the propagation in each MPP as

$$T_{MPP} = \begin{pmatrix} 1 & Z_{MPP} \\ 0 & 1 \end{pmatrix}, \tag{22}$$

and in the case where the layer is airspace either between two MPPs or between the MPP and the rigid wall, the transfer matrix T_A is calculated as

$$T_A = \begin{pmatrix} \cos(k_0 D_{cav}) & jZ_0 \sin(k_0 D_{cav}) \\ j\frac{1}{Z_0} \sin(k_0 D_{cav}) & \cos(k_0 D_{cav}) \end{pmatrix}. \tag{23}$$

Each layer is therefore expressed as a matrix and their direct product is calculated to get the global transfer matrix T of the system which would provide an expression of the surface impedance Z_s of the mulit-layered MPPs as

$$Z_s = \frac{T(1,1)}{T(2,1)}. \tag{24}$$

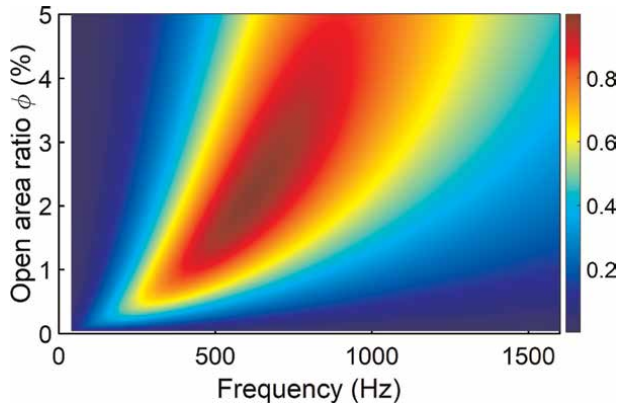

Figure 3.
Variation of MPP open area ratio as a function of frequency. Plate thickness is 2.2 mm, hole diameter is 1.0 mm and air cavity depth of 50 mm.

3. Experimental setup

3.1 Characteristics of the samples

The testing for this study is performed on one polymer and two Aluminum MPP samples as presented in **Figure 4**. The samples have a circular shape, and the circular cross-section perforations have a triangular lattice arrangement over the plate surfaces. The characteristics of the MPP samples are given in **Table 1**.

3.2 Settings for the measurement

Figure 5a shows the impedance tube used for the testing. Description of the internal part of this impedance tube is also presented. This experimental setup is made of a tube with an internal diameter of 100 mm, providing a cut-off frequency of the tube of about 1600 Hz. At one extremity of the tube, a sound source is mounted to generate the acoustic signal. A JBL compression driver, model 2450 J, is chosen for the source excitation with the purpose of generating stable sound pressure levels

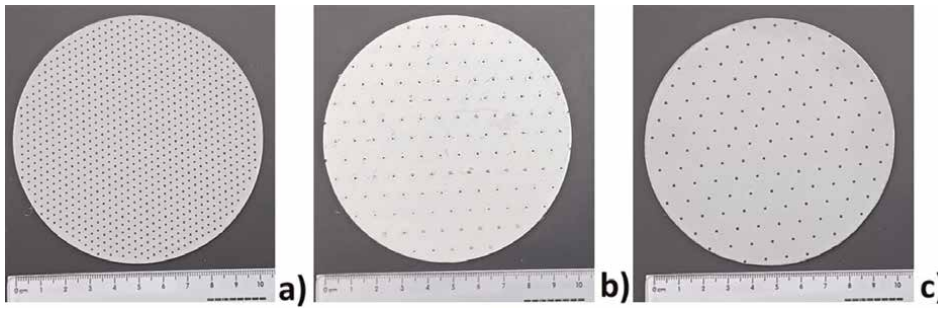

Figure 4.
Circular shape MPP samples with triangular lattice arrangement of the perforations. Diameter of the plate is 100 mm with a thickness of 2.2 mm. (a) MPP1; (b) MPP2; (c) MPP3.

Parameter	MPP1	MPP2	MPP3
Thickness h (mm)	2.2	2.2	2.2
Hole diameter d (mm)	0.7	1.0	1.0
Holes distance b (mm)	2.8	10.6	7.5
Open area ratio (%)	5.7	0.8	1.6
Material	Aluminum	Polymer	Aluminum
Density (kg/m^3)	2700	900	2700
Young Modulus (GPa)	68	4.9	68
Loss factor	0.01	0.11	0.01
Poisson's ratio	0.33	0.30	0.33

Table 1.
Characteristics of the MPP samples. For a clamped condition of the MPP the modal coefficients are taken as $A_{mn} = 2.02$ and $B_{mn} = 2640$.

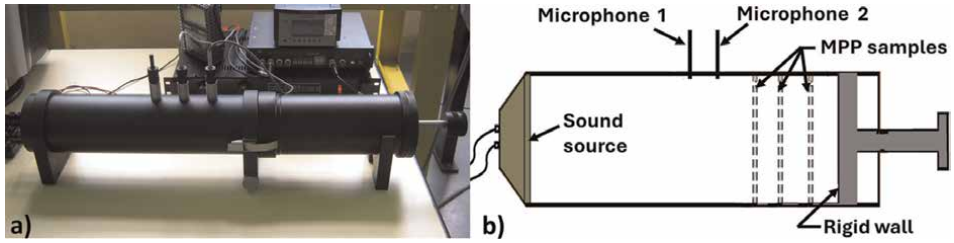

Figure 5.
Impedance tube used for the testing. (a) Photograph of the equipment;)b) Schematic of the impedance tube showing the samples.

necessary for the testing. Since the diameter of this sound source is smaller than the internal diameter of the impedance tube, a transition piece is adapted to the system to ensure a smooth continuity transition. At the other extremity of the impedance tube, a rigid plunger is mounted to create the hard wall behind the MPP samples tested as described in **Figure 5**. The position of the plunger inside the impedance tube can be changed to create variable air cavity depth behind the samples tested. Thin rings with fixed thicknesses are used to create a distance between the MPPs. Two microphones, 1/4″ size, are used to capture the sound pressure signal in front of the MPP and to calculate the surface impedance following the two-microphone standing waves method [42]. Both microphones have a separation distance of 50 mm and the distance between the first microphone (Microphone 1 in **Figure 5b**) and the first MPP sample is about 61 mm. Careful measurement is taken to ensure that the standing wave inside the impedance tube is not saturated and the linear propagation hypothesis is always applicable. With this hypothesis, both the pressures and velocities at any section of the impedance tube can be calculated, as shown by Dalmont [43] as:

$$u = j\frac{p_1}{Z_0}\frac{H\cos(k_0 l_1) - \cos(k_0 l_2)}{\sin(k_0 s)}, \tag{25}$$

where p_1 is the pressure on microphone 1, and l_1 (resp. l_2) is the distance from microphone 1 (resp. 2) to the MPP sample.

4. Results and discussion

Figure 6 represents the comparison results for the absorption coefficient for MPP1. Both models of equivalent fluid and Maa are compared to the real data obtained from the impedance tube. The resonance frequency of 921 Hz is fairly predicted by both model. However, the amplitude of the absorption coefficient for the models less agrees with the real data. The difference between both models is mainly due to the modeled resistance (real part of the characteristic impedance of the MPP). The equivalent fluid impedance seems to minimize the acoustic impedance of MPP1 more than Maa model does.

Figure 7 shows the comparison results for the absorption coefficient for MPP2. Both models of equivalent fluid and the model of Maa are compared to the experimental data. Both the model of Maa with and without accounting for the vibration effect are plotted. The real data depicts two peaks: the first peak corresponding to the frequency of about 370 Hz is related to the viscous effects and the peak around 850 Hz

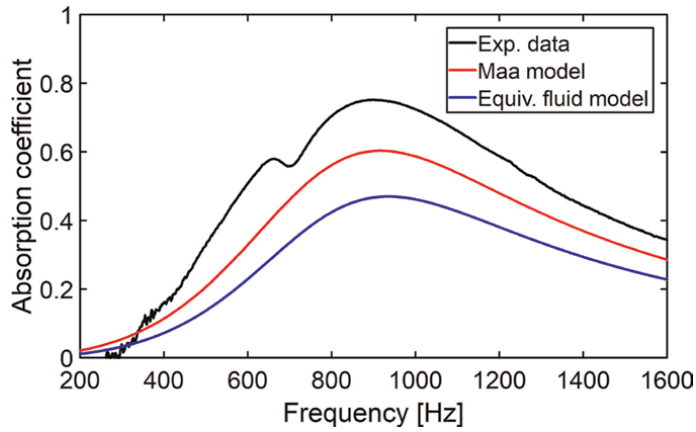

Figure 6.
Comparison results for the absorption coefficient for MPP1. Experimental data (black curve); Maa Model (red curve); Equivalent model (blue curve).

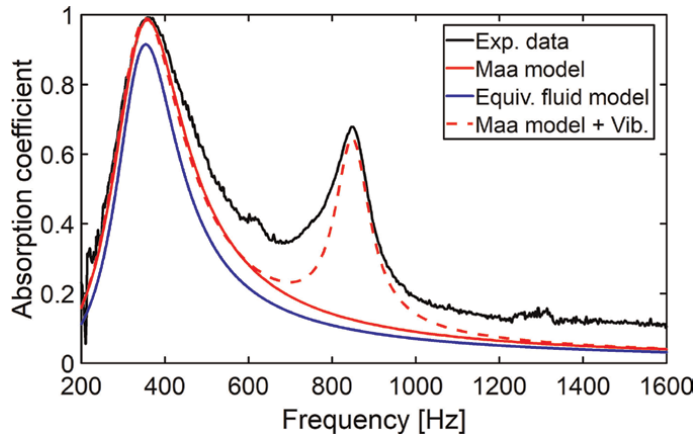

Figure 7.
Comparison results for the absorption coefficient for MPP2. Experimental data (black curve); Maa Model (red curve); Equivalent model (blue curve); Maa Model accounting for the plate vibration (red dashed curve).

is related to the vibrational effect. The model of Maa accounting for the vibrational effect fairly agrees with the real data across the frequency range studied. Although the equivalent fluid model and the model of Maa without vibration effect fairly predict the viscous peak, they fail to calculate the structural response of MPP2. This result particularly shows that the vibrational can improve the soudn absorption coefficient around 850 Hz, globally enhancing the performance of the MPP.

Figure 8 presents the comparison results for the absorption coefficient for MPP3. Both models of equivalent fluid and the model of Maa are compared to the measurement. The vibrational effect is negligible and the absorption coefficient is mainly due to the viscous effects. One can observe that the model of Maa fairly agrees well with the real data. Although the equivalent fluid model fairly predicts the resonance frequency, the agreement with the absorption amplitude is failing. The reason for this fail is as explained for MPP1, due to the modeled resistance of the MPP impedance. The resulst depicts a peak of the absorption coefficient around 500 Hz.

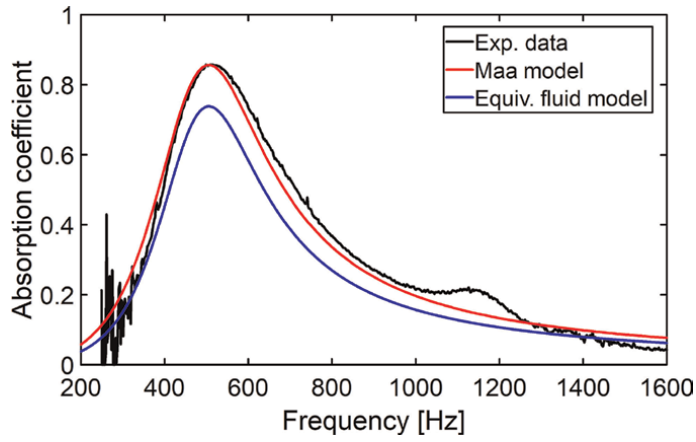

Figure 8.
Comparison results for the absorption coefficient for MPP3. Experimental data (black curve); Maa Model (red curve); Equivalent model (blue curve).

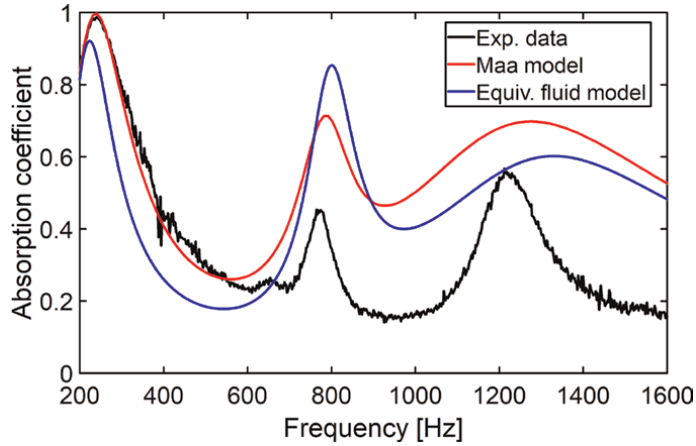

Figure 9.
Comparison results for the absorption coefficient for multi-layer MPPs. MPP1 backed by an air cavity of 30 mm, followed by MPP2 backed by an air cavity of 40 mm and followed by MPP3 backed by 50 mm air cavity before a back wall. Experimental data (black curve); Maa Model (red curve); Equivalent model (blue curve).

For these configurations of a single MPP backed by an air cavity and a rigid wall, the results presented here reveal that this system are a good solution for absorbing the sound in the relatively low to medium frequency range. However, the peak of the absorption coefficient is relatively sharp and the frequency bandwidth covered is limited. This is a characteristic of MPP backed by an air cavity. To improve this performance, one technique is arrange the MPPs in a multi-layered configuration as can be seen in the next result.

Figure 9 depicts the comparison results for the absorption coefficient for multi-layer MPPs. Here the three MPPs are tested in a multi-layered configuration. The arrangement is as followed: MPP1 is backed by an air cavity of 30 mm, followed by MPP2 backed by an air cavity of 40 mm and followed by MPP3 backed by 50 mm air cavity before a back wall. Both models of equivalent fluid and the model of Maa are compared to the measurement. The real data reveals three peaks for the absorption

coefficient. The first peak around 250 Hz is mainly due to the viscous effect created by the MPP close to the acoustic source. The next peak around 800 Hz is due to the combined viscous and vibrational effects of the MPP placed midway between the first and last samples. Finally, the third peak is mainly due to the viscous effect of the MPP close to the rigid wall. Globally, one can observe that unlike for a single MPP, multi-MPPs have an broader frequency range covered. The models fairly predict the resonance frequencies (viscous and vibrational) but struggle to globally capture the amplitude of the peak. This result particularly shows that the sound absorption in the low-frequency ranges can be enhanced by using the combined effects of multiple MPPs and their vibrational effects.

5. Conclusions

The present study dealt with the sound absorption for micro-perforated panels (MPPs) backed by an air cavity and a rigid wall as an effective solution for sound reduction in relative low frequency range. Single and multiple MPPs backed by air cavity are presented, analyzed, and both their behavior and response are modeled and measured. The experimental setup relies on the use of the impedance tube. Three MPP samples were fabricated for this study: two samples are made of Aluminum and one sample is made of polymer to analyze the contribution of the vibration effect of the panel to the overall sound absorption. To support the analysis, two models are presented: a model based on the equivalent fluid and a model based on the acoustic propagation in short and narrow tubes. The followimg concluding remarks can be drawn:

- The use of systems composed of MPPs backed by an air cavity is an effective way to absorb sound at specific frequencies.
- These frequencies are shown to depend on the MPP geometrical parameters and the air cavity depths.
- Two models were presented as effective tools for predicting the sound absorption for these systems.
- Relatively good agreement is observed between the prediction and the measurement.
- Vibrational effects of the panels can enhance the sound absorption coefficient of these systems.
- Multiple layers of MPPs backed by air cavities have an broader sound absorption coefficient.

This study particularly revealed that the sound absorption in the low-frequency ranges can be enhanced by using the combined effects of multiple MPPs and their vibrational effects. Since this work considered no holes interaction effect, the next step would be study how all these effects can help design broader and higher sound absorbing systems composed of multiple layers of MPPs.

Conflict of interest

The author declares no conflict of interest.

Author details

Rostand B. Tayong
Institute for Research in Engineering and Sustainable Environment (IRESE),
University of Bedfordshire, Luton, United Kingdom

*Address all correspondence to: t_rostand2@yahoo.fr

References

[1] Cobo P, Simon F. Multiple-layer microperforated panels as sound absorbers in buildings: A review. Buildings. 2019;**9**(2):53. DOI: 10.3390/buildings9020053

[2] Stremtan F-A, Garai M, Lupea L. Micro-perforated panels and sound absorption. Acta Technica Napocensis Series: Applied Mathematics, Mechanics and Engineering. 2012;**55**(3):549-554

[3] Wong Y, Sekar V, Noum SYE, Sivanesan S. Effect of thickness and perforation size on the acoustic absorption performance of a micro-perforated panel. MATEC Web Conference. 2021;**335**:03016. DOI: 10.1051/matecconf/202133503016

[4] Fuchs H, Zha X. Micro-perforated structures as sound absorbers: A review and outlook. Acta Acustica united with Acustica. 2006;**92**(1):139-146

[5] Maa DY. Theory and design of microperforated panel sound absorbing constructions. Scientia Sinica. 1975; **18**(1):55-71. DOI: 10.1360/ya1975-18-1-55

[6] Bolt RH, Labate S, Ingard U. The acoustic reactance of small circular orifices. Journal of the Acoustical Society of America. 1949;**21**:94-97

[7] Ingard U. On the theory and design of acoustic resonators. Journal of the Acoustical Society of America. 1953;**25**: 1037-1061

[8] Maa DY. Potential of micro-perforated panel absorber. Journal of the Acoustical Society of America. 1998;**104**: 2861-2866

[9] Atalla N, Sgard F. Modeling of perforated plates and screens using rigid frame porous models. Journal of Sound and Vibration. 2007;**303**:195-208

[10] Howe MS. On the theory of unsteady high Reynolds number flow through a circular aperture. Proceedings of the Royal Society of London. Series A. 1979; **366**:205-223

[11] Yang C, Cheng L, Pan J. Absorption of oblique incidence sound by a finite micro-perforated panel absorber. Journal of the Acoustical Society of America. 2013;**133**(1):201-209

[12] Esraa A-A, Putra A, Mosa AI, Dan RM, Attia OH. An empirical model for optimizing the sound absorption of single layer MPP based on response surface methodology. International Journal of Technology. 2022;**13**(3): 496-507

[13] Tayong R, Dupont T, Leclaire P. On the variations of acoustic absorption peak with particle velocity in micro-perforated panels at high level of excitation. Journal of the Acoustical Society of America. 2010;**127**(5): 2875-2882

[14] Maxit L, Yang C, Cheng L, Guyader J. Modeling of micro-perforated panels in a complex vibro-acoustic environment using patch transfer function approach. Journal of the Acoustical Society of America. 2012; **131**(3):2118-2130

[15] Xiang N, Fackler CJ, Hou Y, Schmitt AAJ. Bayesian design of broadband multilayered microperforated panel absorbers. Journal of the Acoustical Society of America. 2022;**151**:3094-3103

[16] Li J, Zhao P, Wang P, Yang C. Revisiting the sound absorption mechanisms of a finite flexible perforated panel absorber using a

numerical approach. Journal of the Acoustical Society of America. 2024; **156**(4):2566-2577

[17] Chen Z, Xiang N. Absorptive metasurface inaccuracies made of micropore and microslit panels in multiple structures. Journal of the Acoustical Society of America. 2024;**155**: A321

[18] Ma X, Yurchenko D, Chen K, Wang L, Liu Y, Yang K. Structural acoustic controlled active micro-perforated panel absorber for improving wide-band low frequency sound absorption. Mechanical Systems and Signal Processing. 2022;**178**:109295

[19] Tan WH, Wahab F, Mat F, Chan CK, Teoh RJ. Sound absorption coefficient measurement and analysis for multisection perforation microperforated panel. Journal of Mechanical Science and Technology. 2024;**38**:2797-2803

[20] Deepak PJ, Nadimpalli R, Chinnapandi LBM. Exploring the acoustic potential of 3D printed micro-perforated panels: A comparative analysis. Helyon. 2024;**10**(7):e28612

[21] Beheshti MH, Khavanin A, Jafarizaveh M, Tabrizi A. A novel acoustic micro-perforated panel (MPP) based on sugarcane fibers and bagasse. Journal of Materials Science: Materials in Engineering. 2024;**19**(35):1-15

[22] Li Z, Zhou Y, Kong X, Zhang P, Pei S, Ge L, et al. Sound absorption performance of a micro-perforated plate sandwich structure based on selective laser melting. Virtual and Physical Prototyping. 2024;**19**(1):e2321607

[23] SheikhMozafari MJ. Enhancing sound absorption in micro-perforated panel and porous material composite in low frequencies: A numerical study using FEM. Sound and Vibration. 2024; **58**:81-100

[24] Hashemi Z, Asadi N, Sadeghian M, Putra A, Ahmadi S, Alidosti M, et al. Optimization and comparative analysis of micro-perforated panel sound absorbers: A study on structures and performance enhancement. Journal of the International Measurement Confederation. 2024;**236**:115123

[25] Gai X-L, Li X-H, Zhang B, Liu Y-Q, Tuo X. Sound absorption properties of microperforated panel with membrane cell and mass blocks composite structure. In: Proceedings of the International Industrial Informatics and Computer Engineering Conference. 2015 January. pp. 345-348

[26] Tayong RB, Manyo Manyo JA, Siryabe E, Ntamack GE. On the simultaneous inversion of micro-perforated panels' parameters: Application to single and double air-cavity backed systems. Journal of the Acoustical Society of America. 2018; **143**(4):2279

[27] Carbajo J, Ramis J, Godinho L, Amado-Mendes P. Perforated panel absorbers with micro-perforated partitions. Applied Acoustics. 2019;**149**: 108-113

[28] Min S, Cong B. Comparison sound absorption methods of multilayer micro-perforated panels. In: Proceeding 5th International Conference on Mechanics and Mechatronics Research (ICMMR 2018); Tokyo Japan. Vol. 417. 2018. p. 012001

[29] Kim J-W, Mendoza JM. Sound absorption performance of layered micro-perforated and Poro-elastic materials. Noise Control Engineering Journal. 2013;**61**(1):100-113

[30] Gao N, Hou H. Experimental investigation of sound absorption in a composite absorber. Theoretical and Applied Mechanics Letters. 2021;**11**(1): 100221

[31] Yang M, Meng C, Fu C, Li Y, Yang Z, Sheng P. Subwavelength total acoustic absorption with degenerate resonators. Applied Physics Letters. 2015;**107**(10): 4930944

[32] Liang X, Liang H, Chu J, Jin F, Wu J. Sound absorber based on a sonic black hole and multi-layer micro-perforated panels. Physica Scripta. 2024;**99**(6): 065960

[33] Zou J, Shen Y, Yang J, Qiu X. A note on the prediction method of reverberation absorption coefficient of double layer micro-perforated membrane. Applied Acoustics. 2006; **67**(2):106-111

[34] Miasa IM, Okuma M, Kishimoto G, Nakahara T. An experimental study of a multi-size microperforated panel absorber. Journal of System Design and Dynamics. 2007;**1**(2):331-339

[35] Everest FA, Pohlmann KC. Master Handbook of Acoustics. New York: McGraw Hill; 2009

[36] Rayleigh L. Theory of Sound II. New York: Macmillan; 1929

[37] Crandall IB. Theory of Vibrating Systems and Sound. New York: Van Nostrand Co.; 1927

[38] Allard JF. Propagation of Sound in Porous Media. Modelling Sound Absorbing Materials. New York: Elsevier; 1993

[39] Lee YY, Lee WM, Ng CF. Sound absorption of a finite flexible micro-perforated panel backed by an air cavity. Journal of Sound and Vibration. 2005; **287**:227-243

[40] Love AEH. Sound absorption of a finite flexible micro-perforated panel backed by an air cavity. Philosophical Transcript of the Royal Society. 1888;**17**: 491-549

[41] Lauriks W, Mees P, Allard JF. The acoustic transmission through layered systems. Journal of Sound and Vibration. 1992;**155**:125-132

[42] Chung JY, Blaser DA. Transfer function method of measuring in-duct acoustic properties. I. Theory. Journal of the Acoustical Society of America. 1980; **68**(3):907-913

[43] Dalmont J-P. Acoustic impedance measurement. Part I: A review. Journal of Sound and Vibration. 2001;**243**(3): 441-459

Chapter 5

The Application of Surface Acoustic Wave Yarn Tension Sensor

Yang Feng, Ben Wang, Keyong Hu, Shuifa Sun, Bingkun Zhang, Hua Xia, Wenbo Liu, Haoda Yu and Zhen Yang

Abstract

In the current textile industry, traditional yarn tension sensors are often insufficient for the demands of modern manufacturing processes. As a result, the surface acoustic wave (SAW) yarn tension sensor has emerged as an ideal alternative. This advanced sensor is designed to enhance the efficiency of textile production by effectively addressing the challenges faced in the manufacturing environment. In this chapter, a new type of surface acoustic wave yarn tension sensor is designed and the test parameters are improved, including the design and simulations of the SAW sensor, the solution to the second-order effect problem of SAW yarn tension sensor, the design and application of the dual differential channel oscillator on SAW yarn tension sensor, and the temperature compensation of SAW yarn tension sensor based on PSO-LSSVM algorithm, which enhances the sensor's performance.

Keywords: surface acoustic wave, yarn tension sensor, second-order effect, dual differential channel oscillator, PSO-LSSVM

1. Introduction

In the textile industry, the measurement and control of tension are essential to ensure the quality and production efficiency of textiles [1]. Yarn tension directly affects the evenness, strength, and appearance quality of textiles. The uniformity, strength, and esthetic appeal of textiles are significantly influenced by the tension in the yarn. Within the realm of textile technology, yarn tension sensors are pivotal for gathering essential information. These sensors are crucial for enhancing the performance metrics and operational parameters of textile machinery [2].

Tension is a critical factor in the manufacturing of yarns, fabrics, and chemical fibers. Following the conventional spinning mill production, it is imperative that the yarn maintains an appropriate level of tension during various stages such as twisting, combing, drawing, and winding [3]. These processes are essential for achieving the desired quality and consistency in the final textile product. The existence of tension has a two-way effect on the production of the textile industry [4]. Excessive tension will cause yarn breakage, affect production efficiency, increase the consumption of

yarn and labor, and affect the quality of yarn, appearance structure, and so forth. On the contrary, if the yarn tension is lower than the production defined value, the fabric forming is lacking, the structure is loose, and it is easy to cause yarn curling, resulting in rough and uneven cloth; reducing the yarn utilization rate, and so on; and then affecting the production quality and production efficiency [5].

At present, the textile industry mainly uses direct detection yarn tension sensors [6]. Commonly used direct detection yarn tension sensors include resistance strain gauge type, differential capacitance type, magnetoelectric induction type, Hall effect type, piezoelectric film type, and optical fiber strain type [7]. They mainly have the following problems: (1) low detection accuracy and large system error; (2) output analog signal, vulnerable to electromagnetic interference in industrial environment; (3) the response speed is slow, unable to meet the needs of high-speed textile equipment (such as high-speed spinning machine, high-speed yarn combining machine, high-speed yarn winder); (4) low resolution cannot meet the requirements of high-count yarn detection; and (5) some sensor technologies are immature and still in the exploration stage.

Yarn tension sensor, as an important testing equipment in textile equipment, its development trend is toward the direction of high precision, high sensitivity, high resolution, strong anti-interference ability, strong reliability, fast response, and low cost. In order to solve the main problems of yarn tension sensor in actual production of textile industry, the realization method of doubly clamped beam yarn tension sensor based on surface acoustic wave (SAW) is proposed [8]. This kind of sensor has the advantages of SAW device: (1) The response time of SAW device is fast, which is suitable for high-speed textile equipment; (2) the dual-channel differential frequency output structure has strong anti-interference performance and is not easily affected by the environment; (3) the doubly clamped beam structure is reliable, reasonable, and stable; (4) high detection accuracy, which can meet the detection requirements of high-count textiles (such as extremely fine yarn with more than 100 counts); and (5) high sensitivity, clear enough to distinguish less than 0.01 N tension changes, can be widely used in the textile industry.

This chapter designs a new type of yarn tension sensor based on surface acoustic wave and gives a detailed overview of device design, simulation, circuit, and temperature compensation. Section 2 shows the design and simulations of the SAW sensor. Section 3 shows the solution to the second-order effect problem of SAW yarn tension sensor. Section 4 shows the design and application of the dual differential channel oscillator on SAW yarn tension sensor. Section 5 shows the temperature compensation of SAW yarn tension sensor based on PSO-LSSVM algorithm.

2. Design and simulations of the SAW sensor

Correct yarn tension is essential for maintaining product quality and manufacturing efficiency, as it impacts production speed and processing ease, with improper tension potentially causing slack or breaks [9]. Traditional yarn tension sensors face limitations in high-speed environments due to interference and low sampling rates. The surface acoustic wave (SAW) sensors provide a reliable, sensitive solution for modern textile needs, yet single-clamped cantilever designs can be less robust in real-world applications [4].

This section details a design methodology for a yarn tension sensor employing surface acoustic waves, establishing a linear correlation between sensor frequency shift and tension. Addressing material selection for piezoelectric substrates, optimizing substrate dimensions, correctly placing Inter-digital Transducers (IDTs), and

constructing the measurement system are paramount. The measurement system's architecture is scrutinized in anticipation of rigorous experimental validation.

2.1 Principle of the SAW yarn tension sensor

A standard yarn tension sensor is composed of two Interdigital Transducers (IDTs) that are etched onto a piezoelectric material [10], along with two stationary gaskets and a support pedestal, as depicted in **Figure 1**.

The SAW based on doubly clamped beam tension sensor, depicted in **Figure 2**, consists of a SAW Delay-line Oscillator, an amplifier, and a yarn guide (**Figure 3**). It measures yarn tension by the tension exerted on the three pulleys (A, B, C) (**Figure 2**) [11].

Applying tension at pulley A induces stress in the piezoelectric sensor, causing voltage fluctuations that alter the SAW Delay-line Oscillator's frequency, which is directly proportional to yarn tension. The oscillator's output frequency is:

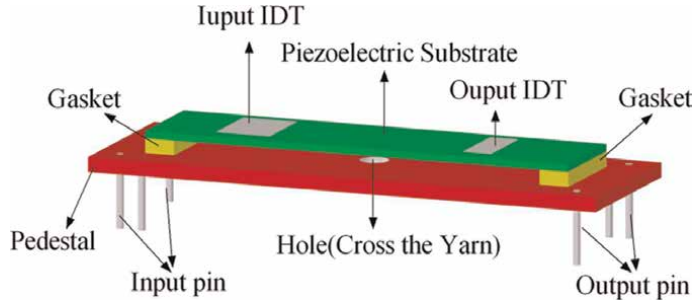

Figure 1.
The structure of the doubly clamped beam [1].

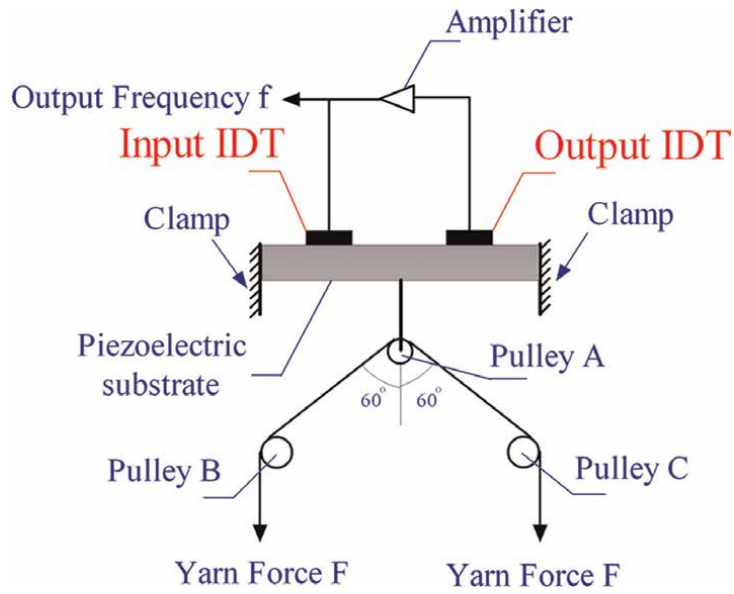

Figure 2.
The measurement system of the doubly clamped beam SAW yarn tension sensor [1].

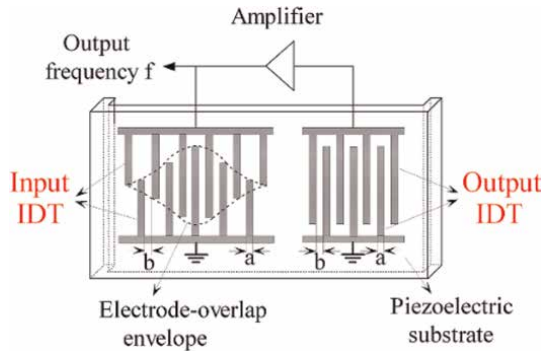

Figure 3.
Delay-line Oscillator SAW structure [1].

$$f = f_0 + \Delta f \tag{1}$$

We know the output frequency shift Δf is in direct proportion to the yarn tension F, which is

$$\Delta f = kF \tag{2}$$

The Eq. (1) can be written as

$$f = f_0 + kF \tag{3}$$

2.2 The choice of the piezoelectric substrate material

Piezoelectric single crystals in SAW device manufacturing include $L_iT_aO_3$, $L_iN_bO_3$, LGS ($La_3Ga_5S_iO_{14}$), LBO, $Li_2B_4O_7$, and S_iO_2. These piezoelectric crystals exhibit anisotropic properties, meaning that their elastic modulus E varies with direction. $[D]$ is elastic stiffness matrix, which is employed to describe their characteristics.

In accordance with Hooke's law, the stress experienced by the piezoelectric crystal is directly proportional to its strain, which is

$$T_i = D_{ij}S_j \tag{4}$$

In rectangular coordinate system, Eq. (4) can be expressed in matrix form:

$$[T] = [D][S] \tag{5}$$

Eq. (5) can be written as

$$\begin{bmatrix} T_1 \\ T_2 \\ T_3 \\ T_4 \\ T_5 \\ T_6 \end{bmatrix} = \begin{bmatrix} D_{11} & D_{21} & D_{31} & D_{41} & D_{51} & D_{61} \\ D_{12} & D_{22} & D_{32} & D_{42} & D_{52} & D_{62} \\ D_{13} & D_{23} & D_{33} & D_{43} & D_{53} & D_{63} \\ D_{14} & D_{24} & D_{34} & D_{44} & D_{54} & D_{64} \\ D_{15} & D_{25} & D_{35} & D_{45} & D_{55} & D_{65} \\ D_{16} & D_{26} & D_{36} & D_{46} & D_{56} & D_{66} \end{bmatrix} \begin{bmatrix} S_1 \\ S_2 \\ S_3 \\ S_4 \\ S_5 \\ S_6 \end{bmatrix} \tag{6}$$

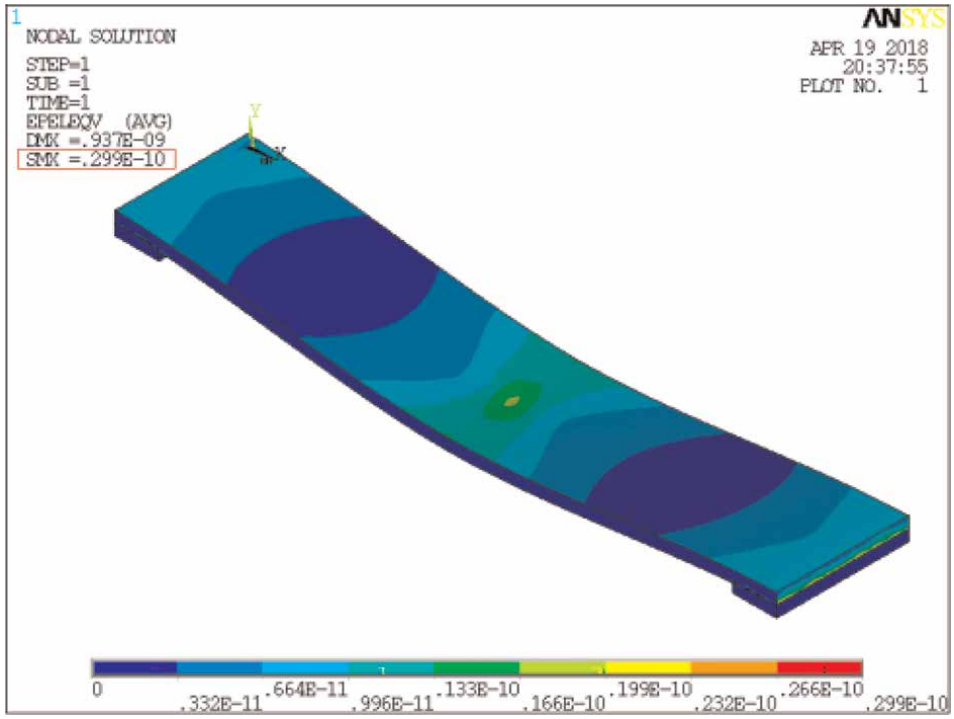

Figure 4.
The strain distribution patterns of the quartz substrate [1].

Using ANSYS 14.0, we modeled these materials and determined the strain in a doubly clamped beam under a constant tension of 0.2 N. The maximum strain, found with ANSYS, occurred with quartz ($SMX = 2.99 \times 10^{-9}$ in **Figure 4**), making it our piezoelectric substrate choice. The quartz model's strain and stress under tension are depicted as follows, with minimum and maximum strain areas colored blue and yellow, respectively [12].

2.3 The choice of the piezoelectric die size

The Von Mises stress criterion is employed to predict the initiation of failure in ductile materials, providing an insight into the stress distribution patterns within a given model [13].

Utilizing ANSYS 14.0, the Von mises stress is depicted in **Figure 5**. When the force 0.2 N is exerted at the midpoint of the doubly clamped beam, the stress to 2.9049 MPa, as indicated by the red frame in **Figure 5** [14].

The sensor is packaged with a maximum length of 30 mm, a minimum aperture of 4 mm, and a 0.5 mm bus-bar for signal transfer. Accounting for 0.5 mm margins, the sensor's minimum width is 6 mm. The doubly clamped beam size is constrained by:

$$\begin{cases} 22\ mm \le L \le 30\ mm \\ 6\ mm \le W \le 10\ mm \end{cases} \tag{7}$$

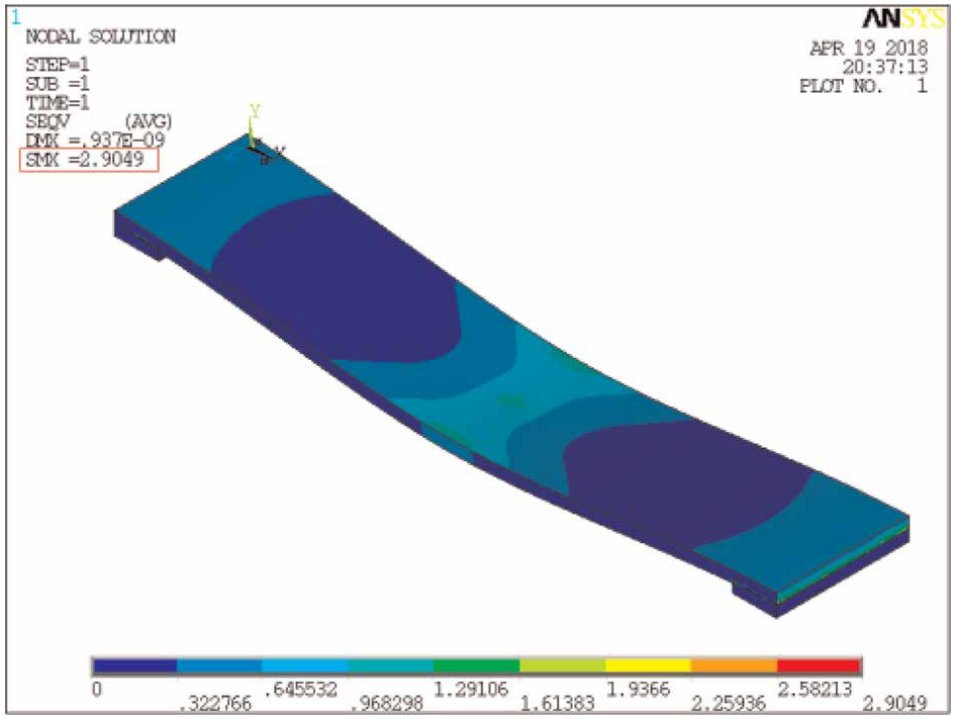

Figure 5.
The stress distribution patterns of the quartz substrate [1].

Following our stated method, we used a quartz substrate to make 25 doubly clamped beams of different sizes and analyzed their stress. **Table 1** shows the Von Mises Stress for each size.

2.4 The placement of IDTs

To achieve the highest sensitivity for the yarn tension sensor, it is essential that the SAW IDTs are positioned in the regions of the piezoelectric substrate where the strain is at its peak [15].

We constructed a quartz doubly clamped beam with size L = 30 mm, W = 6 mm, H = 0.5 mm by ANSYS 14.0, and then loaded the yarn tension F = 0.2 N.

Figure 6(b) plots beam length against Y-axis strain on the piezoelectric substrate, peaking at the midpoint. A 2 mm gap at the center allows for a guide bar. IDTs are strategically placed near points of high strain: input near B and output near C in **Figure 6(c)**, and input near A and output near D in **Figure 6(d)** [16, 17].

2.5 The construction of measurement system

Aimed at the development of a SAW yarn tension sensor measurement system, this section focuses on designing and implementing the peripheral measurement circuitry for the SAW yarn tension sensor [18]. Moreover, through the application of an optimized structural design, the yarn tension can be accurately doubled on the piezoelectric substrate of the SAW device, thereby enhancing the measurement precision of the SAW yarn tension sensor [19].

No.	1	2	3	4	5	6	7	8	9	10	11	12	13	14	15	16	17	18	19	20	21	22	23	24	25
W (mm)	6	6	6	6	6	7	7	7	7	7	8	8	8	8	8	9	9	9	9	9	10	10	10	10	10
L (mm)	22	24	26	28	30	22	24	26	28	30	22	24	26	28	30	22	24	26	28	30	22	24	26	28	30
σ (MPa)	2.0931	2.3951	2.4486	2.7334	2.9049	2.0167	2.2233	2.3738	2.4798	2.8010	1.8886	2.1198	2.2354	2.3478	2.4392	1.6221	1.7392	1.8291	2.0369	2.1081	1.4705	1.6888	1.7251	1.9318	2.0885

Table 1.
The Von Mises Stress of the doubly clamped beam with the quartz substrate (25 different sizes, h = 0.5 mm).

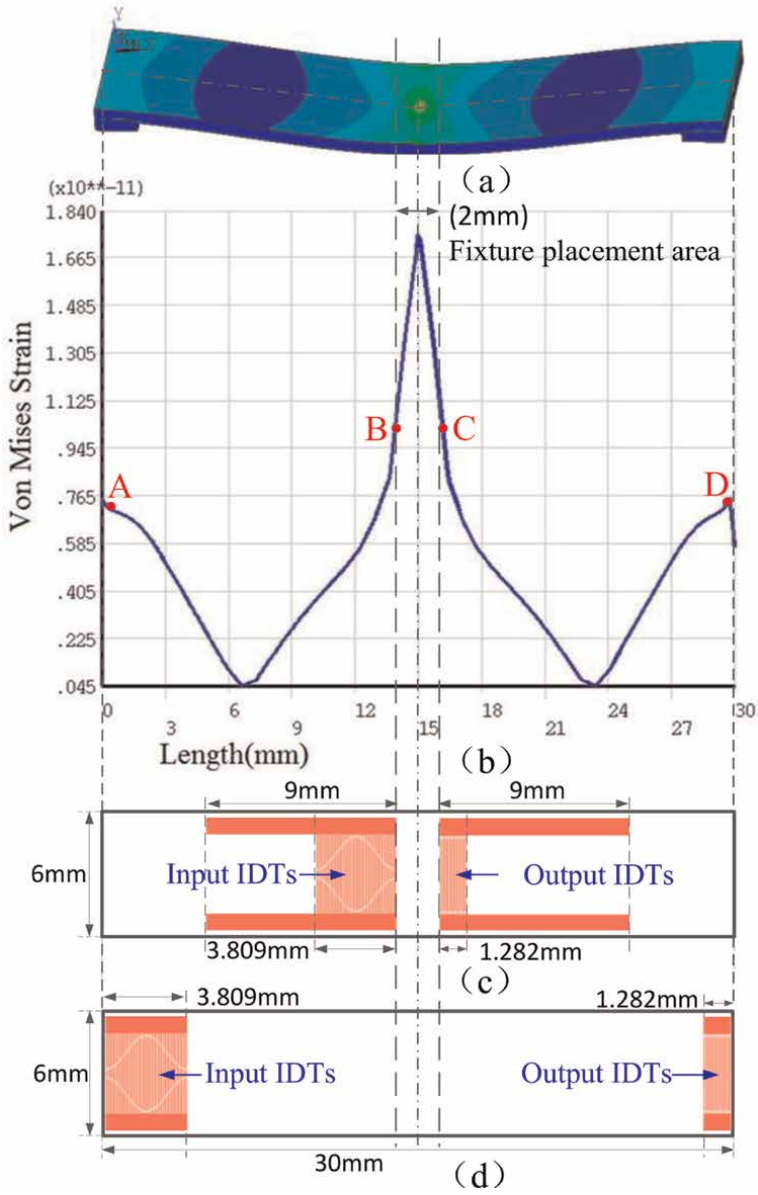

Figure 6.
Design the placement of IDTs [1].

When the angle α is set to 120, 90, 60, and 0 degrees, the magnitude of force F_A corresponds to F, $\sqrt{2}F$, $\sqrt{3}F$, and $2F$, respectively. It is evident that the smaller the angle α, the larger the force F_A, which in turn indicates a higher sensitivity of the SAW yarn tension sensor. As illustrated in **Figure 7(a)**, when α is 120 degrees, F_A equals the yarn tension F ($F_A = F$). In this section, with α at 0 degrees, F_A is twice the yarn tension ($F_A = 2F$). Comparing this to Eq. (5), it can be concluded that the sensitivity of the SAW yarn tension sensor in this scenario is doubled [21–23].

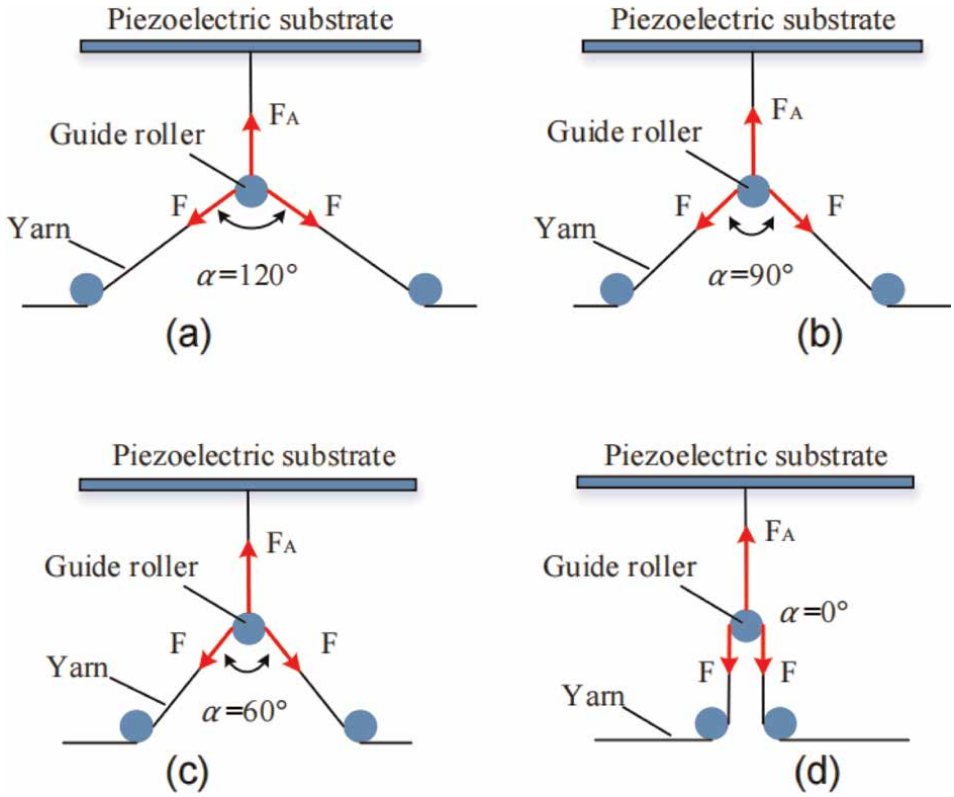

Figure 7.
The position diagram of the yarn guide rollers [20].

2.6 The realization of the measurement

Figure 8 illustrates the SAW yarn tension sensor assembly, with the SAW device mounted on a PCB fixed to the main structure, and a slider with a guide roller connected to the substrate *via* a bolt [20]. **Figure 9** illustrates the SAW yarn tension measurement system, integrating the measurement structure and circuit to enhance the sensor's accuracy and reliability [24, 25].

3. Solution to the second-order effect problem of SAW yarn tension sensor

Preceding chapters detailed the design and simulation of SAW sensor beams for yarn tension measurement, tackling challenges such as slow response times and the limitations of analog signal outputs [26]. As a derivative of SAW pressure sensors, the tension variant employs a single broadband reflective delay line, necessitating strain transfer optimization within the piezoelectric substrate [27]. The SAW's phase variance is directly proportional to the MEL variation along the delay line. This chapter therefore focuses on enhancing sensor performance by scrutinizing the electrode sensor structure and the fabrication process of the piezoelectric substrate. Strategies to

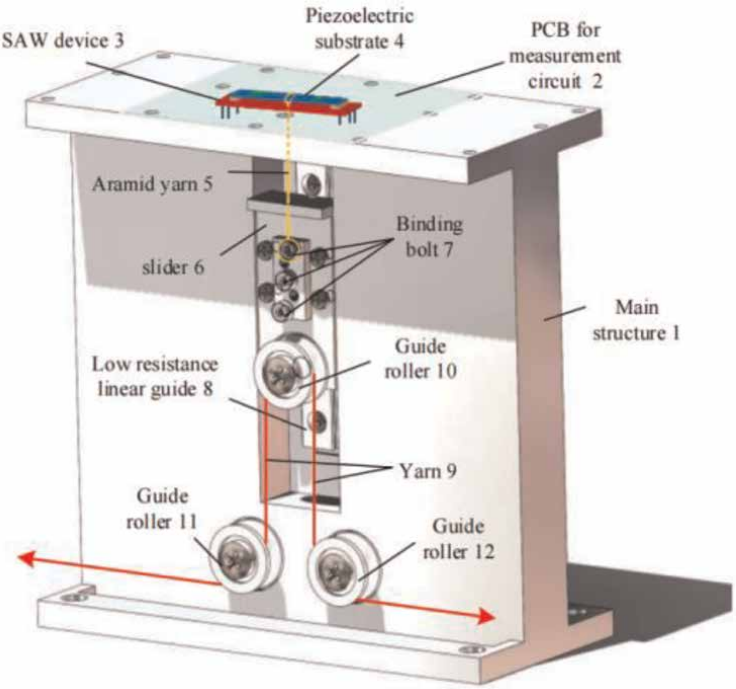

Figure 8.
The construction diagram of the yarn tension measurement system [20].

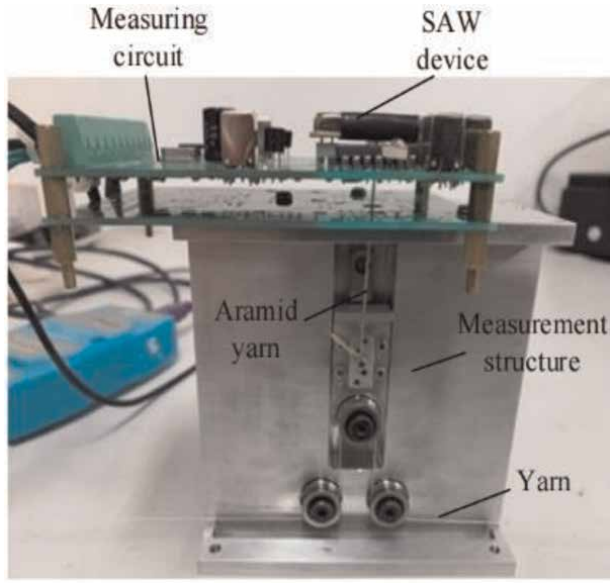

Figure 9.
The SAW yarn tension measurement system [20].

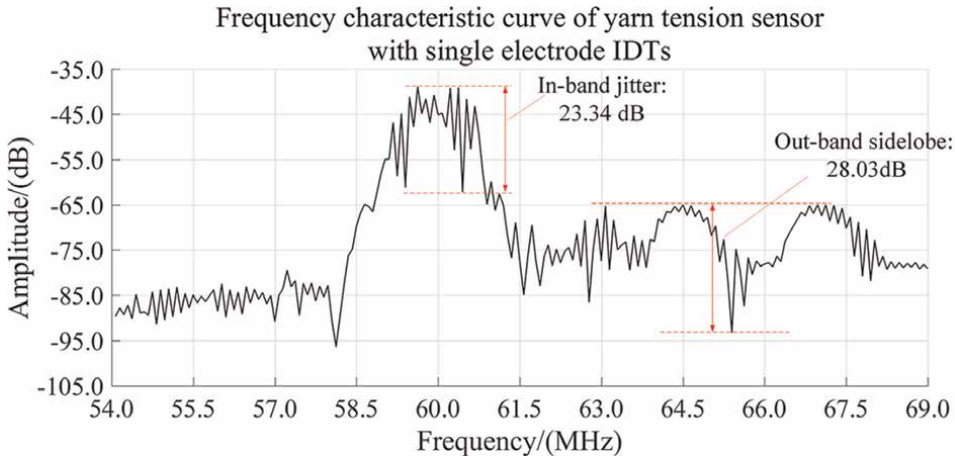

Figure 10.
Frequency characteristic curve of yarn tension sensor with single electrode IDTs [30].

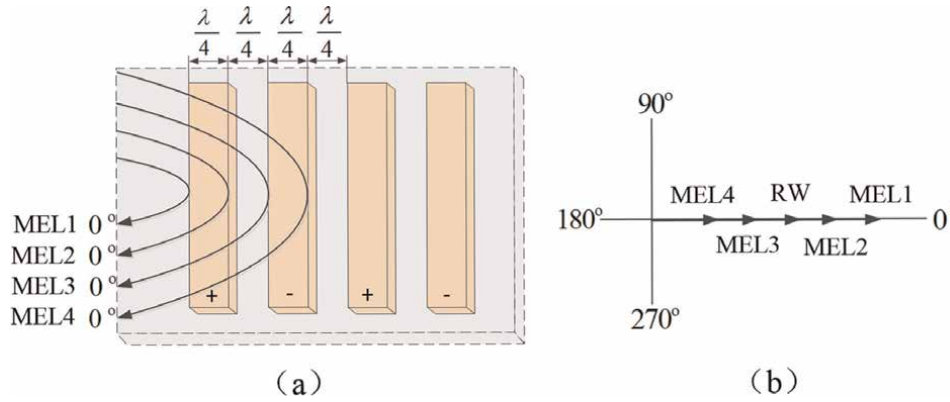

Figure 11.
Electrode reflections of the single electrode IDT [30].

mitigate in-band ripples and out-of-band suppression include the implementation of split electrode IDTs and the etching of bidirectional slots [28].

3.1 Analysis of single electrode IDT of the SAW yarn tension sensor

Single electrode IDTs are a standard feature in SAW devices, where the electrode width matches the inter-electrode spacing [29].

For the assessment of the frequency response of the single electrode IDT SAW yarn tension sensor, an Agilent E5061A ENA-L network analyzer was utilized. The in-band ripples measured 23.34 dB, while the out-of-band suppression levels were recorded at 28.03 dB, as depicted in **Figure 10**.

Periodic IDTs generate RWs from metal electrodes. In **Figure 11(a)**, MEL1-4 denote edge-induced mass/electrical reflections, synchronized [31]. These are transmitted to the piezoelectric substrate's central region for superposition. The transducer center receives a composite RW signal, shown in **Figure 11(b)**, which degrades SAW device performance **Figure 12**.

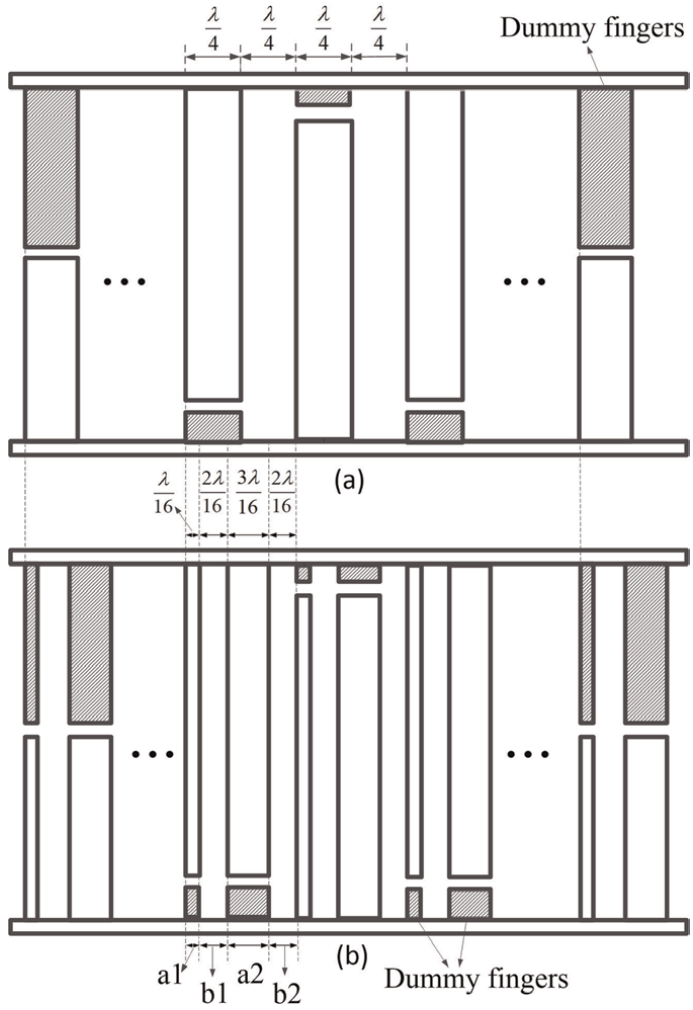

Figure 12.
Structure diagram of split electrode IDTs [30].

3.2 Solution to the in-band ripples of frequency characteristic

Figure 13 illustrates the electrode reflections from a single electrode IDT, where the in-band ripples are notably large. To mitigate the in-band ripples, it is essential to address the issue of electrode reflections.

Electrode reflections arise due to alterations in the acoustic impedance of the metal film that constitutes the electrodes within the acoustic transmission medium [30]. Acoustic impedance changes result mainly from shunting surface piezoelectric fields and the mass loading effect of the electrodes.

The alteration in acoustic impedance due to the termination of surface piezoelectric fields is

$$\left.\frac{\Delta Z}{Z}\right|_P = \left|\frac{\Delta v}{v}\right| \approx \frac{1}{2}K^2 \tag{8}$$

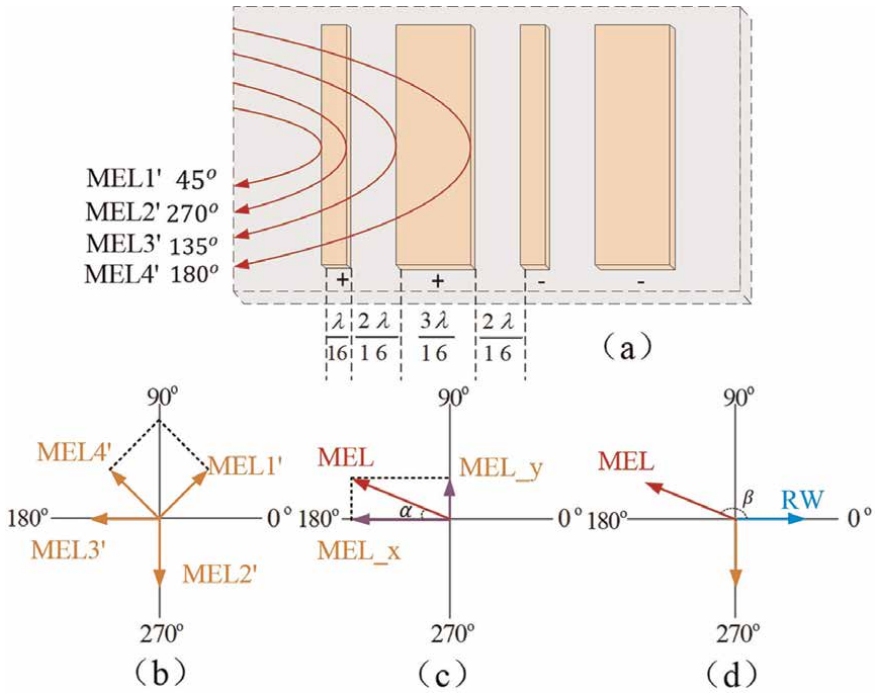

Figure 13.
Aperture lengths of single-electrode IDTs [30].

By substituting $K^2 = 0.0014$ into Eq. (8)

$$\left.\frac{\Delta Z}{Z}\right|_p = 0.0007 \tag{9}$$

The change of the acoustic impedance caused by the mass load is

$$\left.\frac{\Delta Z}{Z}\right|_m \approx \frac{2}{3}\frac{\rho_m}{\rho_s}\frac{h}{\lambda} \tag{10}$$

Small $\left.\frac{\Delta Z}{Z}\right|_m$ can reduce the electrode reflection. By substituting $p_m = \frac{2.7g}{cm^3}$, $p_s = \frac{2.65g}{cm^3}$ and $h = 0.2\,\mu m$ into Eq. (10),

$$\left.\frac{\Delta Z}{Z}\right|_m \approx 0.0026 \tag{11}$$

Therefore, we know from Eqs. (9) and (11) that the total change of the acoustic impedance is

$$\frac{\Delta Z}{Z} = \left.\frac{\Delta Z}{Z}\right|_P + \left.\frac{\Delta Z}{Z}\right|_m \approx 0.0007 + 0.0026 = 0.0033 \tag{12}$$

To more effectively counteract the impact of electrode reflections, split electrode interdigital transducers (IDTs) are employed in the surface acoustic wave (SAW)

device to diminish these reflections. The structure of the device is depicted in **Figure 13** and fulfills the following

$$a1 = \frac{1}{16}\lambda, b1 = \frac{2}{16}\lambda, a2 = \frac{3}{16}\lambda, b2 = \frac{2}{16}\lambda \tag{13}$$

We calculate the phases of MEL1', MEL2', and MEL4' to obtain the combined phase of MEL y; similarly, we calculate the phases of MEL3' and MEL4' to obtain the combined phase of MEL x, as depicted in **Figure 10(c)**. In this analysis, we assume the magnitude of each phasor to be unity, and then, we get

$$\mathrm{MEL\_x} = \frac{\sqrt{2}}{2}MEL1' + \frac{\sqrt{2}}{2}MEL4' + MEL3' \tag{14}$$

$$\mathrm{MEL\_y} = \frac{\sqrt{2}}{2}MEL1' + \frac{\sqrt{2}}{2}MEL4' + MEL2' \tag{15}$$

$$\alpha = \tan^{-1}\frac{\mathrm{MEL\_y}}{\mathrm{MEL\_x}} = \tan^{-1}\frac{\sqrt{2}-1}{-1} = -22.5^{o} \tag{16}$$

To reduce the sidelobes in a surface acoustic wave (SAW) delay-line Oscillator, the electrode-overlap envelope of the input transducer is modified by applying a weighting function, specifically the Hamming function as depicted in Eq. (17). This approach adjusts the amplitude distribution across the electrodes to minimize the undesired sidelobe levels.

$$h(t) = 0.08 + (1 - 0.08)\cos^2\frac{\pi t}{2\tau} = 0.54 + 0.46\cos\frac{\pi t}{\tau}\ \tau \le t \tag{17}$$

The overall response $H(f)$ can be split into two summations relating input and output IDTs responses, exactly as follows.

$$H(f) = H_{out}(f)H_{in}(f) \tag{18}$$

The frequency response of output IDTs $H_{out}(f)$ is

$$H_{\mathrm{out}}(\omega) = \sum_{m=1}^{N_0} We^{-j\omega\frac{x_m}{v}} \tag{19}$$

The frequency response of output IDTs $H_{in}(f)$ is

$$H_{\mathrm{in}}(\omega) = \sum_{n=1}^{N_i} W\left(0.54 + 0.46\cos\frac{\omega\frac{x_n}{v}}{2.1}\right)e^{-j\omega\frac{x_n}{v}} \tag{20}$$

The -3 dB bandwidth can be written as

$$BW = \frac{\Delta f_{-3dB}}{f_0} = \frac{\sqrt{2}}{2}|H(f)| = \frac{\sqrt{2}}{2}|H_{in}(\omega)||H_{out}(\omega)| \tag{21}$$

Given that $N_o = 24$, we determined the relationship between B and $\mathrm{N_i}$ as follows:

$$BW = \frac{\Delta f_{-3dB}}{f_0} = \frac{1.2965}{N_i} \tag{22}$$

Piezoelectric substrate			Center frequency *(MHz)*	-3 dB Bandwidth *(MHz)*	Electrode width *(μm)*	Spacing between electrodes *(μm)*	Aperture width of IDT *(μm)*	Center distance between input IDT and output IDT *(mm)*	Number of electrodes	
Length *(mm)*	**Width *(mm)***	**Thickness *(mm)***							**The input IDT**	**The output IDT**
30	6	0.5	60	0.720	a1 = 2.2896	b 1 = 6.5792	3588.7333	Sensor-A = 4.5455	145	49
					a2 = 9.8688	b2 = 6.5792		Sensor-B = 25.4545		

Table 2.
Design parameters of yarn tension sensor based on ST-X quartz substrate.

The SAW delay-line oscillator is designed with a bandwidth $BW = 1.2\%$, which corresponds to an input IDTs count of $N_i = 72$. The design specifications for the yarn tension sensor, which utilizes a doubly clamped beam, are detailed in **Table 2**.

Table 2 shows the design parameters of the split-electrode IDTs of the SAW yarn tension sensor on ST-X quartz, and the prepared sensor is shown in **Figure 14**. Frequency response in **Figure 15** indicates:

1. IDTs minimize in-band ripples (0.93 dB), enhancing frequency response.

2. Out-of-band suppression remains suboptimal at 25.63 dB, failing to improve sensor's suppression capability noteworthily.

3.3 Solution to the out-of-band suppressions of frequency characteristic

The transducers on piezoelectric substrate emit SAWs and BAWs. BAW's multidirectional propagation can intercept receiving transducers, causing spurious responses that degrade SAW frequency performance [32].

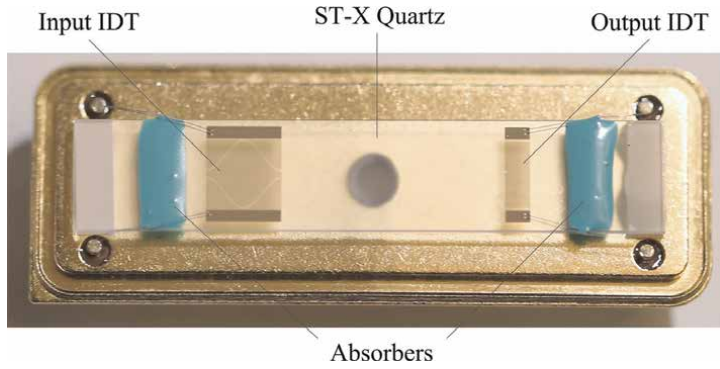

Figure 14.
The split-electrode IDTs of the yarn tension sensor [30].

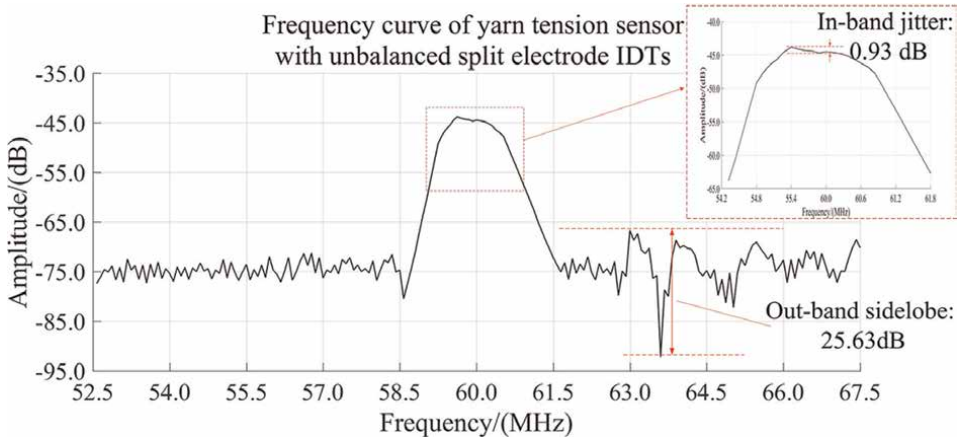

Figure 15.
Frequency curve of yarn tension sensor with split-electrode IDTs [30].

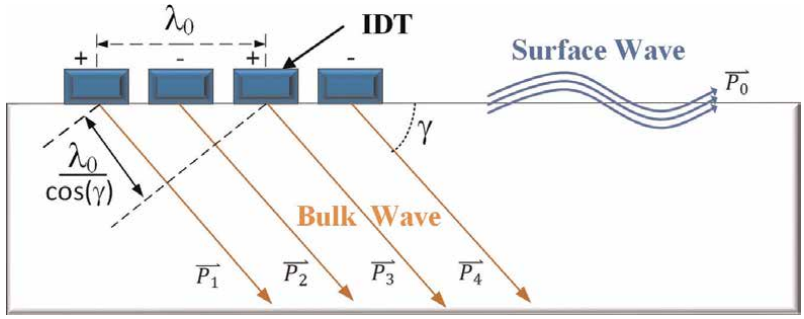

Figure 16.
Schematic diagram of BAW stimulated by IDT [33].

The condition for achieving phase synchronization can be expressed as follows:

$$v_0 = f_0 \lambda_0 = \frac{v(\gamma)}{cos\gamma} \tag{23}$$

In **Figure 16**, the wave vector that travels along the surface of the piezoelectric substrate is represented by $2\pi/\lambda_0$. Based on the properties of wave vectors, Eq. (23) can be requestioned as follows:

$$p_O = 2\pi/\lambda_0 = p_s = p(\gamma)cos\gamma \tag{24}$$

In an isotropic medium, the value of $v(\gamma)$ is contingent upon the wave mode, the substrate material, the surface cut orientation, the transducer direction, and the ambient temperature [34–36]. Once these variables are specified, the center frequency is determined by the inclination angle as follows:

$$f_0 = \frac{1}{\lambda_0} \cdot \frac{v(\gamma)}{cos\gamma} \tag{25}$$

By contrasting the Deep Bulk Acoustic Wave (DBAW) scenario with the limiting case of SSBW, we can obtain the following from Eq. (25):

$$\frac{(f_0)_{DBAW}}{(f_0)_{SBAW}} = \frac{v(\gamma)}{v_{SBAW}} \cdot \frac{cos\,\gamma_c}{cos\gamma} = \frac{1}{cos\gamma} \tag{26}$$

For DBAW devices, enhancement factors $(1/cos\gamma)$ of 2 or more (implying $\gamma \geq 60^{\circ}$) are considered achievable with favorable material and cut conditions.

3.3.1 Arranging acoustic absorbers at ends of piezoelectric substrate

Parasitic reflections from piezoelectric substrate edges increase frequency response ripples, known as the transducer edge reflection phenomenon (**Figure 17**). Applying acoustic absorbers like silicone rubber to these edges mitigates these reflections, improving SAW device performance [33, 37, 38].

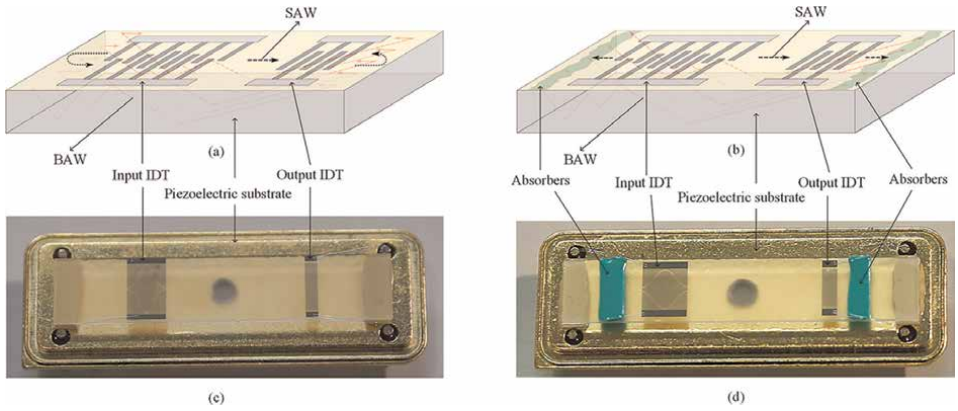

Figure 17.
Reflection of BAW at the ends of piezoelectric substrate [33].

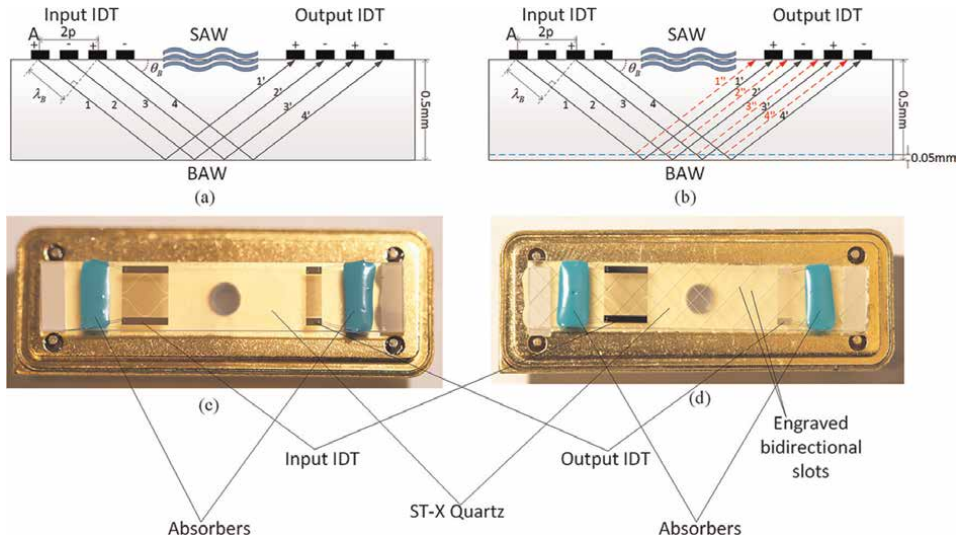

Figure 18.
Change in BAW reflection excited by IDT with the grooves [33].

3.3.2 Piezoelectric substrate with slotted bi-directional grooves

Slotting cutters are precision tools used to etch narrow channels on the back of piezoelectric substrates, disrupting BAW signal pathways, as shown in **Figure 18**. **Figure 19** shows the substrate magnified 120x.

Implemented BAW configurations with selected modes and materials effectively scatter BAW *via* acoustic absorbers and substrate grooves, as shown in **Figure 20**.

1. Asymmetric split electrode IDTs in SAW sensors minimize in-band ripples to just 0.82 dB, effectively controlling out-of-band fluctuations.

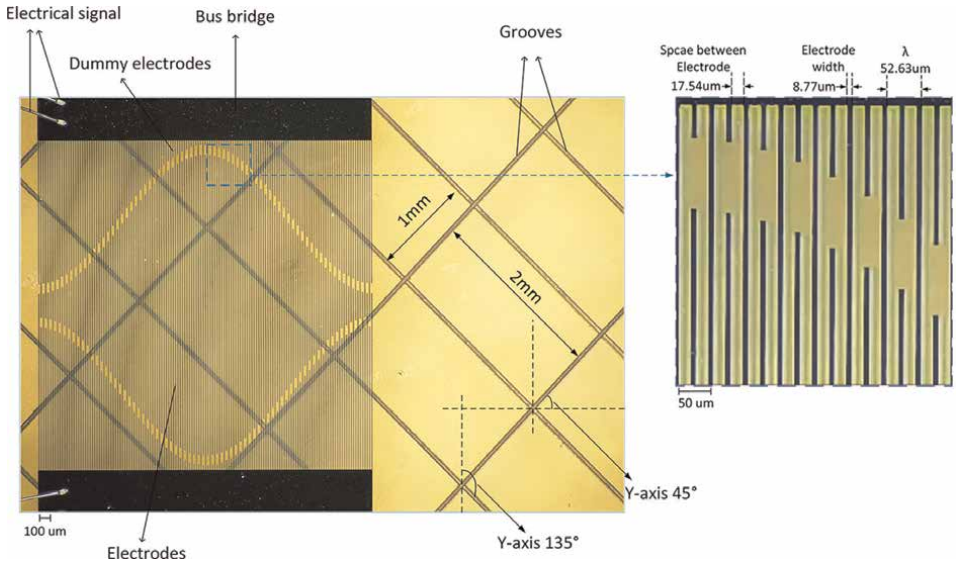

Figure 19.
Grooves on the piezoelectric substrate of SAW yarn sensor (magnified view with 120x) [33].

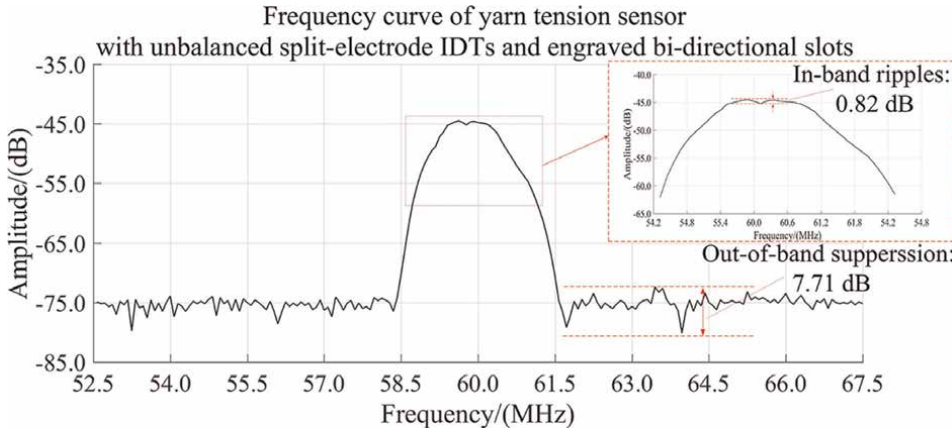

Figure 20.
Frequency curve of yarn tension with split-electrode IDTs and engraved bidirectional slots [30].

2. Bidirectional grooves on the substrate's reverse side achieve a substantial reduction in out-of-band attenuation to 7.712 dB, effectively tackling the out-of-band attenuation issue.

The newly developed SAW yarn tension sensor, characterized by a central frequency of 59.83 MHz, a bandwidth fraction of 1.33%, and a measurable force range from 0 to 1000 mN, exhibited the following performance metrics in laboratory tests: linearity of 1.02%, hysteresis of 0.59%, repeatability of 1.11%, and accuracy of 1.34%. The bidirectional slot carving technique stands out as a solution for improved out-of-band suppression [39].

4. Design and application of the dual differential channel oscillator on SAW yarn tension sensor

The SAW yarn tension sensor, when combined with an oscillation circuit, enhances frequency stability by addressing key issues:

1. Employing split electrodes choosing ST-X quartz for the substrate, and engraving bidirectional slots are strategies to reduce higher-order effects, minimize electrode reflection, and lessen BAW impact.

2. The design of a dual differential channel SAW oscillator (SAWO), including dual delay line oscillators, an integrated mixer, and an LC low-pass filter, is aimed at countering temperature-induced interference, with PCB analysis conducted using an Agilent E5061A ENA-L.

4.1 Principle of the SAWO dual differential channel circuit

Figure 21 depicts the layout of the dual differential SAW oscillator system, which is divided into three main components:

1. A pair of identical SAW oscillators (SAWOs). One is tasked with detecting yarn tension on the piezoelectric substrate and is referred to as the sensing channel, while its counterpart acts as the reference channel.

2. A built-in mixer. When the frequency outputs from both SAWOs are combined in the mixer, the resulting output consists of both the sum and the difference of the two frequencies.

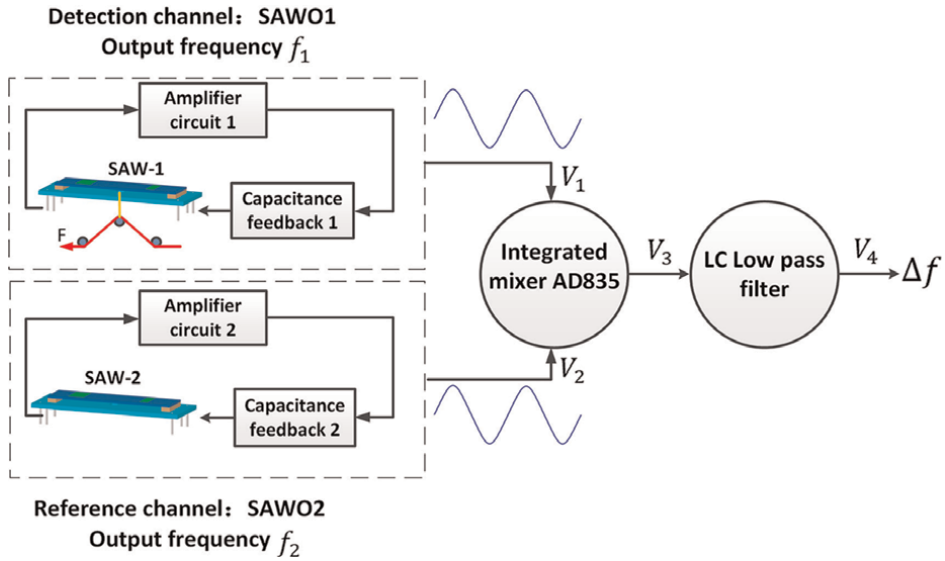

Figure 21.
The diagram of a SAW yarn tension sensor integrated with a dual differential circuitry system [15].

3. An LC low-pass filter. As the mixer's output signal passes through this filter, the resulting signal is the frequency difference (specifically, the difference component of the mixer's output signal).

Within this setup, SAW1 serves to gauge the yarn tension, while SAW2 operates as a reference. The output voltage V_1 from the SAWO1 can be formulated as:

$$V_1 = \sqrt{2}U_1 sin\left(2\pi f_1 t + \varphi_1\right) \tag{27}$$

The output signal V_2 of the SAWO2 can be expressed as:

$$V_2 = \sqrt{2}U_2 sin\left(2\pi f_2 t + \varphi_2\right) \tag{28}$$

AD835 is a voltage output multiplier produced by analog devices, which can complete the function of $W = XY + Z$.

Upon transmission through the integrated mixer AD835, the output signals V_1 and V_2 from the two SAW oscillators (SAWOs) intermingle. The resultant mixing signal V_3 is denoted as

$$\begin{aligned} V_3 = V_1 \times V_2 &= \left[\sqrt{2}U_1 sin\left(2\pi f_1 t + \varphi_1\right)\right]\left[\sqrt{2}U_2 sin\left(2\pi f_2 t + \varphi_2\right)\right] \\ &= 2U_1U_2\{cos\left[2\pi\left(f_1 - f_2\right) + \left(\varphi_1 - \varphi_2\right)\right] - cos\left[2\pi\left(f_1 + f_2\right) + \left(\varphi_1 + \varphi_2\right)\right]\} \end{aligned} \tag{29}$$

In Eq. (29), the mixing signal contains $f_1 - f_2$ and $f_1 + f_2$ signals. According to **Figure 21**, the mixer output signal V_3 passes through the low-pass filter, and the output signal V_4 is:

$$V_4 = K_L U_1 U_2 cos\left[2\pi\left(f_1 - f_2\right)t + \left(\varphi_1 - \varphi_2\right)\right] \tag{30}$$

The simultaneous application of the input supply voltage *Vi* to the dual surface acoustic wave (SAW) oscillator system, along with the symmetry of the system relative to the initial phase of SAWO1 and SAWO2, should be:

$$\varphi_1 = \varphi_2 \tag{31}$$

By inserting Eq. (31) into Eq. (30), the output signal V_4 is transformed into:

$$V_4 = K_L U_1 U_2 cos\left[2\pi\left(f_1 - f_2\right)t\right] == KU_1U_2 cos\left(2\pi\Delta f_{LPF} t\right) \tag{32}$$

According to Eq. (32), the implementation of a dual channel design can mitigate external disturbances to some extent, thereby ensuring the stability and enhancing the system's resistance to interference.

In practice, device asymmetry and parameter inconsistencies mean SAWO1's f1 and SAWO2's f2 would not match perfectly. Thus, it is essential to calibrate the sensing and reference channels before testing.

4.2 Application of dual differential channel circuit on sensor

SAWOs use Pierce or Colpitts configurations for low-noise performance, each with distinct circuit layouts. The Pierce configuration, with its series-resonant

circuit, is preferred for high frequencies due to series resonance. The Colpitts configuration, with its parallel-resonant circuit, maintains stable frequency at lower ranges. For high-frequency SAW devices, the Pierce design enhances frequency stability.

4.3 Test and application of the dual differential channel of the SAWO

Modify the variable capacitor Cx, as depicted in **Figure 22(b)**. For the purposes of this experiment, the compensatory value is established as the fundamental calibration value for the differential frequency output, representing the oscillation frequency disparity between the yellow and green curves highlighted in the red box in **Figure 23**.

Upon applying the yarn tension F to the sensing channel, the differential frequency signal produced by the yarn tension sensor's circuitry is adjusted by subtracting the baseline calibration value. Consequently, this results in the isolation of the frequency difference component. The output signal of AD835 mixer is shown in **Figure 24**. The differential frequency signal of low-pass filter is shown in **Figure 25**.

This measured value is essential for calibrating the detection and reference channels. Therefore, the fundamental calibration can be expressed as:

$$\Delta f_{LPF} = 610k + \Delta f_T + \Delta f_F \tag{33}$$

The low-pass filter of the differential circuit's detection function allows the yarn tension sensor to mitigate environmental interference effectively.

4.4 Test of dual differential channel circuit stability

Circuit stability is vital for SAW sensor performance, with frequency stability indicating unpredictable frequency changes over time. The frequency stability curve of SAWO1 is shown in **Figure 26**. The frequency stability curve of low-pass filter output is shown in **Figure 27**. Short-term stability is measured using Allan variance in

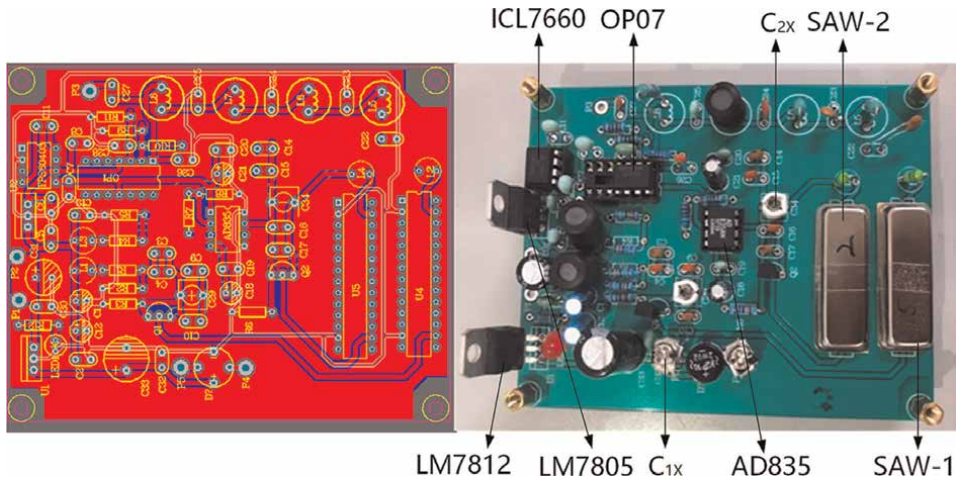

Figure 22.
Diagram of the dual differential surface acoustic wave oscillator system [15].

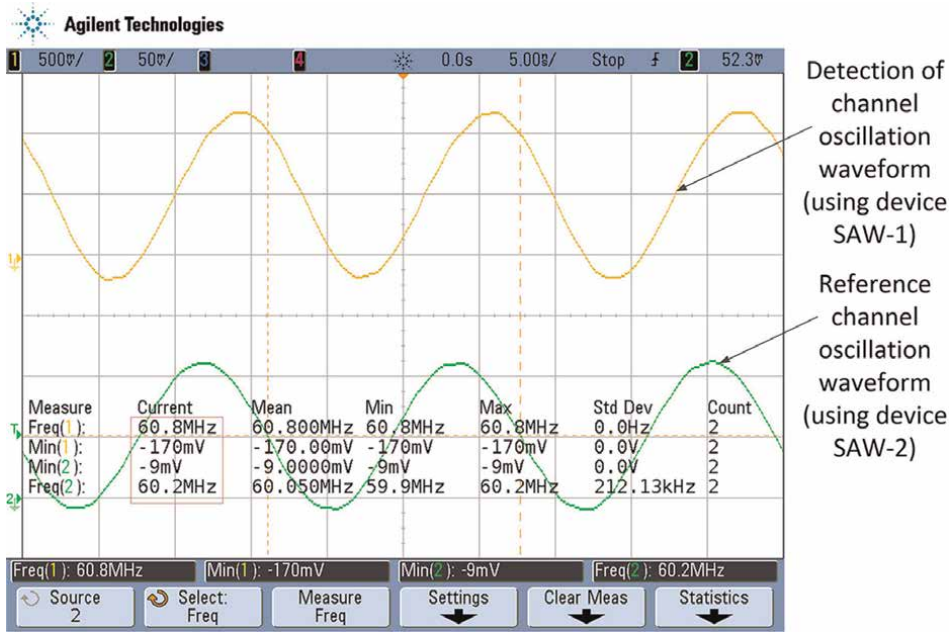

Figure 23.
Test waveform diagram of the SAW oscillator after adjusting the capacitor Cx [15].

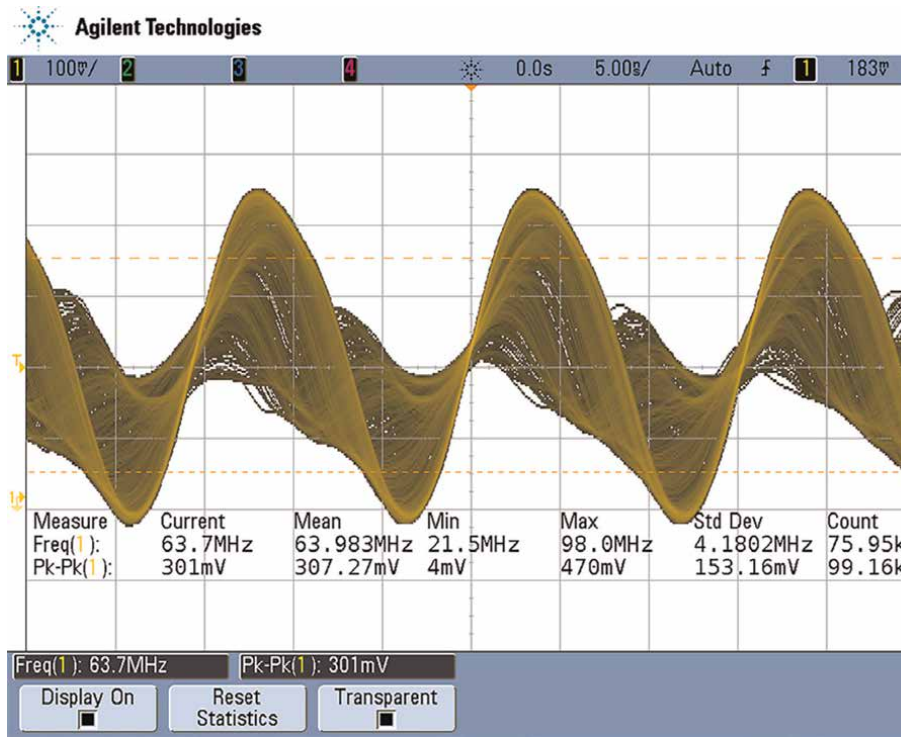

Figure 24.
The output signal of AD835 mixer [15].

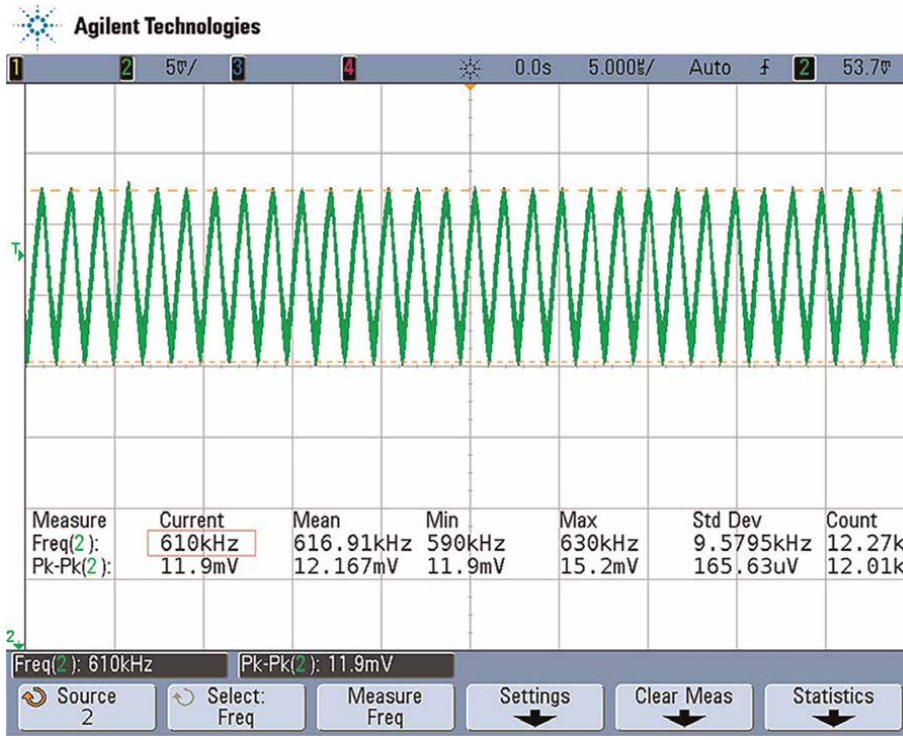

Figure 25.
The differential frequency signal of low-pass filter [15].

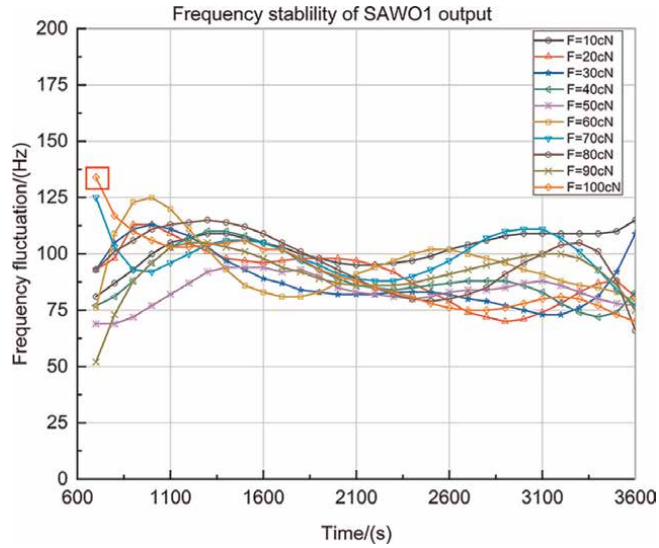

Figure 26.
Frequency stability of SAWO1 with tension [15].

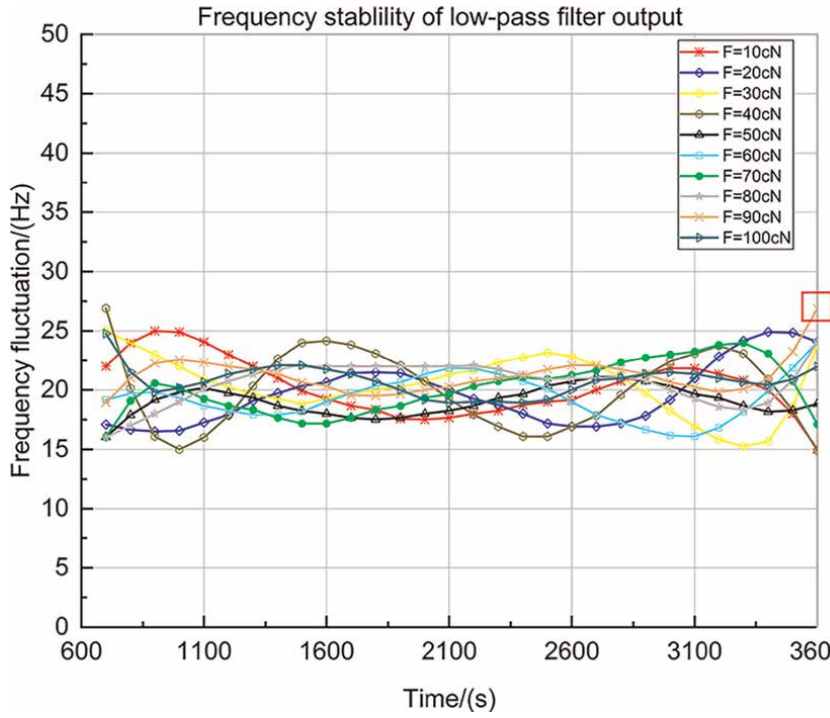

Figure 27.
Frequency stability of low-pass filter output with tension [15].

the time domain or phase noise in the frequency domain, with Allan variance defined as:

$$\sigma(\tau) = \sqrt{\frac{1}{2N}\sum_{k=1}^{N}\left(f_{k+1} - f_k\right)^2} \tag{34}$$

Implemented BAW configurations with selected modes and materials effectively scatter BAW *via* acoustic absorbers and substrate grooves,

$$K = \frac{\delta(t)}{f_M} = \frac{1}{f_M}\left[\frac{\sum_{k=1}^{N}\left(f_{k+1} - f_k\right)^2}{2N}\right]^{\frac{1}{2}} \tag{35}$$

Figure 27 shows the frequency stability curve of low-pass filter output loaded with tension. Tests showed stability improvements, with short-term variability down to 0.17726 ppm, accuracy up to 27 Hz, and max frequency jump to 0.45123 ppm.

5. Temperature compensation of SAW yarn tension sensor based on PSO-LSSVM algorithm

Various sensors measure tension, but temperature impacts their accuracy, necessitating compensation [40]. This section explores data fusion techniques, specifically PSO-LSSVM, to enhance SAW yarn sensor precision beyond

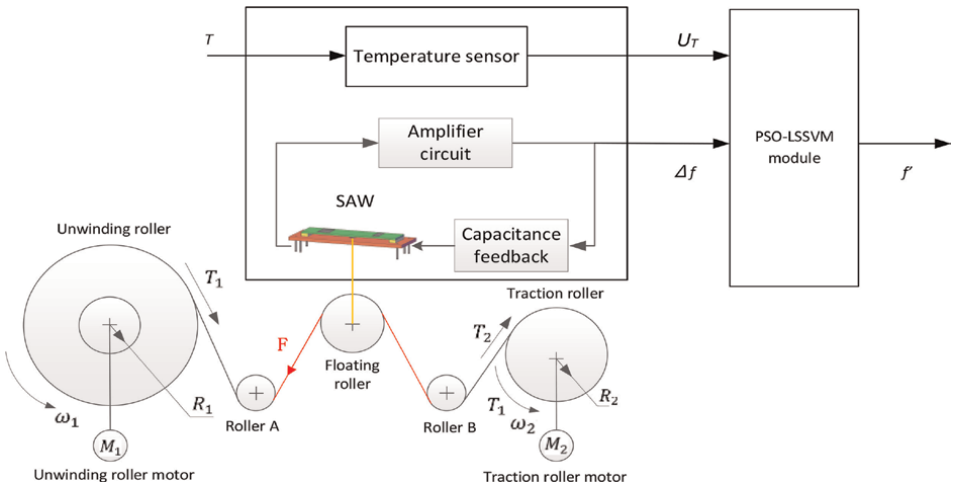

Figure 28.
Temperature compensation of SAW yarn tension sensors using PSO-LSSVM [41].

traditional hardware compensation. The least-squares method establishes fitting equations for frequency shifts and sensor force under varying temperatures post-compensation.

5.1 Principle of SAW yarn tension sensor using PSO-LSSVM module

Figure 28 details the principle of PSO-LSSVM in SAW yarn tension sensors [42–44]. It shows three main components:

1. Motors for unwinding and traction rollers that adjust coil tension, detected by a SAW. device *via* a floating roller.

2. An SAW delay sensor with an amplifier and feedback loop, with an adjacent temperature sensor for ambient temperature readings.

3. A PSO-LSSVM fusion model that neutralizes temperature interference.

The system inputs the SAW sensor's frequency shift Δf and the temperature sensor's output U_T, outputting a compensated frequency f'.

5.2 Principles of PSO-LSSVM algorithms

SVM, a machine learning model known for mapping data into higher dimensions and optimizing decision boundaries [41, 45, 46], converts model training into solving a quadratic programming problem,

$$min\ \frac{1}{2}\|\omega\|^2 + \frac{1}{2}\gamma\sum_{i=1}^{n}\xi_i^2 \tag{36}$$

which has inequality constraints

$$y_i(\omega^\tau \varphi(X_i) + b) \geq 1 - \xi_i \tag{37}$$

In least squares support vector machines (LSSVM), the inequality constraints found in Support Vector Machines (SVM) are converted into equality constraints, which means that:

$$y_i = \omega^\tau \varphi(X_i) + b + \xi_i, i = 1, 2, \ldots, n \tag{38}$$

Which described in Eqs. (37) and (38) also can be transformed into

$$L(\omega, b, \xi, \alpha) = \frac{1}{2}\omega^\tau \omega + \frac{1}{2}\gamma \sum_{i=1}^{n} \xi_i^2 - \sum_{i=1}^{n} \alpha_i \left(\omega^\tau \varphi(X_i) + b + \xi_i - y_k\right) \tag{39}$$

Ultimately, through the integration with the kernel technique, the initial linear equations can be transformed into a nonlinear form

$$f(X) = \sum_{i=1}^{n} \alpha_i K(X, X_i) + b \tag{40}$$

In this part, the kernel function we used is a radial basis function (RBF) kernel, namely,

$$K(X, X_i) = exp\left(-\frac{\|X - X_i\|^2}{2\sigma^2}\right) \tag{41}$$

In the ***k***-th iteration, the position and velocity vector of the ***i***-th particle are adjusted using the following pair of equations:

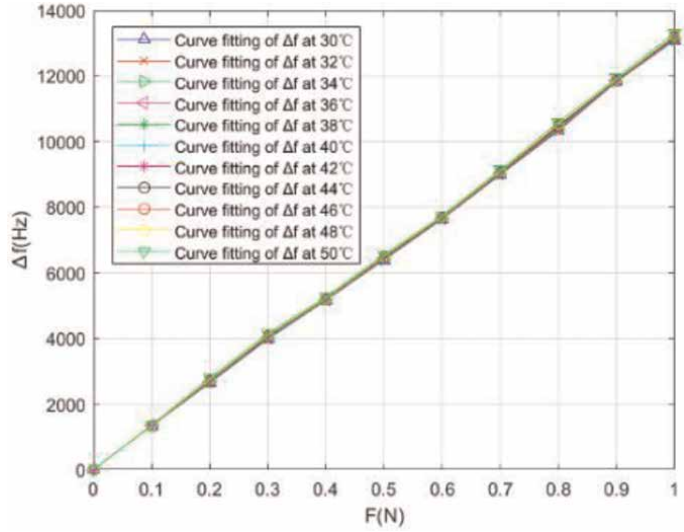

Figure 29.
PSO-LSSVM curve fitting for the relationship between the tension F *and the output frequency shift* Δf *(under different temperature conditions) [41].*

$$V_i^{k+1} = \omega V_i^k + c_1 r_1 \left(P_i^k - X_i^k\right) + c_2 r_2 \left(P_{best}^k - X_i^k\right) \tag{42}$$

$$X_i^{k+1} = X_i^k + V_i^{k+1} \tag{43}$$

5.3 Temperature compensation results and analysis

The LSSVM employs particle swarm optimization (PSO) to fine-tune these parameters, thereby improving LSSVM's predictive accuracy [47–50].

In the PSO-LSSVM algorithm (**Figure 29**), we set $c_1 = 1.6, c_2 = 1.1, \varepsilon = 10^{-8}, t_{max} = 200, \omega_{min} = 0.5$, and $\omega_{max} = 1.6$, so we have the temperature sensitivity coefficient.

$$\alpha_{s2} = \frac{\Delta d_{max}}{\Delta T \bullet \Delta f(FS)} = \frac{264}{20 \times 10590} = 1.2466 \times 10^{-3} °C^{-1} \tag{44}$$

Measurement precision is vital for SAW winding sensors, with the output average error being a key accuracy metric. Within a 0–1 N tension test range, the output average error for each test point is calculated as follows:

$$\sigma_{ae} = \frac{\frac{1}{n}\sum_{i=1}^{n} |x_i - \overline{x}|}{\overline{x}} \tag{45}$$

Through the test of different temperature compensation algorithms, we know that PSO-LSSVM is the most ideal compensation for yarn tension sensor. According to **Figure 30**, the test conclusion is as follows.

1. Applying LSSVM and PSO-LSSVM reduced the SAW Yarn tension sensor's temperature sensitivity coefficient αs from $1.1115 \times 10^{-2} °C^{-1}$ to $2.6851 \times 10^{-3} °C^{-1}$ and $1.2466 \times 10^{-3} °C^{-1}$, a tenfold decrease.

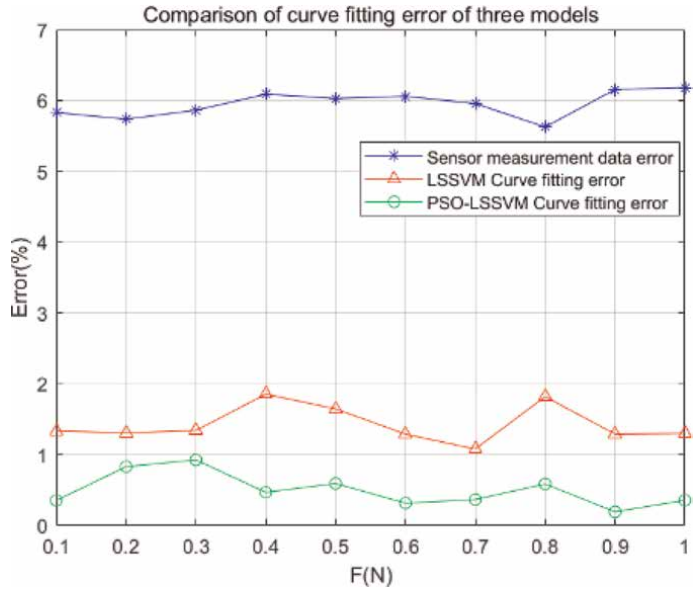

Figure 30.
Comparison the mean error of the SAW Yarn tension sensor in the 0–1 N measurement interval [41].

2. Unoptimized data's average output error is 5.95%. The LSSVM model's average error is over 1.42%, whereas the PSO-LSSVM achieves 0.50% or lower. Hence, PSO-LSSVM is superior for temperature compensation in SAW Yarn tension sensors.

6. Conclusions

In this chapter, we introduce the design of a yarn tension sensor utilizing surface acoustic waves. We also delve into issues such as second-order effects, the design of surface acoustic wave oscillators, and temperature compensation within the sensor. The chapter examines their impact on the sensor and presents effective solutions, thereby enhancing the sensor's performance.

We can draw the following conclusions from this chapter:

1. Design a doubly clamped beam SAW yarn tension sensor, including the choice of the piezoelectric substrate material, the choice of the piezoelectric die size, the placement of IDTs, and the construction of measurement system.

2. Solution to the second-order effect problem of SAW yarn tension sensor, including the split electrode IDTs to improve the in-band ripples of frequency characteristic, arranging acoustic absorbers, and engraving bidirectional slots to improve the out-of-band suppressions of frequency.

3. Test and application of the dual differential channel ensures that the short-term variability of the sensor is reduced 0.17726 ppm, accuracy up to 27 Hz, and max frequency jump to 0.45123 ppm.

4. We tested the SAW yarn tension sensor; the unoptimized data's average output error is 5.95%. The LSSVM model's average error is over 1.42%, whereas the PSO-LSSVM achieves 0.50% or lower. Hence, PSO-LSSVM is superior for temperature compensation in SAW yarn tension sensors.

Author details

Yang Feng[1,2*], Ben Wang[1,2], Keyong Hu[1,2], Shuifa Sun[1,2], Bingkun Zhang[1], Hua Xia[1], Wenbo Liu[1], Haoda Yu[1] and Zhen Yang[3]

1 School of Information Science and Technology, Hangzhou Normal University, Hangzhou, China

2 Mobile Health Management System Engineering Research Center of the Ministry of Education, Hangzhou, China

3 School of Electronic Information, Huzhou College, Huzhou, China

*Address all correspondence to: fengyang@hznu.edu.cn

IntechOpen

References

[1] Feng Y, Lu Z, Lu W. Study of the doubly clamped beam yarn tension sensor based on the surface acoustic wave. IEEE Transactions on Industrial Electronics. 2018;**66**:3256-3264. DOI: 10.1109/TIE.2018.2850028

[2] Zhang JG, Wu XG, Zhu L, Chao Y, Zhang JB. Embedded yarn tension control system based on the design of the sensor. In: Proceedings of the Measuring Technology and Mechatronics Automation, International Conference on IEEE, Zhangjiajie, China, 18 August 2009. Zhangjiajie, China: IEEE Computer Society; 11 Apr 2009. pp. 93-97

[3] Cecati F, Zhu RW, Pugliese S, Liserre M, Wang XF. State feedback reshaping control of voltage source converter. IEEE Transactions on Power Electronics. 2022; **37**:14280-14292

[4] Lei X, Zhang JN, Deng J, Yin P, Shu Z, Tang F. An automatic clock-induced-spurs detector based on energy detection for direct digital frequency synthesizer. Sensors. 2022;**22**:3396. DOI: 10.3390/ s22093396

[5] Quintero S, Figueiredo S, Takahashi V, Llerena RAW, Braga AMB. Passive downhole pressure sensor based on surface acoustic wave technology. Sensors. 2017;**17**:1635

[6] Stoney R, Geraghty D, O'Donnell GE. Characterization of differentially measured strain using passive wireless surface acoustic wave (SAW) strain sensors. IEEE Sensors Journal. 2013;**14**: 722-728

[7] Kim SJ, Kim HA. Effect of fabric structural parameters and weaving conditions to warp tension of aramid fabrics for protective garments. Textile Research Journal. 2018;**88**:987-1001. DOI: 10.1177/0040517517693981

[8] Guzman-Sepulveda JR, May-Arrioja DA, Fuentes-Fuentes MA, Cuando-Espitia N, Torres-Cisneros M, Gonzalez-Gutierrez K, et al. All-fiber measurement of surface tension using a two-hole fiber. Sensors. 2020;**20**:4219-4233. DOI: 10.3390/s20154219

[9] Agarwal A, Psomas C, Krikidis I. Communication systems with amplitude detection: An asymptotic approach. IEEE Internet of Things Journal. 2022;**9**:18319-18322. DOI: 10.1109/jiot.2022.3158947

[10] De Marcellis A, Ferri G, Palange E. A novel Analog autocalibrating phase-voltage converter for signal phase-shifting detection. IEEE Sensors Journal. 2011;**11**:259-266. DOI: 10.1109/ JSEN.2010.2052032

[11] Karnoub A, Kadi N, Azari Z. Using the expert system to analyze loom performance. The Journal of the Textile Institute. 2016;**108**:203-215. DOI: 10.1080/00405000.2016.1160817

[12] Wang JL, Lu CH, Zhang K. Textile-based strain sensor for human motion detection. Energy and Environmental Materials. 2020;**3**:80-100. DOI: CNKI: SUN:EEMS.0.2020-01-007

[13] Engelmann UM, Pourshahidi AM, Shalaby A, Krause HJ. Probing particle size dependency of frequency mixing magnetic detection with dynamic relaxation simulation. Journal of Magnetism and Magnetic Materials. 2022;**563**:169965. DOI: 10.1016/j. jmmm.2022.169965

[14] Takamitsu I, Shingo A, Tatsuhiro O, Nobuo T, Kazushi Y. Dynamic calibration method for trace moisture analyzer based on quick response of ball surface acoustic wave sensor.

Measurement Science and Technology. 2020;**31**:94003. DOI: 10.1088/1361-6501/ab8a7c

[15] Feng Y, Liu W, Wang B. Enhanced frequency stability of SAW yarn tension sensor by using the dual differential channel surface acoustic wave oscillator. Sensors. 2023;**23**:464. DOI: 10.3390/s23010464

[16] Scherr H, Scholl G, Seifert F, Weigel R. Quartz pressure sensor based on SAW reflective delay line. In: Ultrasonics Symposium, Proceedings. Vol. 1. Florida, USA: IEEE; 1996. pp. 347-350. DOI: 10.1109/ULTSYM.1996.583989

[17] Yamada Y, Yoshimura N, Sakurai T. Plastic stress-strain matrix and its application for the solution of elastic-plastic problems by the finite element method. International Journal of Mechanical Sciences. 1968;**10**:343-354. DOI: 10.1016/0020-7403(68)90001-5

[18] Lei BB, Lu WK, Zhu CC, Liu QH, Zhang HX. Optimization of sensitivity induced by substrate strain rate for surface acoustic wave yarn tension sensor. IEEE Sensors Journal. 2015;**15**: 4769-4776. DOI: 10.1109/JSEN.2015.2426018

[19] Zhang JG, Wu XG, Zhu L, Yu C, Zhu WB, Zhang JB. Embedded yarn tension control system based on the design of the sensor. In: Measuring Technology and Mechatronics Automation, International Conference on IEEE. Vol. 261. Zhangjiajie, China: IEEE Computer Society; 2009. pp. 93-97. DOI: 10.1109/ICMTMA.2009.261

[20] Ding Y, Lu W, Zhang Y. Study on the practical application of surface acoustic wave yarn tension sensor. IEEE Transactions on Industrial Electronics. 2021;**69**(12):13781-13790. DOI: 10.1109/TIE.2021.3135618

[21] Zhao HX, Chang DG. Application of fuzzy PID control in yarn tension control system. Applied Mechanics and Materials. 2013;**321**:1748-1752. DOI: 10.4028/www.scientific.net/AMM.321-324.1748

[22] Lei BB, Lu WK, Zhu CC, Liu QH, Zhang HX. A novel optimal sensitivity design scheme for yarn tension sensor using surface acoustic wave device. Ultrasonics. 2014;**54**:1649-1655. DOI: 10.1016/j.ultras.2014.03.004

[23] Chen GF, Sun HC, Zhai LL, Peng LL. A capacitance based circuit design for yarn breaking detection. Advanced Materials Research, Trans Tech Publications. 2012;**562**:1840-1843. DOI: 10.4028/www.scientific.net/AMR.562-564.1840

[24] Lu WK, Feng Y, Zhu CC, Zhen JL. Temperature compensation of the SAW yarn tension sensor. Ultrasonics. 2017; **76**:87-91. DOI: 10.1016/j.ultras.2016.12.006

[25] Lu WK, Hu XM, Zhu CC, Liu JH. Temperature compensation of hall element. Measurement. 2007;**40**:283-287. DOI: 10.1016/j.measurement.2006.05.016

[26] Lu WK, Lu XZ, Zhu CC, Liu QH, Zhang HX. Solving three key problems of the SAW yarn tension sensor. IEEE Transactions on Electron Devices. 2012;**59**:2853-2855. DOI: 10.1109/TED.2012.2209427

[27] Saeed K, Saeed R, Saeed E. Simplification of calibration of low-cost MEMS accelerometer and its temperature compensation without accurate laboratory equipment. Measurement Science and Technology. 2021;**32**. DOI: 10.1088/1361-6501/abd0bf

[28] Naghmeh B, Patrick O, Corbeil JS. Optomechanical modeling and validation of a distributed Bragg reflector force sensor with drift and temperature compensation. IEEE Sensors Journal. 2021;**21**:2929-2941. DOI: 10.1109/JSEN. 2020.3022035

[29] Chen XL, Mei SQ, Chen XB. Non-contact measurement of yarn tension in spinning process. Applied Mechanics and Materials. 2014;**722**:367-372. DOI: 10.4028/www.scientific.net/AMM.722.367

[30] Feng Y, Jun Li R, Bai ZH, Qian. Methods of solving in-band ripples and out-of-band suppression for yarn tension sensor based on surface acoustic wave. IET Circuits, Devices & Systems. 2022;**16**:483-490. DOI: 10.1049/cds2.12121

[31] Lu XZ, Lu WK, Zhu CC. Compensated SAW yarn tension sensor. IEEE Transactions on Instrumentation and Measurement. 2014;**63**:3162-3168. DOI: 10.1109/TIM.2014.2328452

[32] Lu XM, Mouthaan K, Soon YT. Wideband bandpass filters with saw-filter-like selectivity using chip saw resonators. IEEE Transactions on Microwave Theory and Techniques. 2014;**62**:28-36. DOI: 10.1109/TMTT.2013.2292041

[33] Feng Y, Yu H, Liu W, Hu K, Sun S, Yang Z, et al. Grooving and absorption on substrates to reduce the bulk acoustic wave for surface acoustic wave micro-force sensors. Micromachines. 2024;**15**(5):637. DOI: 10.3390/mi15050637

[34] Reindl L, Scholl G, Ostertag T, Scherr H, Wolff U, Schmidt F. Theory and application of passive saw radio transponders as sensors. IEEE Transactions on Ultrasonics. 1998;**45**:1281-1292. DOI: 10.1109/58.726455

[35] Pohlen V, Schnabel A, Neumann F, Gries T. Optimisation of the warp yarn tension on a warp knitting machine. Autex Research Journal. Autex Research Journal. 2012;**12**:29-33. DOI: 10.2478/v10304-012-0006-8

[36] Antonio LN, Valerio APS, Miguel AO, Anna KF, Antonella P, Otavio JDO. Multiple criteria assessment of sustainability programs in the textile industry. International Transactions in Operational Research. 2021;**45**:1550-1572. DOI: 10.1111/itor.12871

[37] Wohltjen H. Mechanism of operation and design considerations for surface acoustic wave device vapour sensors. Sensors & Actuators. 1984;**5**:307-325. DOI: 10.1016/0250-6874(84)85014-3

[38] Memon MM, Liu Q, Manthar A. Surface acoustic wave humidity sensor: A review. Micromachines. 2023;**14**:945. DOI: 10.3390/mi14050945

[39] Shen CY, Hung TT, Chuang YW. Room-temperature NH3 gas surface acoustic wave (saw) sensors based on gra-phene/PPy composite films decorated by Au nanoparticles with ppb detection ability. Polymers. 2023;**15**:4353. DOI: 10.3390/polym15224353

[40] Li Y, Xue Q, Zhang Z. Pressure sensors with ultrahigh sensitivity inspired by spider slit sensilla. IEEE Sensors Journal. 2023;**23**:11729-11737. DOI: 10.1109/jsen.2023.3266753

[41] Feng Y, Liu W, Yu H, Hu K, Sun S, Wang B. Temperature compensation of SAW winding tension sensor based on PSO-LSSVM algorithm. Micromachines. 2023;**14**(11):2093. DOI: 10.3390/mi14112093

[42] Mengue P, Meistersheim L, Hage-Ali S. Magnetic SAW RFID sensor based on love wave for detection of magnetic field

and temperature. IEEE Journal of Radio Frequency Identification. 2023;**7**:528-535. arxiv-2310.03764

[43] Lei B, Lu W, Mian Z. Effect of IDT position parameters on SAW yarn tension sensor sensitivity. Measurement and Control. 2020;**53**:2055-2062. DOI: 10.1177/0020294020965620

[44] Li X, Sun W, Fu W. Advances in sensing mechanisms and micro/nanostructured sensing layers for surface acoustic wave-based gas sensors. Journal of Materials Chemistry A. 2023;**11**:9216-9238. DOI: 10.1039/d2ta10014b

[45] Zhao P, Sharma CH, Liang R. Acoustically induced giant synthetic hall voltages in graphene. Physical Review Letters. 2022;**128**:256601. DOI: 10.1103/physrevlett.128.256601

[46] Ali M, Ahmed R, Ame M. Yarn tension control technique for improving polyester soft winding process. Scientific Reports. 2021;**11**:1060. DOI: 10.1038/s41598-020-79928-1

[47] Jo I, Park S, Kim D. Tension-controlled single-crystallization of copper foils for roll-to-roll synthesis of high-quality graphene films. 2D Materials. 2018;**99**:1-1. DOI: 10.1088/2053-1583/aaa7b8

[48] Chen X, Zhu Z, Shen G, Li W. Tension coordination control of double-rope winding hoisting system using hybrid learning control scheme. Proceedings of the Institution of Mechanical Engineers. 2019;**233**(10):1265-1281. DOI: 10.1177/0959651818824009

[49] Zhang H, Xia H, Lu Y, Wu J, Zhang X, Wei Y. Tension control of a yarn winding system based on the nonlinear active disturbance-rejection control algorithm. Textile Research Journal. 2022;**92**:5049-5065. DOI: 10.1177/00405175221114658

[50] Mandal D, Banerjee S. Surface acoustic wave (SAW) sensors: Physics, materials, and applications. Sensors. 2022;**22**:820. DOI: 10.3390/s22030820

Edited by Jiangyi Zhang

In the technological tide of the 21st century, acoustics—a discipline steeped in history yet bursting with vitality—is advancing at an unprecedented clip, showcasing the immense potential for application across various fields. The book *Acoustical Engineering - The Intricate World of Sound Technology* reviews and offers an in-depth analysis of the latest research breakthroughs and technological advancements in acoustic engineering over the past few years. It paints a vibrant and diverse picture of acoustic technologies, highlighting acoustics' role in modern technology. This book thoroughly explores the applications of acoustics in fields such as acoustic monitoring, mineral resource exploration, target recognition, metamaterials, and manufacturing. The book has clear concepts and rigorous logic, allowing readers to quickly grasp the key points and establish systematic knowledge even when facing complex acoustic theories. Its distinctive feature lies in focusing on the depth and breadth of theoretical knowledge and emphasizing the combination of theory and practice. By analyzing practical cases, readers can understand how acoustic technology can play a role in practical engineering and solve practical problems. The book is for researchers, engineers, graduate students, and advanced undergraduates in fields intertwined with acoustic engineering, physics, geophysics, and mechanical engineering. It is an invaluable guide for related courses, providing a wealth of information and providing inspiration for research and academic pursuits in acoustic engineering.

Published in London, UK

IntechOpen

ISBN 978-0-85014-857-2